UCLA
UCLA Electronic Theses and Dissertations

Title

3D-Printed Lenses, Flat-Layered Meta-Lenses, and Transmitarrays for Next-Generation Spaceborne Applications and Orbital Angular Momentum Beams

Permalink

https://escholarship.org/uc/item/3cc746mv

Author

Papathanasopoulos, Anastasios

Publication Date

2022

Peer reviewed|Thesis/dissertation

UNIVERSITY OF CALIFORNIA

Los Angeles

3D-Printed Lenses, Flat-Layered Meta-Lenses, and Transmitarrays for Next-Generation

Spaceborne Applications and Orbital Angular Momentum Beams

A dissertation submitted in partial satisfaction

of the requirements for the degree

Doctor of Philosophy in Electrical and Computer Engineering

by

Anastasios Papathanasopoulos

2022

ABSTRACT OF THE DISSERTATION

3D-Printed Lenses, Flat-Layered Meta-Lenses, and Transmitarrays for Next-Generation

Spaceborne Applications and Orbital Angular Momentum Beams

by

Anastasios Papathanasopoulos

Doctor of Philosophy in Electrical and Computer Engineering

University of California, Los Angeles, 2022

Professor Yahya Rahmat-Samii, Chair

Real-life communications applications necessitate the development of antennas with different patterns and radiation characteristics. Antennas that can produce the beam scanning in a conical sweep can be advantageous for applications such as spaceborne wind scatterometers weather radars. This work presents the synthesis, prototyping and measurements of three antennas that can produce the conical beam scanning: The 3D-printed shaped and material-optimized lenses, the flat-layered meta-lenses, and the transmitarray antennas. The synthesis of the 3D-printed lens and meta-lens inhomogeneity requires the use of a software package hybridizing the computational electromagnetics method of Geometrical optics (GO) with the optimization strategy of Particle Swarm Optimization (PSO). Additionally, a new synthesis algorithm is presented for the design of transmitarrays that can produce the conical beam sweep based on the optimization of the feed location and a modified transmitarray phase compensation. Novel implementation and fabrication methods based on additive manufacturing and metamaterial structures are presented for the realization of the proposed antennas. In the last part of this work, Orbital Angular Momentum (OAM) beams for antenna applications are investigated. The theory and mathematical formulations of the far-field properties of OAM beams using the antenna aperture field method are presented in a systematic and comprehensive manner. Transmitarray antennas are proposed to generate circularly-polarized (CP) OAM beams with cone-shaped radiation patterns. Antennas with cone-shaped patterns can be advantageous for applications such as geosynchronous satellite-

based navigation and guidance systems that serve moving vehicles and ceiling-mounted indoor wireless systems. An ultra-thin "S-ring" transmitarray unit cell is introduced to support CP that can provide arbitrary CP phase compensation by proper rotation of the elements. The synthesis, prototyping and measurement validation of a proof-of-concept transmitarray prototype are presented and demonstrate that the proposed transmitarray antenna can be a unique apparatus that generates CP OAM cone-shaped patterns.

The dissertation of Anastasios Papathanasopoulos is approved.

Aydin Babakhani

Yuanxun Ethan Wang

Mona Jarrahi

Yahya Rahmat-Samii, Committee Chair

University of California, Los Angeles

2022

To my beloved wife Audrey and family. . .

For their endless love, support, and encouragement.

TABLE OF CONTENTS

LIST OF FIGURES

x

xiv

LIST OF ACRONYMS

AR Axial Ratio. xvi–xviii, 96, 97, 103, 104, 111–113

CP Circularly-Polarized. ii, iii, xvi, xvii, 5, 11, 13, 89, 90, 94–98, 102, 103, 105, 106, 108, 111–113, 117, 123–125

FDM Fused Deposition Modeling. 6, 23, 35, 40

FEM Finite Element Method. 66

GO Geometrical optics. ii, x, xi, xvii, 6, 9, 22–24, 26, 33, 40, 43–46, 61, 114, 118, 119

LHCP Left-Hand Circularly-Polarized. xv, xvi, 94–96, 102–104, 106–109, 111, 113, 123–125

LP Linearly-Polarized. 89, 91, 95–99, 113

OAM Orbital Angular Momentum. ii, iii, xv, xvi, xviii, 11, 13, 86–99, 102–105, 107–109, 111–113, 117

PSO Particle Swarm Optimization. ii, x, xi, xiv, 6, 9, 22–24, 28, 30, 40, 43–45, 61, 77, 78, 84, 114, 115, 118

PTFE Polytetrafluoroethylene. 1

RHCP Right-Hand Circularly-Polarized. xv, xvi, 94–96, 102–104, 106–113, 123–125

SatComs Satellite Communications. 1

WirelessHD Wireless High Definition. 1

WLAN/WPAN Wireless Local Area Network/Wireless Personal Area Network. 1

ACKNOWLEDGMENTS

I am forever grateful to my advisor, Distinguished Professor Yahya Rahmat-Samii, who has been an example for me as an excellent educator and researcher and has served as a role model in my life. This dissertation is a fruit of his endless support and continuous guidance throughout my Ph.D. research. Professor Rahmat-Samii, I could not have imagined a better mentor for my Ph.D. study, and I will sincerely consider you as a friend for the remainder of my life. I would like to thank Professors Aydin Babakhani, Yuanxun Ethan Wang, and Mona Jarrahi for their insightful feedback and time spent as part of my thesis committee. I would also like to thank Professor Tatsuo Itoh for his time serving as my committee member. While he is sadly no longer with us, his advice and guidance greatly improved the quality of this dissertation.

I thank my colleagues at the UCLA Antenna Research, Analysis, and Measurement (ARAM) Laboratory: Jordan Budhu, Vignesh Manohar, Lingnan Song, Daisong Zhang, Dustin Brown, Junbo Wang, Yubin Cai, Tianjian Huang, and Botian Zhang for their constant support and fruitful discussions that led to some of the ideas presented in this dissertation. I look forward to our future discussions and great collaborations, and I warmly wish you all the best in the future.

None of my accomplishments would be possible without the unconditional support and continuous encouragement provided to me by my family and friends, who have played a vital role in shaping who I am now. I would also like to thank my beloved wife, Audrey, for standing beside me throughout my life journey.

VITA

2012–2017	**BSc & MSc in Electrical and Computer Engineering**, National Technical University of Athens (NTUA), Athens, Greece
2017–2022	**Graduate Student Researcher**, UCLA Antenna Research, Measurement and Analysis Laboratory
2017–2018	**UCLA Henry Samueli School of Engineering and Applied Sciences (HSSEAS) Fellowship**
2019–2022	**Future Investigator in NASA Earth and Space Science and Technology (FINESST) Award**
2019–2022	**Onassis Foundation Scholarship**
2019	**Henry Samueli Excellence in Teaching Award**
2019	**Gerondelis Foundation Scholarship**
2020	**Teaching Assistant Consultant (TAC)**, UCLA
2020	**Best Paper 3ʳᵈ Place in 2020 Symposium of the Antenna Measurement Techniques Association**
2020–2021	**Antenna Design Engineering Summer Intern**, Apple Inc.

PUBLICATIONS

Anastasios Papathanasopoulos, and Yahya Rahmat-Samii. "Transmitarray Antenna for Conical Beam Scanning," *IEEE Transactions on Antennas and Propagation*, Submitted February 2022. (Under Review).

Junbo Wang, **Anastasios Papathanasopoulos**, Yahya Rahmat-Samii, Ryan Hensleigh, Zhenpeng Xu, and Xiaoyu Zheng. "Ultra-Lightweight Transmitarray Antenna Enabled by Charge-Programmed Three-Dimensional Multi-Material Printing", *in 2022 United States National Committee of URSI National Radio Science Meeting (USNC-URSI NRSM)*, Boulder, CO, USA, 2022, pp. 302-303.

Anastasios Papathanasopoulos, Jordan Budhu, Yahya Rahmat-Samii, Richard E. Hodges, and Donald F. Ruffatto. "3-D-Printed Shaped and Material-Optimized Slimmed Lenses for Next-Generation Spaceborne Wind Scatterometer Weather Radars," *IEEE Transactions on Antennas and Propagation*, vol. 70, no. 5, pp. 3163-3172, May 2022.

Anastasios Papathanasopoulos, and Yahya Rahmat-Samii. "Fundamentals of Orbital Angular Momentum Beams: Concepts, Antenna Analogies, and Applications," *in Electromagnetic Vortices: Wave Phenomena and Engineering Applications*, Zhi Hao Jiang, and Douglas Werner, Ed. Wiley 2021.

Anastasios Papathanasopoulos, and Yahya Rahmat-Samii. "Low-Profile Transmitarray for Wide-Angle Conical Scanning: Concept, Optimization and Validation." *in 2021 IEEE International Symposium on Antennas and Propagation and USNC-URSI Radio Science Meeting (APS/URSI)*, pp. 1079-1080. IEEE, 2021.

Anastasios Papathanasopoulos, and Yahya Rahmat-Samii. "Multi-Layered Flat Meta-Lenses for Conical Beam Scanning via Optimization of Geometrical Optics." *in 2021 IEEE*

International Symposium on Antennas and Propagation and USNC-URSI Radio Science Meeting (APS/URSI), pp. 105-106. IEEE, 2021.

Anastasios Papathanasopoulos, and Yahya Rahmat-Samii. "Transmitarray Antenna Generating Circularly Polarized Orbital Angular Momentum (OAM) Beams: Synthesis, Prototyping and Measurements." *in 2021 Antenna Measurement Techniques Association Symposium (AMTA)*, 2021.

Anastasios Papathanasopoulos, Yahya Rahmat-Samii, Ryan Bahr, Yepu Cui, and Manos M Tentzeris. "Introducing Inkjet Printing Technology to the Fabrication of Flat-Layered Meta-Lens Antennas." *in 2021 United States National Committee of URSI National Radio Science Meeting (USNC-URSI NRSM)*, Boulder, CO, USA, 2021, pp. 49-50.

Anastasios Papathanasopoulos, and Yahya Rahmat-Samii. "A Review on Orbital Angular Momentum (OAM) Beams: Fundamental Concepts, Potential Applications, and Perspectives." *in XXXIII General Assembly and Scientific Symposium (GASS) of the International Union of Radio Science*, 2021. (Invited Paper)

Anastasios Papathanasopoulos, Yahya Rahmat-Samii, Nicolas Garcia, and Jonathan Chisum. "A Novel Collapsible Flat-Layered Metamaterial Gradient-Refractive-Index (GRIN) Lens Antenna," *IEEE Transactions on Antennas and Propagation*, vol. 68, no. 3, pp. 1312-1321, March 2020. (Invited Paper).

Anastasios Papathanasopoulos, and Yahya Rahmat-Samii. "Multi-Layered Flat Meta-material Lenses: Design, Prototyping and Measurements." *in 2020 Antenna Measurement Techniques Association Symposium (AMTA)*, pp. 1-6. IEEE. **Best Paper, 3$^{\text{rd}}$ Place**.

Cheng Tao, **Anastasios Papathanasopoulos**, and Tatsuo Itoh. "Linear-to-Circular Polarization Converter Based on Stacked Metasurfaces with Aperture Coupling Interlayer." *in 2020 IEEE/MTT-S International Microwave Symposium (IMS)*, pp. 1-4. IEEE, 2020.

Anastasios Papathanasopoulos, and Yahya Rahmat-Samii. "Flat Meta-Lens Antenna Synthesis Via Geometrical Optics and Particle Swarm Optimization." *in 2020 IEEE International Symposium on Antennas and Propagation and CNC/USNC-URSI Radio Science Meeting*, pp. 857-858. IEEE, 2020.

Themistoklis Mavrogordatos, **Anastasios Papathanasopoulos**, and George Fikioris. "An Effective-Current Approach for Hallén's Equation in Center-Fed Dipole Antennas with Finite Conductivity," *IEEE Transactions on Antennas and Propagation*, vol. 67, no. 6, pp. 3680-3687, June 2019.

Anastasios Papathanasopoulos, and Yahya Rahmat-Samii. "A Systematic Approach for the Design of Metallic Delay Lenses." *in 2019 United States National Committee of URSI National Radio Science Meeting (USNC-URSI NRSM)*, Boulder, CO, USA, 2019, pp. 1-2.

Anastasios Papathanasopoulos, and Yahya Rahmat-Samii. "A Novel Deployable Compact Lens Antenna Based on Gradient-Index Metamaterials", *in 2019 IEEE International Symposium on Antennas and Propagation & USNC/URSI National Radio Science Meeting*, Atlanta, GA, USA, 2019, pp. 625-626.

George Fikioris, and **Anastasios Papathanasopoulos**. "On the Thin-Wire Integral Equations for Carbon Nanotube Antennas," *IEEE Transactions on Antennas and Propagation*, vol. 66, no. 7, pp. 3567-3576, July 2018.

CHAPTER 1

Introduction

1.1 Lens Antennas Evolution: From Homogeneous Dielectric Lenses to Flat-Layered Meta-Lenses

Lens antennas have attracted significant interest in a variety of antenna systems in microwave and millimeter wave frequencies [1]. The conventional approach to lens design has been to shape the surfaces of dielectric materials in such a manner as to curve the paths that rays follow as they transit through the lens interfaces. One major advantage of lenses over reflectors is that the feed and its supporting structure are located behind the antenna and that there is no central feed blockage for symmetric configurations that are typically advantageous mechanically. This unique feature that eliminates blockage adverse effects was the key for the development of homogeneous dielectric lenses for many applications in the microwave and millimeter frequency regimes. Some representative homogeneous shaped dielectric lenses are shown in Fig. 1.1. In previous work, shaped dielectric lenses were proposed as antenna elements for mobile broadband communications systems at millimeter wavelengths [2]. A solid dielectric ellipsoid PTFE lens-based antenna concept for high precision industrial Tank Level Probing Radar measurements at 24GHz was introduced in [3]. In [4], the design of a quartz extended hemispherical lens and experimental verification of electronically steerable Integrated Lens Antennas (Fig. 1.1a) for WLAN/WPAN communication systems operating in the 60-GHz frequency band were presented. Reference [5] demonstrated the potential of Stereolithography-based horn-lens antennas (Fig. 1.1b) for Satellite Communications (SatComs) in Ka-Band. A compact and low-cost horn-lens antenna solution (Fig. 1.1c) to perform total mechanical beam steering in the 60-GHz Wireless High Definition (WirelessHD)
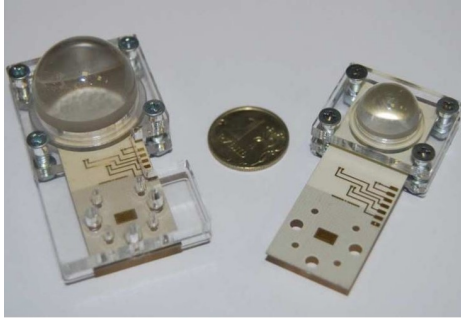
(a) Integrated Lens Antennas for WLAN WPAN Applications [4].

(b) Stereolithography-Based Antennas for Satellite Communications in Ka-Band [5].

(c) Compact Beam-Steerable Lens Antenna for 60-GHz WirelessHD Communications [6].

Figure 1.1 Representative homogeneous shaped dielectric lens antennas.

entertaining network band was studied in [6]. In [7], integrated axial-symmetric double-shell Macor/Plexiglass lens antenna solutions for future space remote sensing applications at the 500 GHz to 1500 GHz band were investigated. In [8], wide-scan spherical-lens antennas were developed for automotive radars and were intended for automatic cruise control and/or collision avoidance applications.

Notwithstanding their popularity, homogeneous shaped dielectric lenses are limited by the wave aberrations that are inherent to the way in which electromagnetic waves refract at the interface between two materials. As the wave refraction occurs only at the input and output surfaces of a conventional lens, the trajectory of rays is only altered at the interfaces and rays travel in straight lines within the volume of the lens. Alternatively, the refractive index of the medium can be varied spatially throughout the body of the lens forming the Gradient-Refractive-Index (GRIN) lenses that control the optical ray paths inside the lens rather than relying only on refraction at the interface between two uniform materials. In this manner, far greater control can be achieved over the ray trajectories since incoming electromagnetic waves can travel in a curved path within the volume of the lens. A classical GRIN lens antenna was proposed in 1949 by R.K. Luneburg [9]. This type of optical device is a spherically symmetric lens where the refractive index varies as a function of the distance from the center of the sphere, according to the equation $n(r) = [2 - (r/R)^2]^{1/2}$, where r is the distance at each point measured from the center of the lens and R is the radius of the

(a) Half-spherical Luneburg lens antenna based on the drilled-hole approach on the commercially available dielectric boards [12].
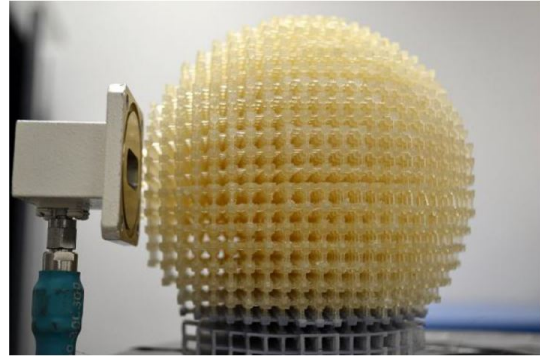
(b) 3D-printed Eaton lens antenna fabricated by polymer jetting rapid prototyping [19].

Figure 1.2 Representative spherically symmetric inhomogeneous lens antennas.

lens.

Since the conceptualization of the Luneburg lens, advancements in artificially engineered materials and additive manufacturing [10] allowed for the construction of Luneburg lens antenna prototypes. For example, [11] presents a 3D-printed Luneburg lens antenna fabricated by polymer jetting rapid prototyping where the gradient-index is realized by controlling the filling ratio of a polymer/air-based unit cell. In [12], a half-spherical Luneburg lens is designed based on the perforated dielectric approach where the effective index is tuned by varying the size of the drilled holes on the commercially available dielectric boards (see Fig. 1.2a). Several design recipes for various spherically symmetric lenses have been discussed in the literature [13–18], and proof of concept prototypes have been reported such as a 3D-printed Eaton lens [19] (see Fig. 1.2b) and a half Maxwell fisheye lens based on the drilled-hole approach on the commercial dielectric boards [12].

Although spherically symmetric lenses have significant advantages over conventional homogeneous shaped dielectric lenses, they are far less prevalent in practical applications because of their excessive weight. Due to spherical symmetry, the material that fills the volume of the lens increases and the weight becomes impractical for applications that require highly directive antennas. In order to overcome this disadvantage, antenna engineers have developed ways to produce "slimmed" alternatives to the classical Luneburg lens. 3D-printed shaped

3
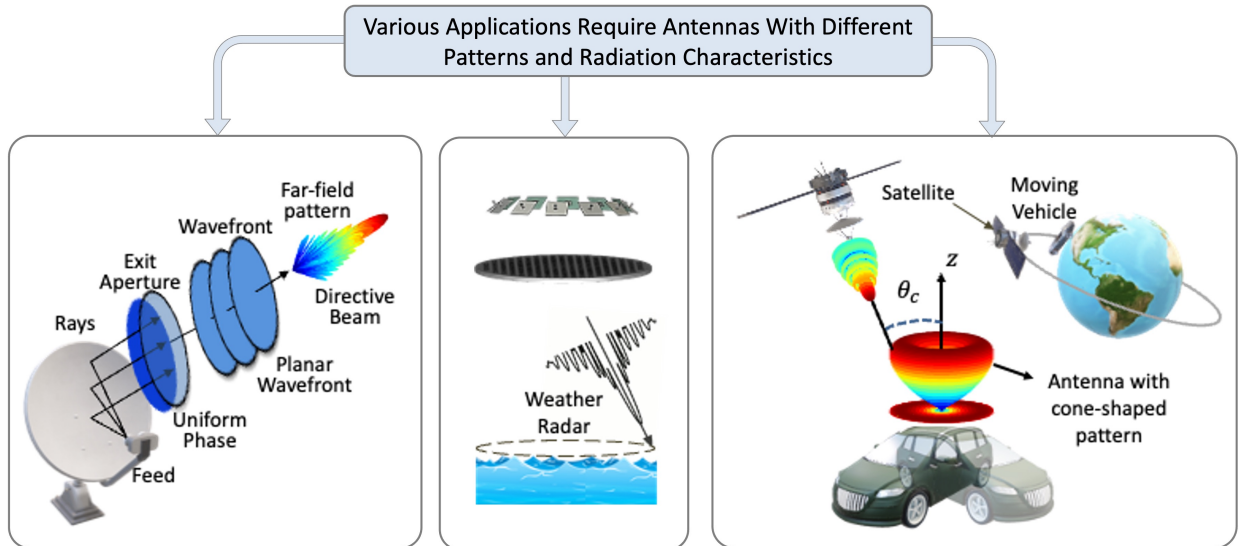
Figure 1.3 Real-life applications require antennas with different patterns and radiation characteristics.

and material-optimized lenses [20–23], flat-layered meta-lenses [24–26], and transmitarray antennas based on phase shifting metasurfaces [27–29] have recently gained attention. These antennas overcome the disadvantage of excessive bulk and weight of spherically symmetric lenses while maintaining high performance. Additionally, advancements in 3D-printing and lithography techniques allow the fabrication on demand and open the door for the realization of these antennas.

1.2 Motivation: The Need for Antennas With Atypical Patterns and Radiation Characteristics

Real-life applications require antennas with different patterns and radiation characteristics. Antennas are typically synthesized to produce an aperture field with uniform phase to achieve a directive antenna radiation pattern, as shown in Fig. 1.3. Conventional antenna systems that convert the input wavefront into a planar wavefront to produce directive on-axis beams were presented in previous work [30–32]. However, real-life applications necessitate significant developments regarding the synthesis, optimization, and prototyping of antennas with atypical radiation characteristics, as shown in Fig. 1.3. For example, some potential applications
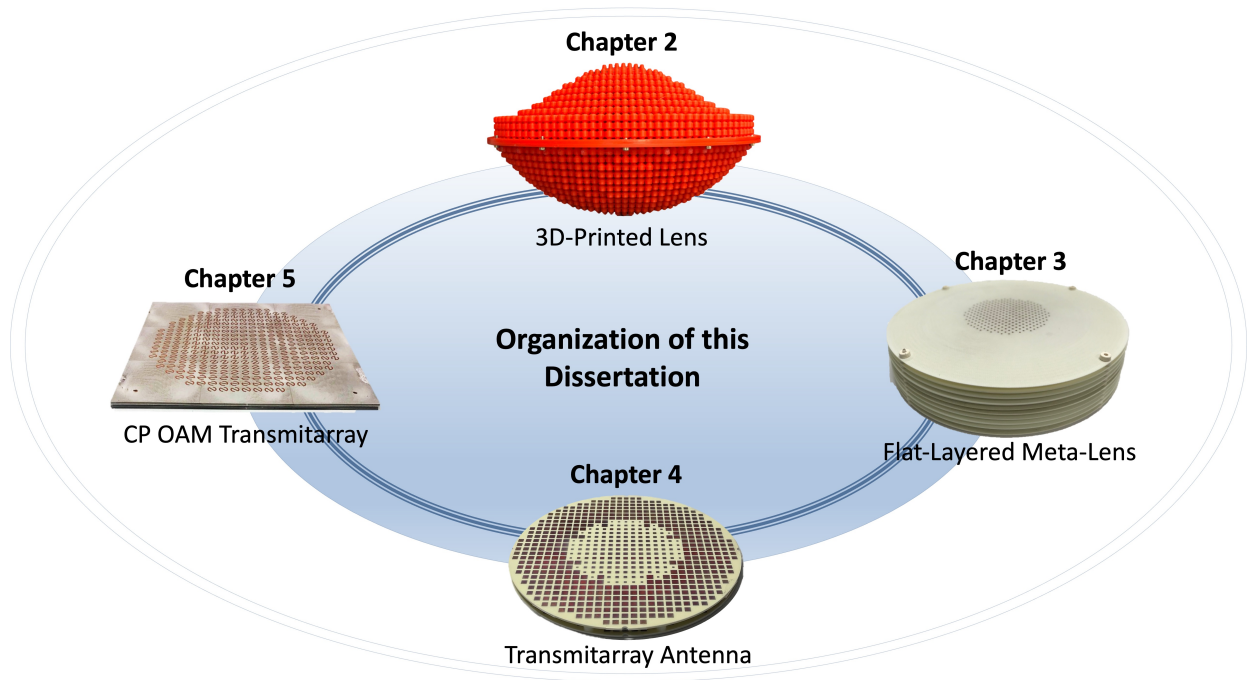
Figure 1.4 Organization of this Dissertation.

requiring conical beam scanning include spaceborne wind scatterometers that take multiple (at least four) measurements along an azimuthal conical scan to retrieve the wind speed and direction [21, 33–35]; spaceborne microwave radars [36–38] as well as millimeter wave imaging systems [39–44]. Additionally, CP cone-shaped patterns can be advantageous for applications that require cone-shaped patterns, such as in geosynchronous satellite-based navigation and guidance systems that serve moving vehicles and ceiling-mounted indoor wireless systems [45–48]. The goal of this dissertation is to identify real-life antenna problems requiring atypical patterns and present the design of antennas that directly address the needs of actual applications. In particular, the synthesis, prototyping and measurement results of 3D-printed shaped dielectric lenses, flat-layered meta-lenses, and transmitarray antennas are presented.

1.3   Organization of this Dissertation

The organization of this dissertation is shown in Fig. 1.4.

Chapter 2 presents a lightweight, 3D-printed, inhomogeneous lens antenna for spaceborne wind scatterometer weather radars. The outline of Chapter 2 is illustrated in Fig. 1.5. The operation of spaceborne wind scatterometers is revisited. To eliminate the risk of mechanical rotation failure that occurred in previous scatterometer missions, an antenna design with no moving parts that achieves the conical beam sweep is desirable. The 3D-printed lens is proposed as an antenna alternative with no moving parts that achieves the conical beam sweep. The lens is designed using curved-ray GO coupled to PSO to determine the optimum lens surface shapes and material inhomogeneity while obtaining a design with minimum volume and therefore mass [20]. An 18 cm lens is designed using this approach. Instructions on how to 3D-print the inhomogeneous lens is given using a unit cell design which permits additive manufacturing using Fused Deposition Modeling (FDM) techniques. The lens is measured for far-field pattern performance at various locations along the ring-shaped focus of the azimuthally symmetric lens. The measurements agree well with predictions obtained by full-wave simulations. The novelty of this work compared to previous works lies in the following: a) The most recent Ku-band scatterometer pencil-beam antenna topology employs a parabolic dish that is conically-rotated to provide multiple azimuth measurements. The proposed 3D-printed lens is presented as an alternative for the traditional mechanically driven design that can prolong the lifetime of future spaceborne wind scatterometers. b) The proposed 3D-printed lens is a more lightweight design than the spherical Luneburg lens (the 3D-printed lens volume is less than 50% of the volume of the spherical lens with the same diameter) that can produce the conical electronic scan. c) Only on-axis fed 3D-printed shaped and material-optimized lenses have been presented in the literature so far. This work addresses off-axis designs suitable for the real-life application requiring conical beam scanning. d) A novel unit cell design is presented which permits additive manufacturing using FDM techniques.

Chapter 3 presents the design, prototyping and measurement results of multi-layered flat metamaterial lenses for both on-axis and off-axis fed meta-lenses. The outline of Chapter 3 is illustrated in Fig. 1.6. The numerical synthesis algorithm based on GO and PSO is revisited and applied to synthesize both on-axis and off-axis fed meta-lenses. It is shown
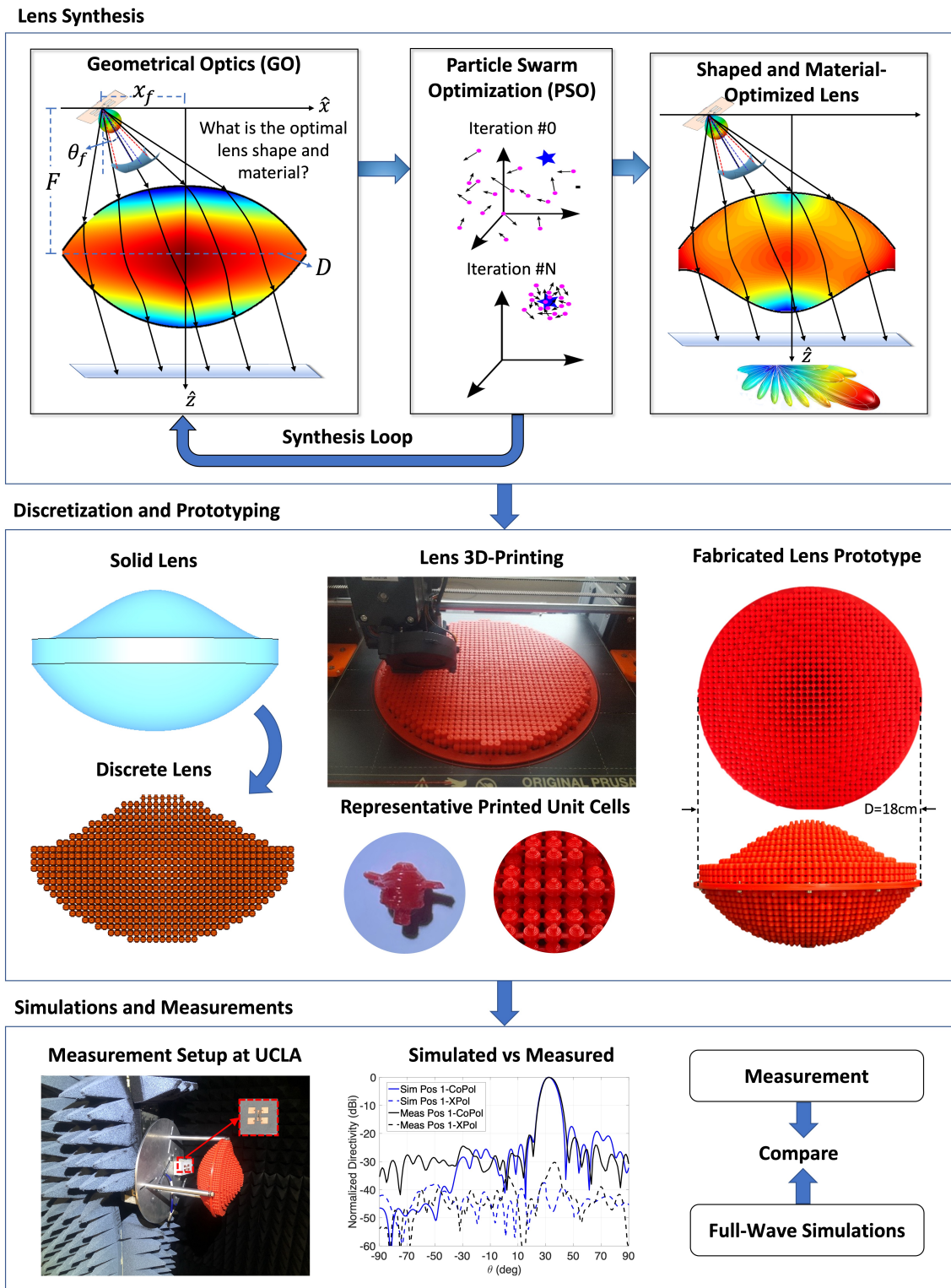
Figure 1.5 Outline of Chapter 2. 3D-Printed Shaped and Material-Optimized Lenses for Next-Generation Spaceborne Wind Scatterometer Weather Radars.
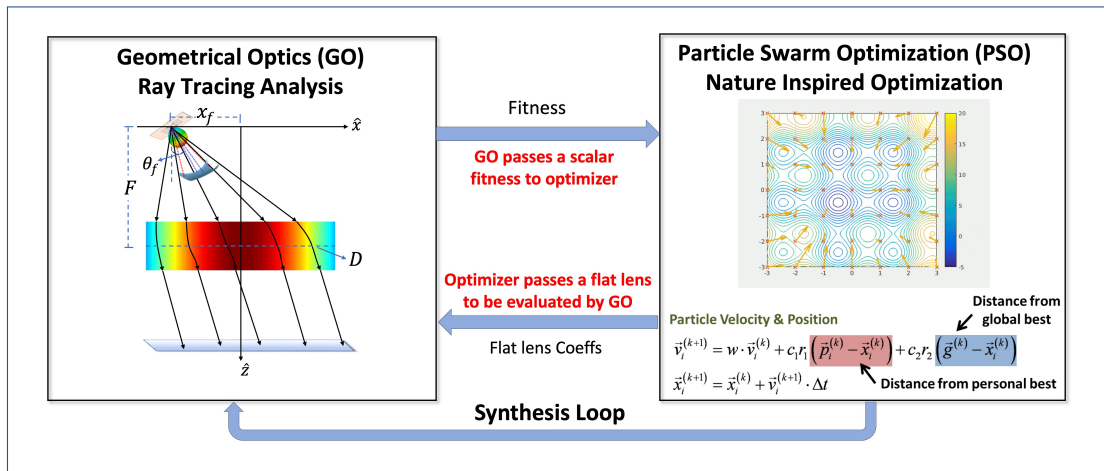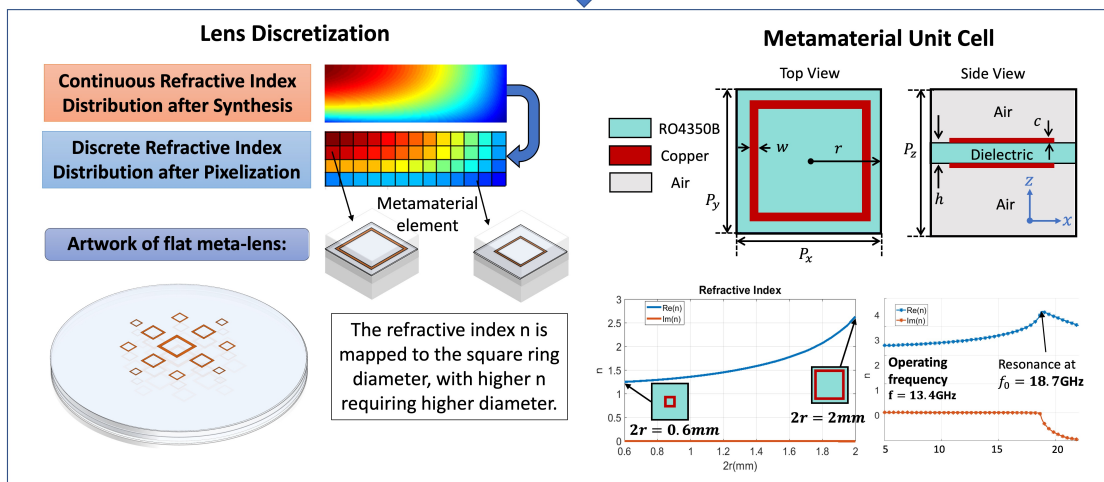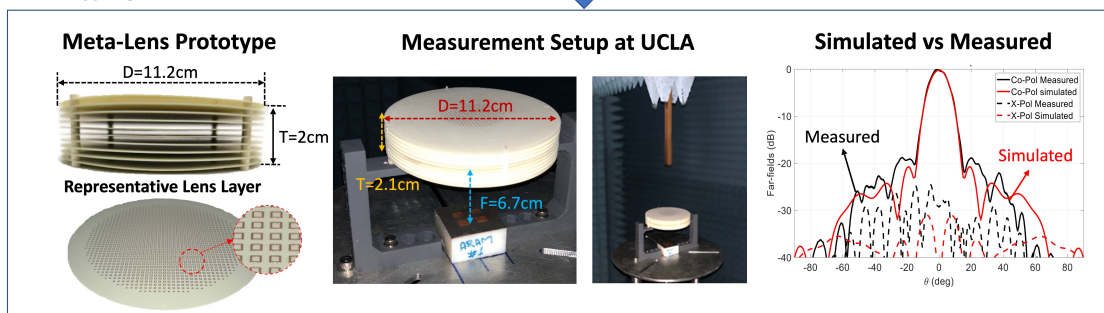
Figure 1.6 Outline of Chapter 3. Flat-Layered Meta-Lens Antennas: Synthesis, Prototyping and Measurements.

that the lens designs based on the numerical synthesis algorithm outperform the designs that are produced using previous synthesis methods that are based on the straight path approximation. The discretization methodology and prototyping of flat meta-lenses is also discussed. Simulation and measured results of a proof-of-concept on-axis fed flat-layered meta-lens prototype operating at 13.4 GHz are presented. The novelty of this work lies in the following: a) Previous meta-lens synthesis methods, which are approximate and applicable only for on-axis fed lenses, assume that the ray path is straight within the volume of the lens. In this work, the GO-PSO algorithm is proposed to synthesize flat-layered inhomogeneous lenses. b) The proposed synthesis technique is applicable for on- and off-axis fed meta-lenses with circular symmetry thus providing conically scanned beams for the off-axis designs. An example of an optimized on-axis fed meta-lens is presented along with a flat meta-lens that is synthesized based on the straight ray path approximation to highlight the superior performance of the optimized lens. A second example of an optimized off-axis fed lens is synthesized to demonstrate the effectiveness of the proposed algorithm for the off-axis designs. c) Novel implementation techniques for the fabrication of flat-layered meta-lenses are presented. The concept of collapsible flat-layered lens based on gradient-refractive-index metamaterials is introduced. A novel metamaterial unit cell is presented where adjacent lens layers are separated by an air gap, which allows the lens to collapse and be stored in a stacked configuration. The attractiveness of the meta-lens design is its low packaging height, low profile and weight.

Chapter 4 proposes transmitarrays as an antenna solution that can achieve the conical beam sweep. The outline of Chapter 4 is illustrated in Fig. 1.7. Compared to the previously reported transmitarrays, the development of an off-axis fed transmitarray for conical beam scanning requires significant advancements regarding the synthesis and optimization of the off-axis fed transmitarray. Therefore, a novel synthesis algorithm is presented based on the optimization of the feed location and a modified transmitarray phase compensation. To validate the approach, an 18 cm transmitarray with a thickness of 0.8 cm operating at 13.4 GHz is designed, simulated, prototyped and measured. Predictions obtained by full-wave simulations agree well with the measured results. The conical beam scanning capability of
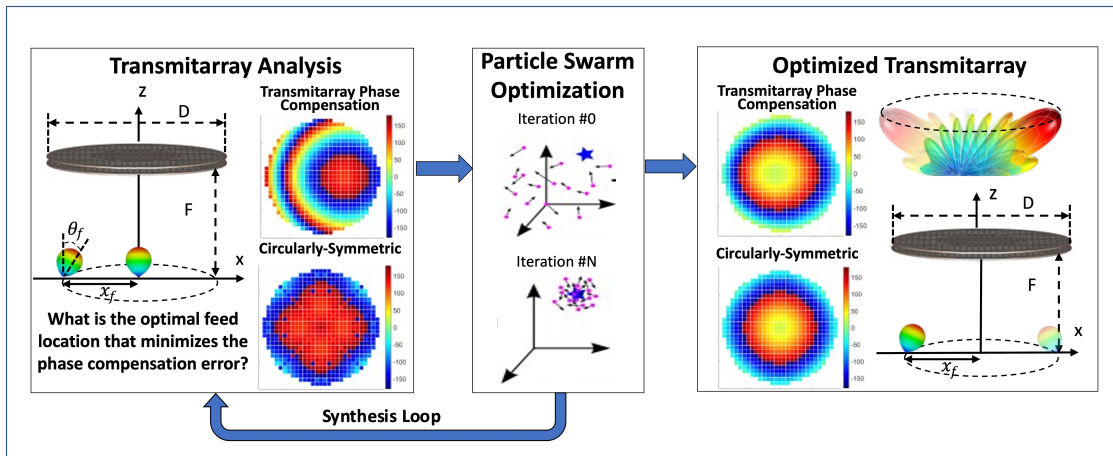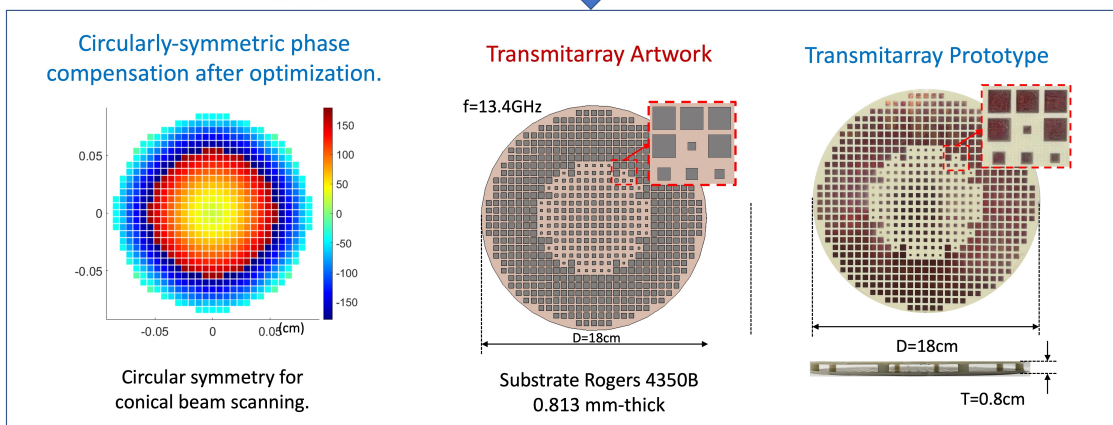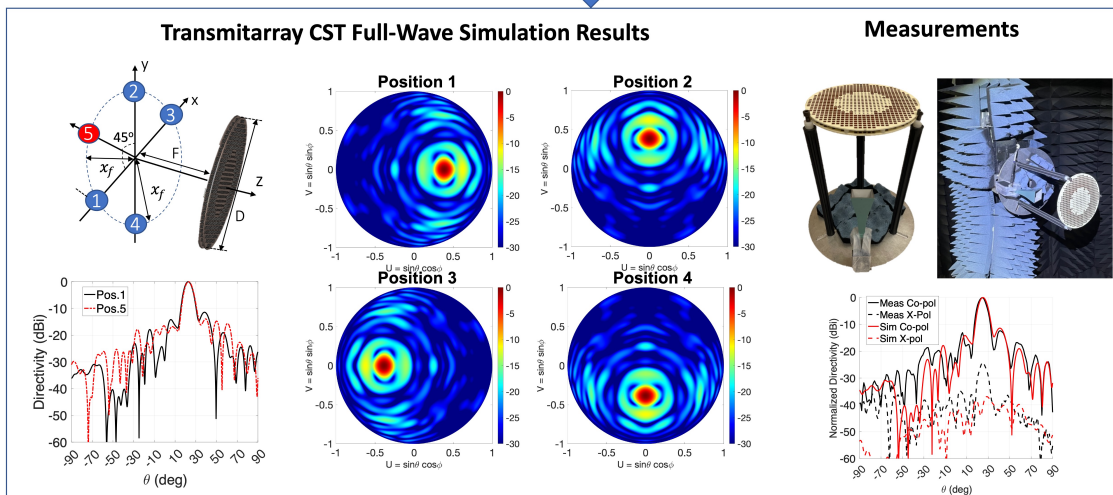
Figure 1.7 Outline of Chapter 4. Low-Profile Transmitarray Antenna for Conical Beam Scanning: Concept, Optimization, and Measurements.

the transmitarray is demonstrated through measurements taken with the feed placed at five locations within the ring focus. The novelty of this work over previous works is the following: (a) This is the first time that transmitarrays are proposed as an antenna alternative that can achieve the conical beam sweep. (b) Unlike conventional transmitarrays, the synthesis of transmitarrays for conical beam scanning is a challenging problem. A novel synthesis algorithm is proposed based on the particle swarm optimization of the feed location and a modified transmitarray phase compensation. (c) The thickness and therefore the weight of the previously reported lenses proposed for conical beam scanning scales with the lens diameter, whereas the proposed transmitarray is low-profile with reduced thickness that does not scale with the transmitarray diameter.

Chapter 5 focuses on OAM beams and addresses two main challenges: The lack of a comprehensive and systematic characterization of the far field properties of OAM beams that would potentially facilitate the design of OAM antennas and the development of low-profile antennas that can generate CP OAM beams. To address these challenges, insight into the far field properties of OAM beams is provided using the antenna aperture field method. Analytical and semi-analytical formulas for the far field of circularly-symmetric OAM aperture fields are derived and validated through full-wave simulations. The derived formulas can potentially guide the design of OAM communication systems. Second, transmitarray antennas are proposed for the generation of CP OAM beams. A novel "S-ring" transmitarray element is designed to sustain CP operation with only three metal patterned layers. The synthesis, prototyping and measurement validation of a proof-of-concept prototype with a thickness of 3 mm operating at 19 GHz are presented. The measurements agree well with predictions obtained by full-wave simulations and demonstrate that the proposed transmitarray antenna can be a unique apparatus that generates OAM CP cone-shaped patterns. The outline of Chapter 5 is illustrated in Fig. 1.8. The novelty of this work lies in the following: a) To the author's best knowledge, there has not been a comprehensive and systematic characterization of the far-field properties of OAM beams (some aspects have been discussed in [49,50] but not thoroughly investigated). Understanding the far-field properties of OAM beams is important because: (i) In many application scenarios, an OAM-carrying radiation is characterized in

11

Aperture Field Method Tailored for OAM

Exit-Aperture Field $\vec{E}(\rho', \phi')$

Amplitude   Phase   Far-field

Conventional Antenna

Uniform

Directional Pattern

OAM Antenna

OAM

Cone-Shaped Pattern

From Far-Field integrals:

$$N_\theta = \iint_S \left(J_x \cos\theta \cos\phi + J_y \cos\theta \sin\phi \right) e^{jk\hat{r}\cdot\vec{r}'} ds'$$

$$N_\phi = \iint_S \left(-J_x \sin\phi + J_y \cos\phi \right) e^{jk\hat{r}\cdot\vec{r}'} ds'$$

$$L_\theta = \iint_S \left(M_x \cos\theta \cos\phi + M_y \cos\theta \sin\phi \right) e^{jk\hat{r}\cdot\vec{r}'} ds'$$

$$L_\phi = \iint_S \left(-M_x \sin\phi + M_y \cos\phi \right) e^{jk\hat{r}\cdot\vec{r}'} ds'$$

To Far-Field expressions:

$$E_r \simeq 0 \qquad H_r \simeq 0$$

$$E_\theta \simeq -\frac{jke^{-jkr}}{4\pi r}(L_\phi + \eta N_\theta) \qquad H_\theta \simeq +\frac{jke^{-jkr}}{4\pi r}(N_\phi - L_\theta/\eta)$$

$$E_\phi \simeq +\frac{jke^{-jkr}}{4\pi r}(L_\theta - \eta N_\phi) \qquad H_\phi \simeq -\frac{jke^{-jkr}}{4\pi r}(N_\theta + L_\phi/\eta)$$

Transmitarray Antenna Generating CP OAM Beams

Transmitarray Synthesis

RHCP Feed   Spherical Wavefront   Directive Beam   OAM Wavefront   Conical LHCP Beam

Transmission Coefficient T_{RL}

Fabrication and Measurements

$\phi = 90°$ cut

Figure 1.8 Outline of Chapter 5. Orbital Angular Momentum Beams: Novel Mathematical Insights, Transmitarray Generation and Measurement Validation.

the far-field. Therefore, the understanding of OAM's far-field pattern, polarization, phase, etc. can be crucial to establishing effective OAM communications links and understanding inherent limitations; (ii) Analytical or semi-analytical expressions for the OAM far-fields can provide proper guidelines to the design of OAM antennas (an example can be found in the domain of conventional reflector antennas where the analytical formulas of the Airy disk, i.e. the uniform amplitude and phase aperture field distribution, facilitate the antenna design [30, 51]). b) Transmitarrays are proposed as a low-profile antenna that can generate OAM CP patterns using a novel ultra-thin "S-ring" element that supports CP. The resulting transmitarray based on the "S-ring" element is an ultra-thin design that consists of only three metal patterned layers separated by two dielectric substrates.

Finally, chapter 6 concludes this dissertation and discusses future research directions.

CHAPTER 2

3D-Printed Shaped and Material-Optimized Lenses for Next-Generation Spaceborne Wind Scatterometer Weather Radars

2.1 Spaceborne Scatterometers

Hurricanes are among the most powerful natural hazards known to humankind. Wind and water are the twin perils associated with hurricanes and both can be tremendously destructive and deadly. They can wreck homes and buildings, flood cities and damage residential, commercial and public property. Weather radar systems are urgently important to promptly predict the occurrence of these extreme phenomena and give citizens ample warning to securely evacuate the threatened territories. In particular, an article published by Popular Science was entitled "Today's hurricanes kill way fewer Americans, and NOAA's satellites are the reason why" [52]. Wind scatterometer weather radar satellites are instruments capable of measuring the near-surface wind velocity vectors over the earth's oceans and thus predict hurricanes [34, 54]. Fig. 2.1 shows the surface winds generated by hurricane Katrina as observed by the QuickSCAT scatterometer [53]. The arrows indicate the direction of the surface wind while the colors show the speed. One could even say that scatterometers have revolutionized the oceanic wind and short-term warning process as they can be an excellent tool for predicting near real-time winds on the surface of the ocean. This data feeds numerical weather prediction models able to accurately forecast natural hazards, such as hurricanes and cyclones. Fast assessment of hurricanes allows ample warning of mariners near the area at risk [55, 56].
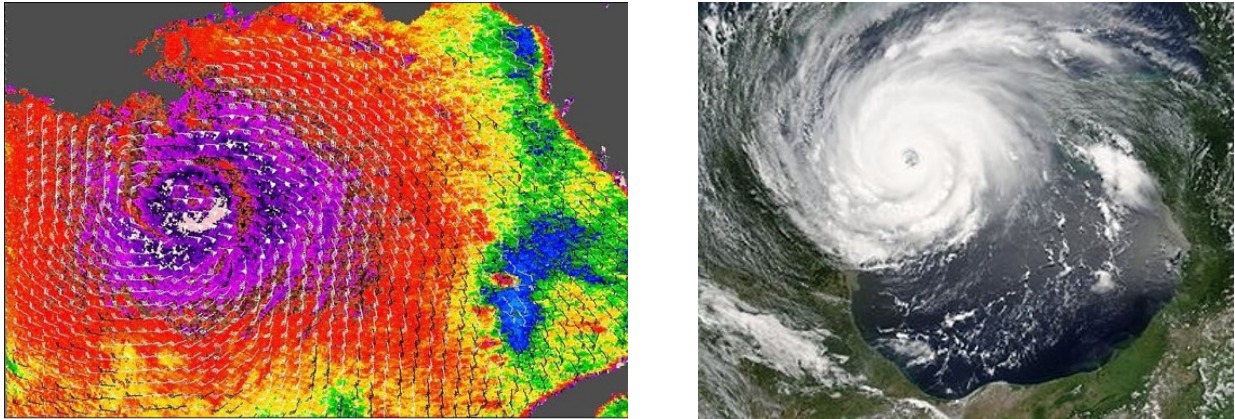
Figure 2.1 Hurricane Katrina. (a) Generated surface winds observed by the QuickSCAT scatterometer. The arrows indicate the direction of the surface wind while the colors show the speed. Courtesy: W. Timothy Liu and Xiaosu Xie, NASA/JPL. [53] (b) Hurricane Katrina at peak intensity in the Gulf of Mexico on August 28, 2005.

The significance of scatterometers extends beyond the prediction of extreme weather phenomena. Scatterometer weather radars produce data of immense scientific value for ocean winds measurements and related applications including weather forecast, ocean usable wind power assessment [34, 57–62], and various additional applications including vegetation phenology monitoring, soil moisture estimation, sea-ice mass freeze and thaw detection in polar regions, amongst others [63–67]. Scatterometer data have been shown to significantly improve the weather forecast accuracy of computer models used by meteorologists and improved methods of assimilating wind data into numerical weather and wave prediction models have been developed [54, 68, 69]. Wind data are combined with measurements from various scientific disciplines to understand processes of global climatic change and weather patterns [70, 71]. This data is vital to scientists in order to improve the ability to fully understand air-sea interaction and ocean circulation, and their effects on weather patterns and global climate [66]. Scatterometer data is also useful in the study of the long-term effects of deforestation on our rain forests, annual and semi-annual rain forest vegetation variations [72], and changes in the sea-ice masses around the polar regions [73–75].

15

2.2 Principles of Operation

Scatterometer satellites carry high gain antennas which transmit a pulse of microwave energy toward the ocean surface and measure the backscattered power. The backscattered power is used to calculate the radar cross section (RCS) σ_0 of the ocean surface, with rough surfaces producing stronger signals than smooth surfaces, as shown in Fig. 2.2(a). A sketch of the scattering geometry is illustrated in Fig. 2.2(b). Incidence angle θ is measured in the plane normal to the mean ocean surface. The angle χ is the azimuth angle between the wind vector and the incident electromagnetic wave. The radar cross section σ_0 is calculated using the basic radar equation [34]:

$$\sigma_0 = \frac{(4\pi)^3 R^4 L P_s}{P_t G^2 \lambda^2 A} \tag{2.1}$$

where R is the slant range to the surface, P_t is the transmitted power, P_s is the received backscattered power, L represents known system losses, G is antenna gain, A is the effective illuminated area, and λ is the wavelength of the transmitted radiation. The noise contribution P_n resulting from the instrument noise and the natural emissivity from the earth-atmosphere system must be subtracted from the total received power to determine the received backscattered power P_s.

The RCS is a function of the surface roughness of the ocean, which in turn is a function of the near-surface winds. Stress to the surface of the ocean caused by the near surface winds cause surface waves to develop and the surface to roughen. In principle, there should be a clear relationship between RCS and wind velocity. However, a theoretical mathematical model describing such a relationship would require an in-depth understanding of the electromagnetic energy-sea surface and wind-wave interactions. The lack of rigorous theoretically based expressions to relate the ocean radar cross section and the near-surface wind necessitates an empirical *geophysical model function*, which in the most general form can be written as:

$$\sigma_0 = fun\left(|U|, \chi, ..., \theta, f, pol\right) \tag{2.2}$$

where $|U|$ is wind speed, χ is the azimuth angle between the incident radiation and the wind
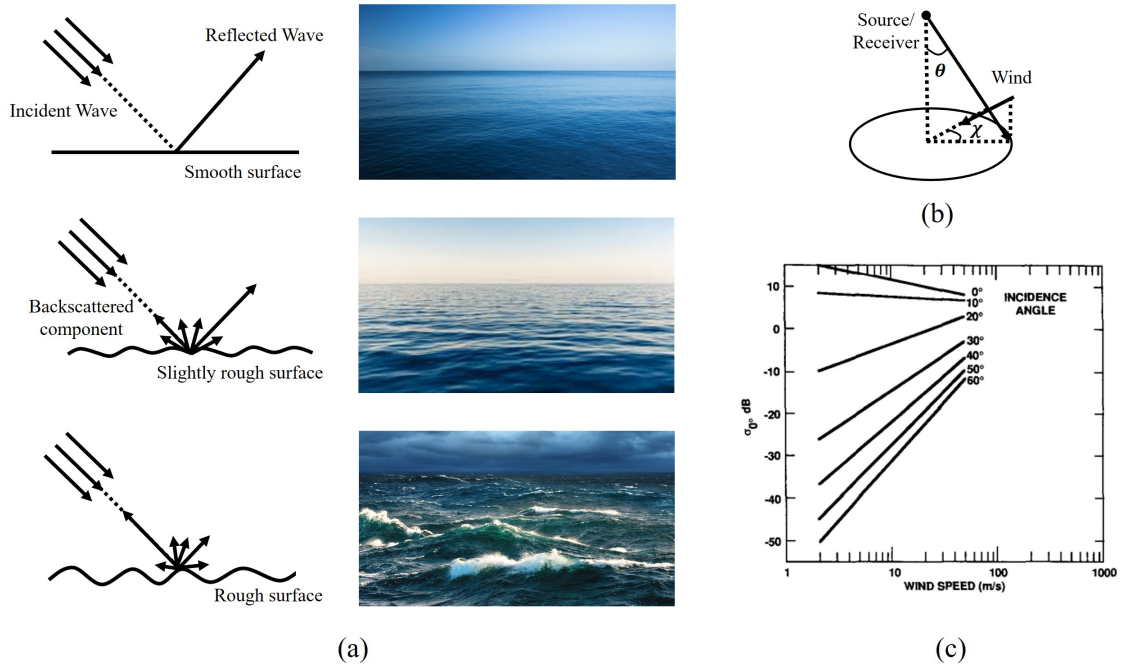
Figure 2.2 Scatterometers principle of operation. (a) Scatterometers transmit a pulse of microwave energy toward the ocean surface and measure the backscattered power. (b) Scattering geometry. The angle χ is the azimuth angle between the wind vector and the incident electromagnetic wave. θ is the incidence angle. (c) Dependence of the normalized cross section and wind speed as a function of the incident angle θ [34]. For $20° < \theta < 65°$, σ is sensitive to wind speed which allows inversion of geophysical model and determination of wind vector.

vector (see Fig. 2.2(b)), ... represents the (small) effects of non-wind variables such as long waves, stratification, temperature, etc., θ is the incidence angle measured in the plane normal to the mean ocean surface, and f and *pol* are the frequency and polarization, respectively, of the incident radiation.

The relationship between the ocean's normalized radar cross section at Ku-Band and the surface wind vector was derived using the 3 months of Seasat microwave scatterometer (SASS) measurements [76–78]. The dependence of the normalized cross section and wind speed as a function of incident angle θ for v-pol radiation and a given azimuth angle χ is shown in Fig. 2.2(c). According to the empirical model function based on the Seasat data, also referred to as SASS-2, σ_0 is weakly sensitive to wind speed for $\theta < 20°$ which makes it extremely difficult to retrieve the wind speed from RCS measurements. On the other hand,

if the incident angle θ is between 20 and 65 degrees, σ_0 is sensitive to wind speed (see Fig. 2.2(c)). Further, empirical studies have also demonstrated that at these angles σ_0 is also a sensitive function of wind direction as measured relative to the radar azimuth angle χ. Therefore, for angles of incidence $20° < \theta < 65°$ the inversion of model (2.2) allows estimation of wind speed and direction.

In order to derive the wind vector from RCS measurements unambiguously, the scatterometer must take multiple measurements along an azimuthal conical scan [33]. Typically, only 4 or more measurements are needed at different antenna azimuth angles to unambiguously invert the geophysical model function and obtain the wind vector [34]. For a single σ_0 measurement (or less than 4 measurements) no unique solution exists for the inversion of eq. (2.2), and the geophysical model function is insufficient to determine both wind speed and direction. Therefore, scatterometer radars should have the capability to obtain data from more than three azimuth angles in a conical scan.

2.3   Scatterometer History

Up to date, scatterometers have provided useful wind observations and many missions have had a successful period of service internationally [54], with NASA's missions being prevalent [79]. Table 2.1 shows a chronicle of NASA's past wind scatterometer missions. NSCAT was launched in 1996 and carried six dual-polarized, 3-meter long, stick-like antennas [34]. Each side of the sub-satellite track contains six wide swath fan beam antennas oriented at different azimuth angles. As the satellite moves over a point on the ocean surface, each one of the six antennas passes over the same spot and takes a measurement at its azimuth angle, as illustrated in Fig. 2.3. Antennas at two azimuth angles take a measurement for both horizontal and vertical polarization resulting in a total of 8 measurements which is enough to unambiguously derive wind vectors from RCS measurements, as explained in section 2.2.

The most recent type of wind scatterometer antenna topology is the spinning spot beam antenna as shown in Fig. 2.4(a), which has been proved to be superior to the fan beam designs [71]. Fig. 2.4(b) shows the QuikSCAT carrying the SeaWinds scatterometer [80, 81],

Table 2.1: NASA past wind scatterometry missions. The QuikSCAT employed a rotating reflector antenna that is revolved about a fixed axis by a mechanical motor. The required moving parts were the single point of failure for the satellite system.

Mission	Period of Service	Frequency	Antenna	End status
NSCAT	1996 - 1997	13.995 GHz	Six dual-polarized, 3-meter long, stick-like antennas	Solar panel failure
QuikSCAT	1999 - 2009	13.4 GHz	Rotating reflector	Mechanical failure
ADEOS II	2002 - 2003	13.4 GHz	Rotating reflector	Solar panel failure
RapidScat	2014 - 2016	13.4 GHz	Rotating reflector	Space station Power failure
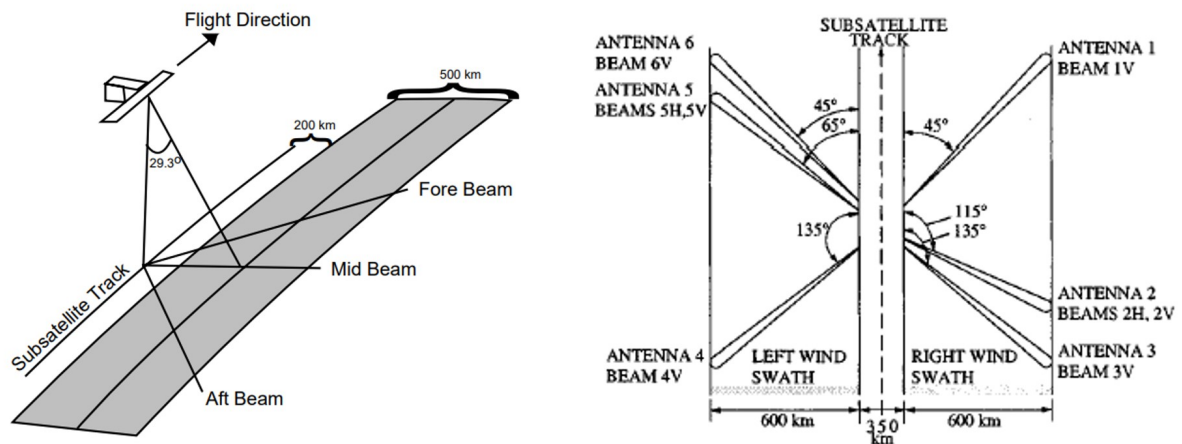
Figure 2.3 NSCAT viewing geometry. The scatterometer carries six dual-polarized, stick-like, fan beam antennas and takes measurements at six different azimuth angles to unambiguously derive wind vector from RCS measurements.

which was launched on June 20th, 1999, to replace its unexpectedly failed predecessor, the NSCAT. To achieve the conical scan, a parabolic reflector antenna is revolved about a fixed axis by a mechanical motor. On November 23rd, 2009, bearing seizure in the rotating mechanism used to scan the antenna caused the satellite to be decommissioned by NASA [82]. The RapidSCAT (Fig. 2.4(c)) was launched on September 21st, 2014 to quickly replace the QuickSCAT and also contained a rotating parabolic reflector antenna [83–85]. This satellite was also decommissioned on November 18th, 2016 due to a power failure on the International Space Station. Weather radar instruments have shown chronic failure due to moving mechanical parts wearing over time. Needless to say, new designs should avoid moving parts and transition to a fully electronic version while maintaining similar performance.

19
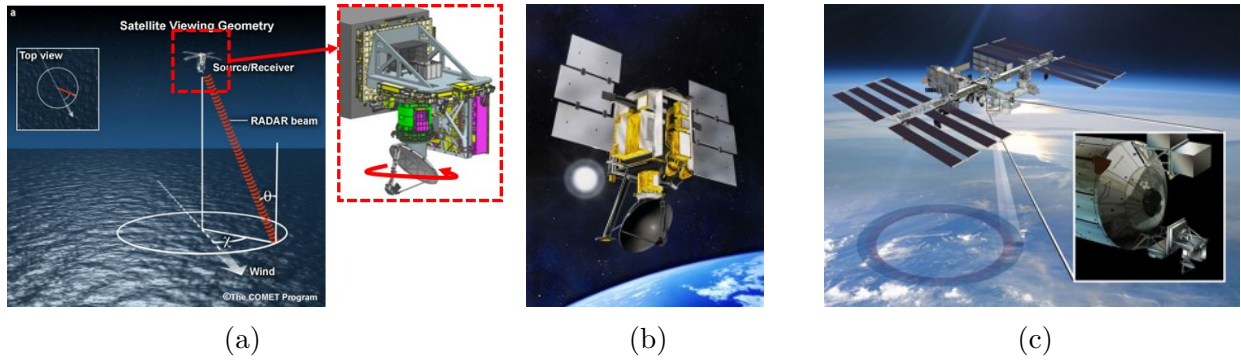
Figure 2.4 Wind scatterometer spinning spot beam antenna topology [86]. (a) A parabolic reflector antenna is revolved about a fixed axis by a mechanical motor to take multiple measurements along an azimuth conical scan. (b) QuickSCAT [80] and (c) RapidSCAT [85].

2.4 Scatterometer Antenna Considerations

Currently, no future NASA scatterometer mission has been planned and, clearly, this is a good time for the development of emerging technologies for next-generation spaceborne wind scatterometers. Bearing the considerations of sections 2.2 and 2.3 in mind, the new antenna design must meet a set of specific requirements:

- **Frequency of operation:** The wind scatterometer should be designed in Ku-Band. All previous NASA missions incorporated radars operating at 13.4 GHz, as shown in table 2.1. The reasons behind this choice are mainly two. First, the backscattered returns in Ku-band are high because they are mostly due to resonant Bragg scattering with wave separation on the order of the radar wavelength. Second, the geophysical model function of equation (2.2), namely the SASS-2, was developed from empirical observations based on the Seasat data in Ku-band [77,78]. Therefore, the retrieval of the wind velocity from RCS measurements using the empirical model is effective at this frequency range.

- **Scanning capabilities:** Typically, the antenna must take multiple (4 or more) RCS measurements along an azimuth conical scan to unambiguously derive the wind velocity vector. The angle of incidence should be in the range $20° < \theta < 65°$, because RCS is sensitive to wind speed for these angles which allows inversion of geophysical model

and determination of wind vector, as explained in section 2.2.

- **Gain and aperture size:** A high gain antenna with large effective aperture is desired, while at the same time the stowage space and weight at the spacecraft should be minimum. In particular, the scatterometer system requires high received backscattered power to increase the signal to noise ration at the receiver endpoint. For a specific orbital attitude and scan angle θ, antenna gain and effective illuminated aperture should increase in order to offset the decrease the received power P_s, since the other quantities in radar equation (2.1) are constant. As an example, the most recent NASA RapiSCAT employed a 0.75 m rotating reflector with 36, 37 dBi gain, 28.3%, 35.6% total efficiency, at 49°, 55.5° incidence angle, respectively.

- **Electronic versus mechanical scan:** The single point of failure for QuickSCAT scatterometer is the moving part of the rotating parabolic reflector. Weather radar instruments have shown failure due to moving mechanical parts wearing over time. Antennas that provide electronic beam scanning with no moving parts would potentially result in designs with higher reliability and longer lifespan compared to conventional rotating reflectors.

2.5   Proposed Solution

The lack of planned NASA scatterometer missions in the near future and the urge for high-performance antennas that meet all the requirements of section 2.4 motivate the objective of this research: The development of novel antennas for next-generation spaceborne wind scatterometer weather radar satellites. Of the few design choices available in the literature, the Luneburg lens can produce the electronic scan in a conical sweep through successive excitation of feeds placed along the body of revolution ring focus, as shown in Fig. 2.5(b) [9,11,18,87–91]. A more lightweight design than the spherical Luneburg Lens that can produce the conical scan is desirable, as shown in Fig. 2.5(c).

Our approach to achieving such a design is a numerical synthesis algorithm hybridizing

Figure 2.5 Conical electronic scanning lens development: 3D-printed shaped and material-optimized slimmed lens produces the conical scan without moving parts.

the curved-ray GO [92], a numerical method for wave propagation in inhomogeneous media, and PSO [93], a global stochastic nature-inspired optimization technique. The algorithm allows the synthesis of the optimal shape and material of the lens, which is then manufactured using 3D-printing technology. The algorithm and its mathematical formulations, the obtained on-axis fed designs and prototypes, and the measurements validating the codes were presented in a series of recent papers [20, 23, 94–96]. This chapter focuses on the design, implementation, 3D-printing fabrication, and measurement verification for the off-axis fed conically-scanned beam version suitable for future wind scatterometers. The novelty of this work lies in the following: a) the application of the conical beam scanning using 3D-printed shaped and material-optimized lenses, b) the customization of the GO-PSO synthesis algorithm, which was previously applied for the design of on-axis fed lenses, for the specific conical
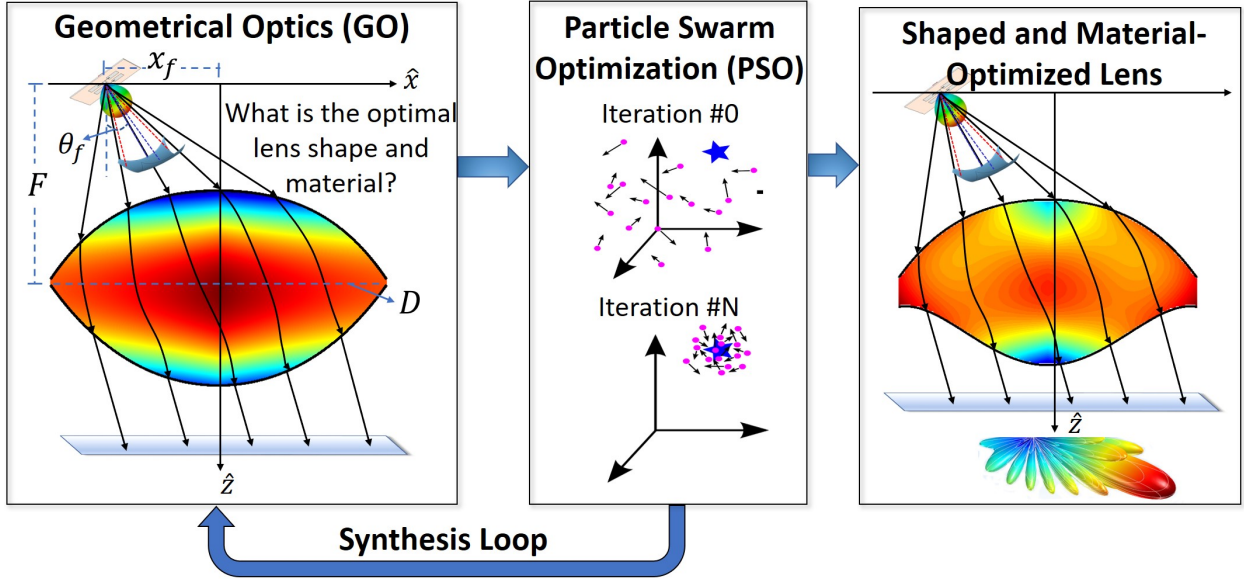
Figure 2.6 High-level flowchart of the synthesis algorithm. GO (GO) is linked with PSO to obtain the lens design with optimized shape and material.

scanning application, and c) the FDM 3D-printing realization, the process used for low-loss space-qualified lens materials such as Ultem [23].

2.6   Lens Synthesis Algorithm Overview

The geometry of the synthesis problem under consideration is shown in Fig. 2.6. A lens is illuminated by a feed that is located at $(-x_f, 0, 0)$ and tilted at an angle θ_f with respect to z axis. The feed is assumed to radiate a spherical phase front. It is $\hat{x}$-polarized and carries a $\cos^q(\theta)$ amplitude pattern. Here, we choose $q = 4.45$, which results in approximately -10 dB and -7.5 dB edge taper for the on axis design and off axis designs, respectively, that are presented in section 2.7. The lens diameter is D and the vertical distance of the feed from the lens center is F. A body-of-revolution symmetry of the lens surface and permittivity parametrization is enforced in order to take advantage of the azimuthal symmetry of the feeds placed along the ring focus that will ultimately produce the electronic conical scan, as shown in Fig. 2.5(c). The same parametrizations are used as in [20], with four parameters for each of the upper and lower lens surfaces and ten samples of the permittivity at ten points in the
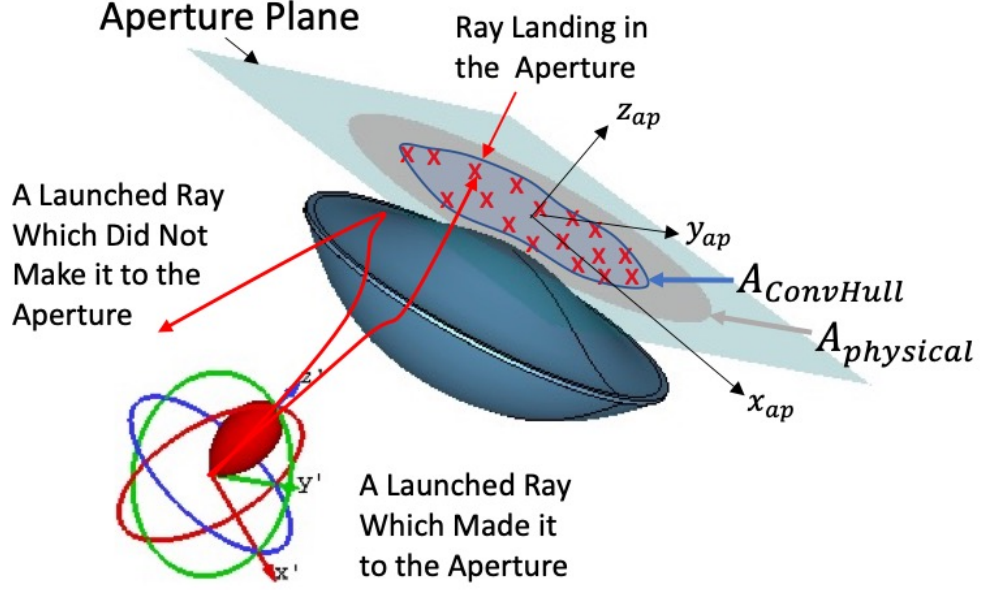
Figure 2.7 Depiction of the terms in the fitness function definition (2.3).

lens cross section, 18 parameters in total. The aperture side and feed side lens shape curves are described by fourth-order polynomials and the relative electric permittivity is described by a third-order polynomial surface (for more details, see [20]). The problem is to determine the shape of the bounding surface and permittivity of the medium filling the inhomogeneous lens to obtain a desired aperture field in the exit aperture plane and hence radiation pattern.

A high-level flowchart of the lens synthesis algorithm is shown in Fig. 2.6. GO [92] is linked with PSO [93] to obtain the lens design with optimized shape and material. A thorough description of the algorithm and the details of its analytical formulations can be found in [20]. For our designs, we choose the fitness function:

$$
\begin{aligned}
\text{fitness} = {} & 2 \times \sigma_{\text{phase}} + 7.5 \times (1 - \text{RayRatio}) + 0.5 \times \text{VolumeRatio} \\
& + 1 \times \sigma_{\text{par}} + 1 \times (1 - \min(\text{AperAreaRatio}, 1))
\end{aligned}
\tag{2.3}
$$

The terms in (2.3) are described with reference to Fig. 2.7. The first term, σ_{phase}, is the root-mean-square error of the linear least squares fit of the phase distribution of the rays in the aperture plane and a desired phase model given by $\Phi(x, y) = \phi_{\text{const}} + k_0 \sin \theta_b \cos \phi_b x_{ap} +$

24

$k_0 \sin\theta_b \sin\phi_b y_{ap}$[1]. This term ensures that the phase of the aperture field has the intended phase gradient for the desired beam scan angle. Note that this term is different from previous works that required beams with a beam peak at $\theta_b = 0°$; therein, $\Phi(x,y) = \phi_{\text{const}}$ and the first term was the standard deviation of the aperture field phase attempting uniform aperture phase [20, 23, 94]. The second term, (1-RayRatio), is the ratio of the actual number of rays which impinged upon the aperture over the total number of launched rays and aims to minimize the totally internally reflected rays. If this term is not minimized, then σ_{phase} may not be a good indication of the quality of the lens; that is, the phase of the aperture field may have the intended phase gradient for the desired beam scan angle but only a few rays may have reached the aperture. The third term, VolumeRatio, is the ratio of the volume of the lens over the volume of a sphere with the same diameter as the lens and aims to minimize the lens volume. This term is necessary to achieve a design with not only high performance but also low volume and therefore mass. The fourth term, σ_{par}, is the sum of the standard deviation of the rays' angle and the mean of the relative difference of the rays' angle and the intended beam peak angle and requires the rays to exit in parallel and in the direction of the intended beam. The fifth and final term is $(1 - \min(\text{AperAreaRatio}, 1))$, where AperAreaRatio is the area ratio of the convex hull of rays at the aperture plane, A_{ConvHull}, over the lens' physical area, A_{physical}, and aims to maximize the effective aperture for high directivity. It is worth mentioning that this term was not included in the fitness function of the on-axis fed homogeneous lens that was presented in [23]. Since the lenses in this chapter are inhomogeneous, the rays curved paths through the lens can force them to bunch up and not fill the aperture leading to poor aperture efficiency. Thus, this term ensures the rays fill the aperture. Note that the AperAreaRatio term was not included in the optimizations of the on-axis fed inhomogeneous 3D-printed lenses in previous works [20], and this term is important especially for the off-axis case. In particular, we attempted to optimize both on-axis and off-axis fed lenses with the same definitions as in sections 2.7.1,

---

[1]The aperture coordinate system (x_{ap}, y_{ap}, z_{ap}) has its origin a quarter wavelength far from the exit aperture of the lens and (θ_b, ϕ_b) are the spherical angles to the intended beam peak as expressed in the aperture coordinate system. ϕ_{const} is a constant phase offset defining the plane to fit the aperture field phase to and $k_0 = 2\pi/\lambda$ is the free-space wavenumber.

2.7.3 without including the final term in the fitness function (2.3) (the first four terms were identical as in sections 2.7.1, 2.7.3). For the on-axis case, the optimization converged to the same design as in section 2.7.1 when the AperAreaRatio was not included in the fitness function. For the off-axis case, the optimization resulted in a lens with a directivity of 24.0 dBi and aperture illumination efficiency (as defined in [25, 97]) of 39.3 % (the directivity and aperture illumination efficiency are 25.5 dBi and 55.0%, respectively, when the final term is included), demonstrating the importance of the new AperAreaRatio term for the off-axis case.

The fitness function in (2.3) resulted from many preliminary optimizations and the lessons learned from the insufficiency of the previous fitness function definitions. Attempts were made through trial and error to develop a fitness function that best represents the relative importance of each goal. As an example, a preliminary optimization with the same definitions as in section 2.7.3 with a relative weight of 0.1 instead of 0.5 for the VolumeRatio term resulted in a lens that achieved a directivity of 25.5 dBi and occupies 61.5% of the volume of a spherical lens of the same diameter. As shown in section 2.7.3, increasing the relative weight of the VolumeRatio from 0.1 to 0.5 resulted in a lens with a similar directivity level of 25.5 dBi and lower volume of 46.7% of the volume of the spherical lens of the same diameter. Further increasing the weight of the VolumeRatio term to 0.9 resulted in lens with a directivity of 24.3 dBi that occupies 43.2% of the volume of the spherical lens of the same diameter, therefore, a weight of 0.5 was chosen considering the trade-off between the achieved directivity and lens volume.

In what follows, the lens diameter[2] is $D = 18$ cm, the focal length is $F = 12$ cm, the operating frequency is $f = 13.4$ GHz (the free-space wavelength is $\lambda_0 = 2.24 cm$). The maximum permittivity is $\epsilon_{r_{max}} = 2.1$, which is the maximum permittivity that can be achieved using the 3D-printed material and unit cell that is described in section 2.8.1.

---

[2]The optimization was run for a $D = 12$ cm diameter lens with focal distance $F = 8$ cm and $F/D = 2/3$ to reduce the GO evaluation time and thus the optimization time. Each optimization is ran for 1000 iterations and is completed in approximately 81 hours. The 12 cm-diameter design is then scaled up to $D = 18$ cm.
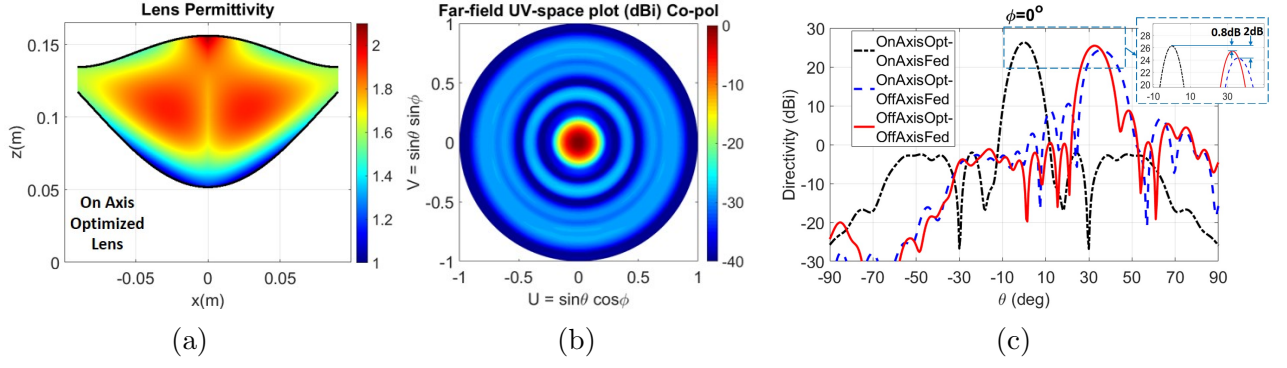
Figure 2.8 18 cm inhomogeneous lens results (f=13.4 GHz): (a) Cross section of the lens that is optimized for on axis performance showing the bounding surfaces and the permittivity of the volume filling the lens. (b) Simulated far-field normalized radiation pattern of the OnAxisOpt-OnAxisFed solid lens. (c) Simulated directivities of the OnAxisOpt-OnAxisFed, OnAxisOpt-OffAxisFed, and OffAxisOpt-OffAxisFed for the E-plane.

2.7 Lens Design and Simulation Results

2.7.1 18 cm On-Axis Lens Design

The algorithm was used to synthesize an on-axis fed lens with a diameter of $D = 18$ cm and $F = 12$ cm at $f = 13.4$ GHz. The feed is placed on axis ($x_f = 0$, $\theta_f = 0$) and the intended beam peak is $\theta_b = 0°$. The obtained design is shown in Fig. 2.8(a). The aperture and feed side surface generating curves $f_{AS}(\rho)$ and $f_{FS}(\rho)$ are described by the fourth-order polynomial functions:

$$f_{AS}(\rho) = +354\rho^4 - 5.54\rho^2 + 0.1560 \tag{2.4}$$

$$f_{FS}(\rho) = -286\rho^4 + 10.40\rho^2 + 0.0517 \tag{2.5}$$

The expansions for the surface generating curves are chosen to be even polynomials so that they exhibit a zero tangent at $\rho = 0$. This ensures the lens is smooth at its apex when the generating curve is revolved about the z-axis. The relative electric permittivity function $\epsilon_r(\rho, z)$ of the inhomogeneous volume filling the lens is described by the 2-D polynomial surface:

$$\begin{aligned} \epsilon_r(\rho, z) = {} & -2.23 + 108z - 73.4\rho + 1840z\rho - 984z^2 \\ & - 942\rho^2 - 9700z^2\rho + 6420z\rho^2 + 3000z^3 + 661\rho^3 \end{aligned} \tag{2.6}$$

27

(a) On Axis Design. (b) Off Axis Design.
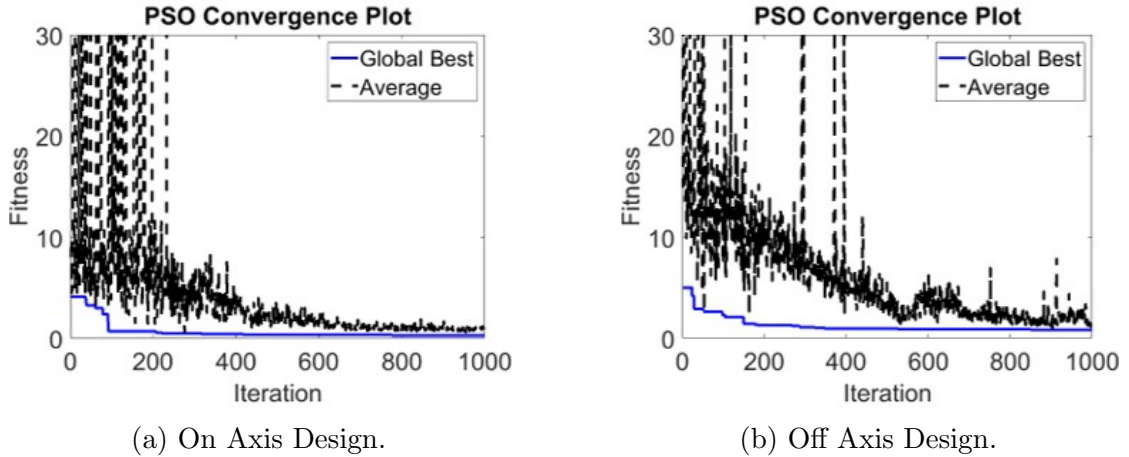
Figure 2.9 PSO convergence plots for the obtained lens designs.

The PSO convergence plot is shown in Fig. 2.9(a). The optimization of 36 particles in total (2 per unknown, see [20] for definitions of the unknowns) and invisible boundaries is run for 1000 iterations with randomly chosen start points for each optimization variable. The optimized lens occupies only 44.8% of the volume of a spherical lens of the same diameter. The lens thickness is 10.4 cm. The final optimization values of the best design in the solution domain are $\sigma_{\mathrm{phase}} = 0.044$ radians, RayRatio $= 1$, VolumeRatio $= 0.448$, $\sigma_{\mathrm{par}} = 0.055$, AperAreaRatio $= 0.965$, corresponding to a fitness function of 0.401.

To validate the approach, the optimized design of Fig. 2.8(a) is simulated using CST MWS full-wave simulation software. CST allows the modelling of the solid inhomogeneous lens with continuously varying material that is described by eq. (2.6). We used the transient solver of CST that is based on the finite integration technique and hexahedral mesh. The feed is placed on axis at the origin and this particular case will be referred to as OnAxisOpt-OnAxisFed as the lens is optimized for on-axis performance and is fed on axis. The lens demonstrates a directional far-field pattern, as shown in 2.8(b). The simulated pattern for the E-plane is shown in Fig. 2.8(c) and the performance statistics are listed in table 2.2. In particular, the simulated directivity of the OnAxisOpt-OnAxisFed lens is 26.3 dBi corresponding to a 66.7% aperture illumination efficiency e_{ap} [25, 97], the half-power beamwidth (HPBW) for E- and H-planes are 8.9° and 8.9°, the sidelobe level (SLL) for E- and H-planes are -28.3 dB and -27.4 dB, respectively, and the beam peak is at $\theta_b = 0°$.

28

Table 2.2:
18 cm solid inhomogeneous lens simulated performance statistics (f=13.4 GHz).

	OnAxisOpt-OnAxisFed	OnAxisOpt-OffAxisFed	OffAxisOpt-OffAxisFed
Directivity (dBi)	26.3 dBi	24.3 dBi	25.5 dBi
HPBW E-plane	8.9°	12.3°	9.9°
SLL E-plane	-28.3 dB	-13.8 dB	-16.7 dB
θ_b	0°	35.6°	32.6°
e_{ap}	66.7 %	42.2 %	55.0 %

2.7.2 The Necessity for Off-Axis Optimization

In general, the lens design that was optimized for particular geometrical parameters (i.e feed position, tilt angle, and intended beam beak) performs best only for these parameters. When the feed is placed at an arbitrary position $(-x_f, 0, 0)$ and/or tilted at an angle θ_f, the performance is degraded and, therefore, a new optimization is necessary in order to restore the performance. To demonstrate this phenomenon, the OnAxisOpt-OnAxisFed lens is now fed off axis and we set $x_f = 7.5$ cm and $\theta_f = 29°$. The latter design is denoted by OnAxisOpt-OffAxisFed hereafter and the simulated E-plane radiation pattern and performance statistics are shown in Fig. 2.8(c) and table 2.2. The directivity drops by 2.0 dB to 24.3 dBi, the E-plane beamwidths broaden to 12.3° from 8.9°, the E-plane sidelobe level has risen to -13.8 dB from -28.3 dB compared to the OnAxisOpt-OnAxisFed lens. In section 2.7.3, we present a new design denoted by OffAxisOpt-OffAxisFed in attempt to restore the performance.

2.7.3 18 cm Off-Axis Lens Design

The algorithm was used to synthesize an off-axis fed lens with a diameter of D $= 18$ cm and F $= 12$ cm at f=13.4 GHz, denoted by OffAxisOpt-OffAxisFed. The feed is placed off axis, and the feed position and tilt angle ($x_f = 7.5$ cm, $\theta_f = 29°$) are chosen for approximately -7.5 dB edge taper. For scatterometer applications, the beam peak has to be greater than 20° to allow the retrieval of the wind speed and direction (see reference [34]) and, therefore, we choose $\theta_b = 33°$as an example. The OffAxisOpt-OffAxisFed lens is shown in Fig. 2.10. The

29
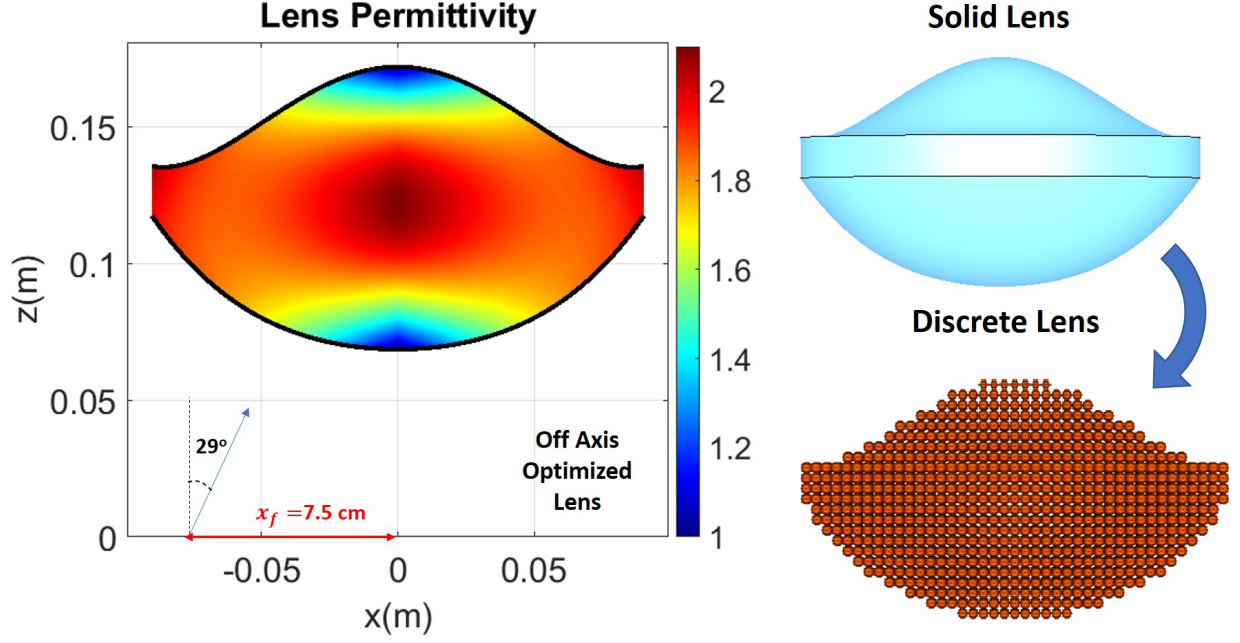
Figure 2.10 18 cm lens optimized for off axis performance and discretization process; the continuously varying material is realized using 3D-printed polymer unit cells of variable sizes.

aperture and feed surface generating curves $f_{AS}(\rho)$ and $f_{FS}(\rho)$ are described by:

$$f_{AS}(\rho) = +672\rho^4 - 9.92\rho^2 + 0.172 \tag{2.7}$$

$$f_{FS}(\rho) = -250\rho^4 + 3.99\rho^2 + 0.0685 \tag{2.8}$$

and the relative electric permittivity function $\epsilon_r(\rho, z)$ is described by the 2-D polynomial surface:

$$\begin{aligned} \epsilon_r(\rho, z) = &-3.18 + 79.7z + 88.9\rho - 1490z\rho - 241z^2 \\ &- 160\rho^2 + 5920z^2\rho + 887z\rho^2 - 469z^3 + 950\rho^3 \end{aligned} \tag{2.9}$$

The PSO convergence plot is shown in Fig. 2.9(b). The OffAxisOpt-OffAxisFed lens occupies only 46.7% of the volume of a spherical lens of the same diameter. The lens thickness is 10.32 cm. The final optimization values of the best design in the solution domain are $\sigma_{\text{phase}} = 0.187$ radians, RayRatio = 1, VolumeRatio = 0.4672, $\sigma_{\text{par}} = 0.16$, AperAreaRatio = 0.8, corresponding to a fitness function of 0.968.

The solid OffAxisOpt-OffAxisFed lens is simulated in CST. The far-field pattern and performance statistics are shown in Fig. 2.8(c) and table 2.2. The HPBW is 9.9°, the SLL

is -16.7 dB, and the beam peak is at $\theta_b = 32.6°$. The simulated directivity is 25.5 dBi, corresponding to an $e_{ap} = 55\%$. Note that the scan loss for this beam angle is 0.74 dB and that the OffAxisOpt-OffAxisFed lens directivity is 0.8 dB lower than the OnAxisOpt-OnAxisFed case and 1.2 dB higher than the OnAxisOpt-OffAxisFed case. After optimizing the lens for off axis feed, we were able to restore part of the performance and lower sidelobe levels, narrower beamwidth and higher directivity were achieved when compared to the OnAxisOpt-OffAxisFed lens.

2.8 Lens Discretization and 3D-Printing Fabrication

2.8.1 Unit Cell and Discrete Lens Simulations

The inhomogeneous permittivity distribution of eq. (2.9) is a continuous function of space. As a necessity to the actual realization, the next imperative step is to discretize the lens. The effective dielectric constant of the unit cell is largely determined by the percentage of the dielectric fill per unit volume [20] and is less dependent on the lattice geometry (cubic, rectilinear, tetrahedral grid, etc.). That being the case, we selected the cubic lattice because it is the simplest way to design the grid and program the 3D-printer. We choose cubic grids each occupying a volume of $(\lambda/5)^3 = (4.48 \text{ mm})^3$, where $\lambda = 2.24$ cm is the free-space wavelength at f=13.4 GHz. The size of the fundamental element of the grid is subwavelength such that the effective medium assumption is valid [88]. The unit cell geometry that was chosen for our design is shown in Fig. 2.11. A cylindrical-type unit cell with variable radius R is supported by a lattice structure consisting of rods of dimensions $s_1 = 0.9$ mm $\times$ $s_2 = 0.4$ mm. This type of unit cell with the specific dimensions can be readily fabricated using 3D-printing technology, as discussed in section 2.8.2.

In principle, the effective permittivity ϵ_r can be tuned by changing the filling ratio of the printed polymer based on the effective medium concept [11], with higher ϵ_r requiring larger printed volume, as illustrated in Fig. 2.11. The 3D-printed polymer is the Polylactic Acid (PLA) with properties of $\epsilon_r = 2.7$ and loss tangent $\tan\delta = 0.01$. The standard
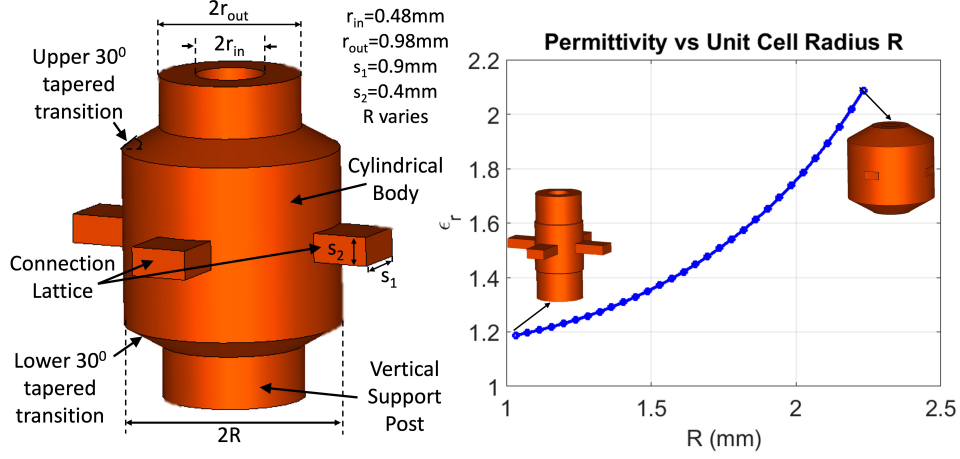
Figure 2.11 Unit cell geometry with dimensions and effective permittivity ϵ_r of the unit cell versus the cylinder radius R; ϵ_r can be tuned by changing R.

electromagnetic parameter retrieval method was used to obtain the relative permittivity of the unit cell versus the cylinder radius R [25]. This method has been proven to provide more accurate results than the fill fraction interpolation (for more details, see reference [20]) that was used in previous works (see for example, [11, 20, 88, 91]). Note that the maximum achievable permittivity $\epsilon_{r_{\max}} = 2.1$ is less than that of the 3D-printed polymer since the largest cylindrical-type unit cell does not occupy the entire volume of the cubic grid. The standard electromagnetic parameter method considers only normally incident waves. To demonstrate the accuracy of the retrieval method and to study the effect of the discretization process, the solid and discrete lenses were simulated in CST. Note that the discrete lens full-wave simulation accounts for the effect of oblique incidence, lens anisotropy, and edge effects. It is worthwhile mentioning that the simulation of the discrete lens is computationally intensive. The computer used for our CST simulations had a 64-bit operating system and 256 GB RAM. A single simulation of the discrete lens was completed in about 13 h and required 29.6 GB of memory, whereas the solid lens ran for approximately 5 minutes and required 1.9 GB of memory. The normalized directivity for the E-plane is shown in Fig. 2.12(b) and the simulated performance statistics are listed in table 2.3. Additionally, the discrete lens is simulated at five distinct feed positions $(-x_f, 0, 0)$, $(0, x_f, 0)$, $(x_f, 0, 0)$, $(0, -x_f, 0)$, and $(-x_f\sqrt{2}/2, x_f\sqrt{2}/2, 0)$ (Positions 1-5) to demonstrate the conical scanning capabilities

32
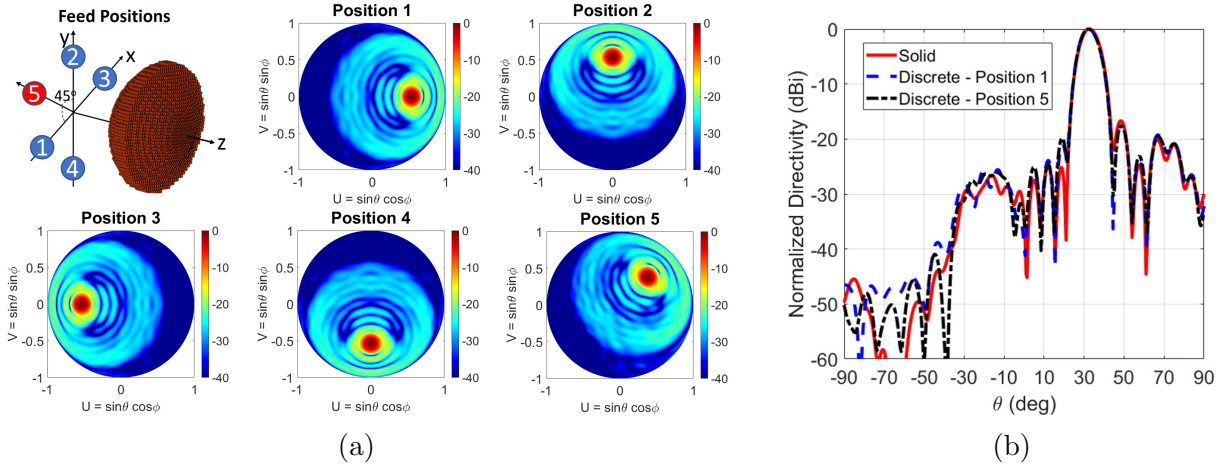
Figure 2.12 18 cm inhomogeneous off-axis fed lens simulation results (f=13.4 GHz): (a) Illustrative figure of different feed positions and simulated conically-scanned radiation pattern. (b) Simulated normalized E-plane patterns of solid, discrete lens with feed at position 1, discrete lens with feed at position 5.

Table 2.3:
Off axis fed 18 cm solid and discrete inhomogeneous lens simulated performance statistics (f=13.4 GHz).

	Solid	Discrete Lens - Position 1	Discrete Lens - Position 5
Directivity (dBi)	25.5 dBi	25.4 dBi	25.3 dBi
HPBW E-plane	9.9°	9.8°	9.8°
SLL E-plane	-16.7 dB	-17.5 dB	-17.5 dB
θ_b	32.6°	32.2°	32.2°
e_{ap}	55.0 %	54.3 %	53.4 %

of the lens and the far-field patterns are shown in Fig. 2.12. The simulation results show an excellent agreement between the solid lens and the discrete lens at all positions, which encouraged the 3D-printing of the lens to obtain measurements.

Since the synthesized lens is based on GO and thus inherently an optical design, the bandwidth is not limited at the design level but rather at the fabrication level. As an example, the same 18 cm lens design with the same $\cos^q(\theta)$ pattern was simulated at 9.75 GHz. The simulated directivity is 23.4 dBi, corresponding to an $e_{ap} = 64.5\%$, demonstrating the broadband features of the lens. Note that the lens discretization process reaches the
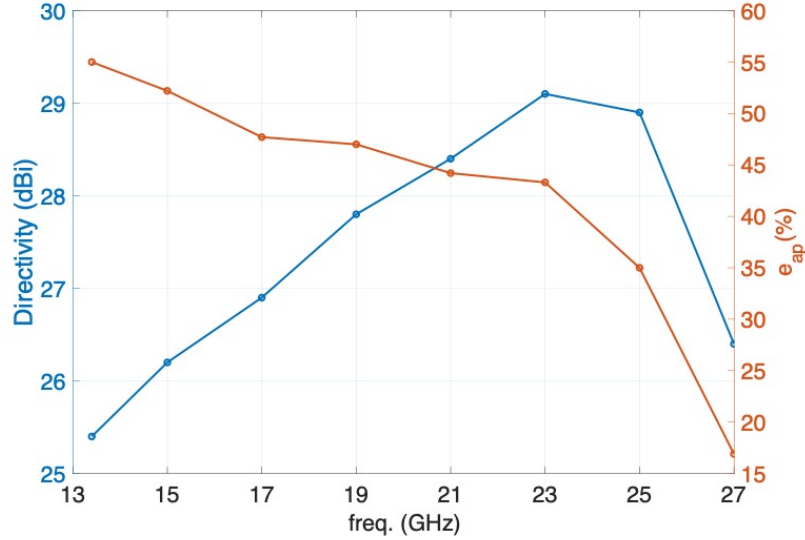
Figure 2.13 Simulated directivity and e_{ap} of 18 cm off-axis fed discrete lenses at various frequencies showing where the effective medium approximation breaks down. As the frequency increases and the unit cell becomes larger in terms of wavelength, e_{ap} decreases and drops from 55% at 13.4 GHz to only 16.9% at 27 GHz.

limits of the effective medium subwavelength unit cell assumption as the frequency increases since the unit cells becomes larger in terms of wavelength. The 18 cm discrete lens design was simulated at higher frequencies using the same $\cos^q(\theta)$ feed. Fig. 2.13 shows the simulated directivities and e_{ap} versus frequency. It can be observed that, as the frequency increases and the unit cell becomes larger in terms of wavelength, the effective medium approximation breaks down and e_{ap} decreases. For example, e_{ap} drops from 55% at 13.4 GHz to only 16.9% at 27 GHz. Note that the unit cell size of Fig. 2.11 is a fraction of 1/5 and 1/2.5 of the free-space wavelength at 13.4 GHz and 27GHz, respectively, i.e., 4.48 mm $= \lambda_{13.4\mathrm{GHz}}/5 = \lambda_{27\mathrm{GHz}}/2.5$. The design, with proper realization techniques, can be pushed from lower to higher bands if needed, as highlighted in [96]. Also, lenses with larger diameters can be obtained using the same design process. In particular, reference [96] reports the fabrication and measurements of a on-axis fed 60 cm lens. The computational resources that were available allowed the scaling of the 18 cm design of Fig. 2.10 up to a 30 cm design. The 30 cm discrete lens was modeled in CST and the simulated directivity was 29.0 dBi, corresponding to an $e_{\mathrm{ap}} = 44.6\%$.

2.8.2   3D-Printing Technique

The lens was fabricated using Fused Deposition Modeling FDM due to its capacity to print high strength flight qualified materials (Ultem and/or PEEK) while also being readily scalable to larger sizes. The most significant downside to the FDM process is its relatively low resolution and requirement for support material under overhangs. For reference, the Objet Eden 350 polymer jetting printer used in [11] states a droplet size of $42\mu m \times 42\mu m \times 16\mu m$ and the reported resolution of the polymer jetting printer in [87] is $40\mu m$. The recommended trace width and extrusion height values from the manufacturer for the Prusa i3 MK3 FDM printer used in this chapter are 0.45mm (or $450\mu m$) and 0.20mm (or $200\mu m$), respectively. For this project these issues have been mitigated though both the design of the unit cell structure (Fig. 2.11) and the lens's natural dimensional robustness. In fact, due to lens design's tolerance to dimensional variations, even occasional unit cell print failures have shown no discernable impact on performance. In learning to optimize the print process, we have had lenses with noticeable defects. In particular, the most frequent defect we have found is 'stringers' – thin lines of dielectric that resembles hair forming a spider web within the lattice. In other cases, we found lattice defects such as a unit cell in which the cylinder appeared to be melted due to power interruptions. Far-field measurements similar to section V of the lenses with defects duplicate results from lenses that do not have print defects to within measurement uncertainty.

The lens's unit cell and lattice structure were specifically designed to accommodate limitations of the FDM process to both improve part quality and enable printing of the high complexity part. For reference, the lens consists of 4305 nodes and takes around six days to print using a standard commercial machine (see Fig. 2.14). With FDM a plastic feedstock is melted and deposited onto a print bed by "drawing" each layer of the part with small line of extruded plastic. This makes designing to the specific extrusion trace width and layer height (0.45 mm and 0.20 mm respectively for this work) very important for high complexity or detailed components. In particular, the unit cell geometry has to be adjusted to be compatible with the printer's trace width and extrusion height. For example, the final
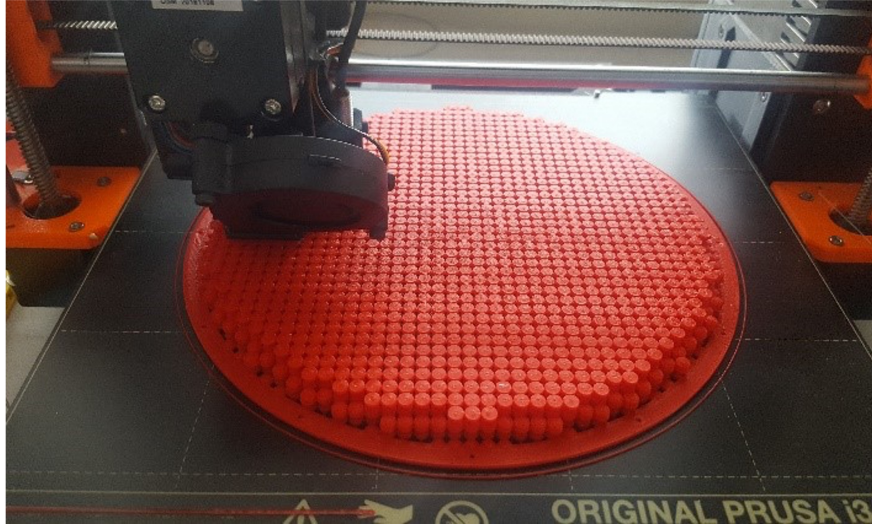
Figure 2.14 Top half of the lens being printed from PLA on a low cost consumer grade 3D printer (Prusa i3 MK3) [98].

unit cell configuration is shown in Fig. 2.11, where the lattice width dimensions ($s_1 = 0.9$ mm and $s_2 = 0.4$ mm) are selected to be exactly two times the trace width and layer height, respectively.

The unit cell implements a printed lattice structure consisting of four elements: cylindrical body, 30° tapered transitions, vertical support posts, and connection lattice (see Fig. 2.11). First, a cylindrical body was chosen to minimize warping that could induce errors during the print process. While a cubic geometry can provide a higher peak fill percentage, and thus dielectric constant, the sharp 90° corners significantly exacerbate warping, resulting in degraded print quality. Second, a 30° tapered transition was added to the bottom of cylindrical cell to allow printing of the overhanging cylindrical body without the need to add sacrificial support material that would have to be removed following the print process. A mirror image 30° tapered transition is also applied to the top surface to maintain symmetry. Next, a vertical support post is used as a pedestal to hold the cylindrical body and 30° tapered transitions. The support post is configured as a 1 mm diameter tube with a wall thickness equal to print trace width (0.45 mm). This configuration prints more reliably compared to a solid, small diameter post. Finally, the x-y support lattice is sized as two print traces wide and tall (0.9 mm × 0.4 mm) to eliminate gaps and slicing errors. A CAD rendering of the

36
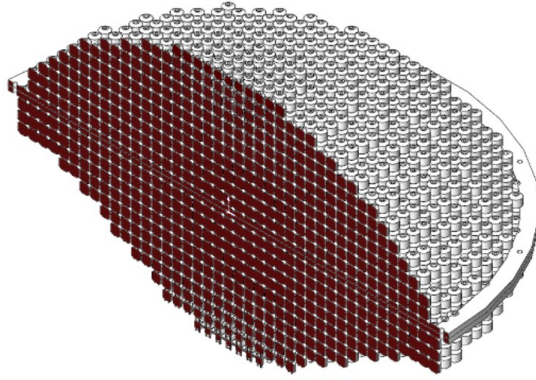
Figure 2.15 CAD section view of the final lens design generated in SolidWorks. The model is split along the center plane into two halves for printing.

final lens design generated in SolidWorks is shown in Fig. 2.15.

The optimized inhomogeneous permittivity gradient in Fig. 2.10 was converted to a node structure based on the unit cell geometry in Fig. 2.11 and design considerations listed above. The lens was printed in PLA with properties of $\epsilon_r = 2.7$ and loss tangent $\tan \delta = 0.01$. It is fabricated in two separate halves to avoid the need for any support material. These halves are then bolted together using an outer support ring that doubles and a mounting point for measurement in the near-field antenna measurement range. The final result is shown in Fig. 2.16 and has a measured mass of 0.915 kg.

2.9   Lens Measurements

The fabricated 3D-printed lens was measured at the NSI near-field spherical range at UCLA. The lens was illuminated by a four-patch array resonant at 13.4 GHz with a measured directivity of 13.4 dBi, which was designed to emulate the $\cos^q(\theta)$ pattern that was used in the simulations of the previous sections. The same feed was used in previous works and showed good results [20, 25, 96]. The mounting apparatus and the measurement setup are shown in Fig. 2.17(a), where three posts are used to support the lens. The feed is placed at position 1 ($x_f = -7.5$ cm, $\theta_f = 29°$), as illustrated in Fig. 2.9. The lens is modelled in CST
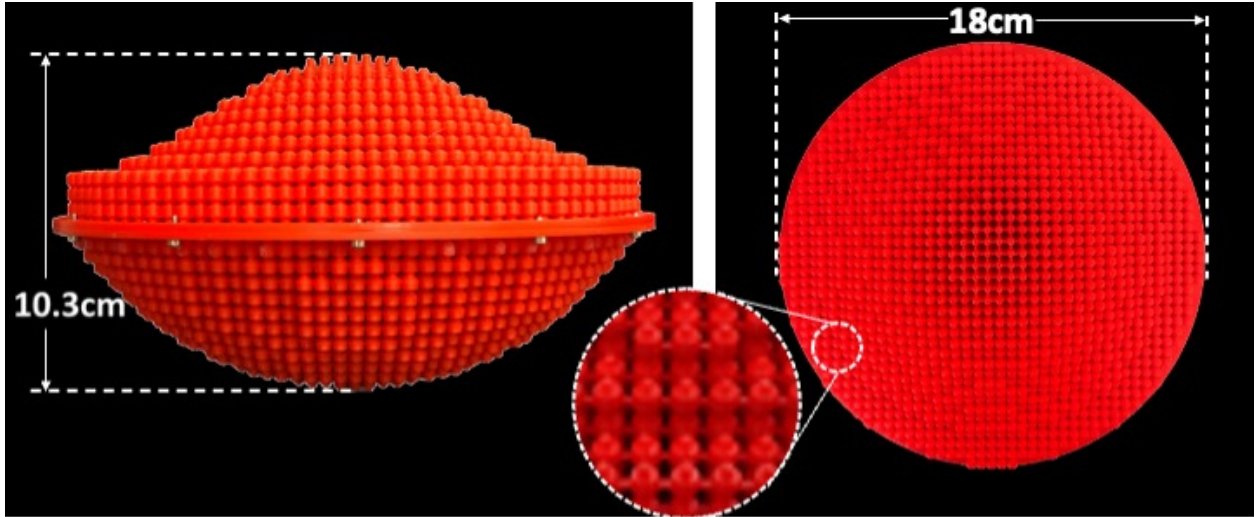
Figure 2.16 Side view, top view, and zoom-in view of the 18 cm 3D-printed lens prototype.

Table 2.4:
Off axis fed 18 cm 3D-printed lens measured performance statistics (f=13.4 GHz).

	Position 1 Simulated	Positions 1-4 Measured Averaged	Position 5 Measured	Position 1 Measured Rotated Feed
Directivity (dBi)	25.4 dBi	25.1 dBi	25.0 dBi	25.2 dBi
HPBW E-plane	9.8°	10.42°	10.55°	9.39°
SLL E-plane	-17.5 dB	-20.6 dB	-20.8 dB	-17.4 dB
θ_b	32.20°	32.42°	32.67°	31.5°
e_{ap}	54.3 %	50.1 %	49.7 %	52.3 %

and a comparison of the simulated and measured radiation patterns is shown in Fig. 2.17(b). The measured cross-polarization level is below -30 dB. The measured directivity is 25.1 dBi and the simulated directivity is a 25.4 dBi. The simulated overall antenna efficiency that accounts for losses from the 3D-printed dielectric radiation, losses from the patch array feed and feed mismatch is 42%, and the simulated total gain is 24.3 dBi. The gain was measured using the gain transfer method and a standard gain horn antenna [99]. The measured gain is 23.7 dBi, corresponding to an overall antenna efficiency of 37%. Overall, very good agreement was found between simulated and measured results, as shown in table 2.4. Discrepancies between the simulated and measured results are attributed to implementation tolerance caused by antenna assembly, misalignment and accuracy of measurements.

To demonstrate the conical scanning beam capabilities of the lens, the feed was placed at
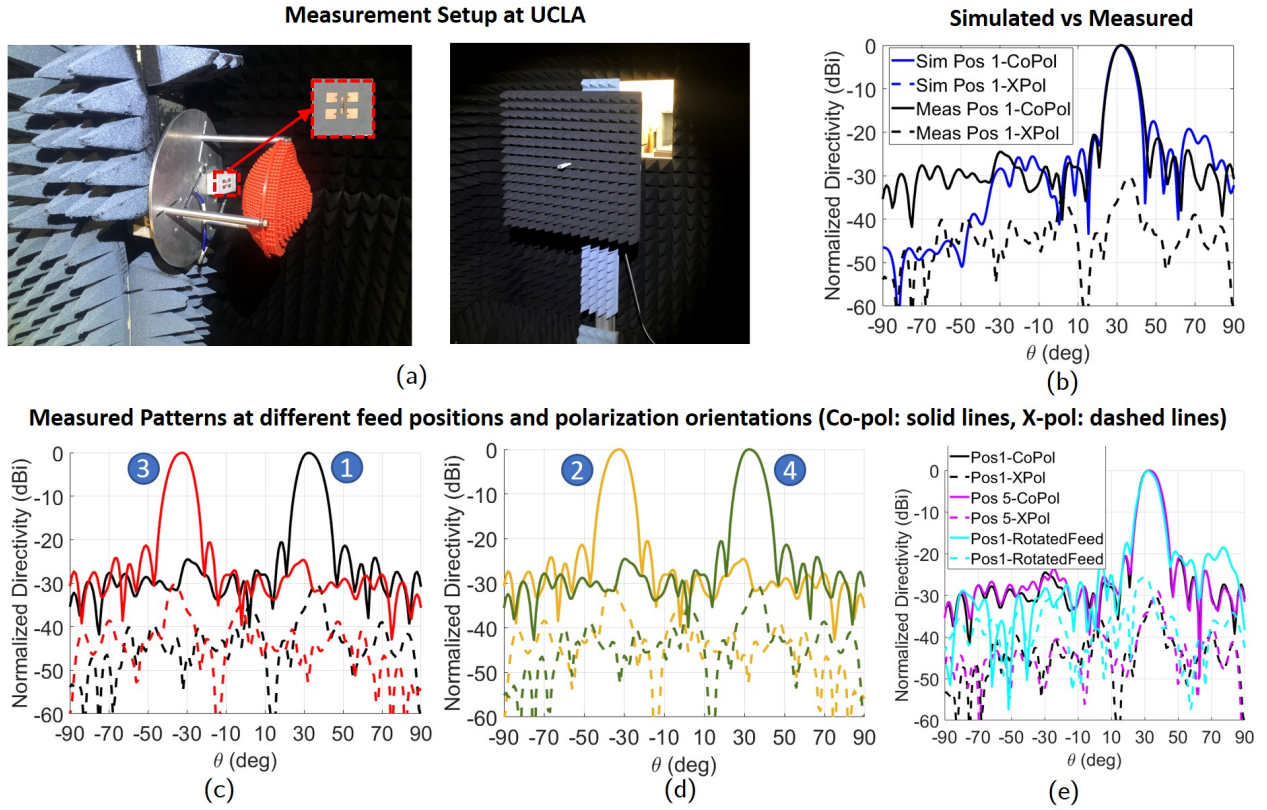
Figure 2.17 18 cm 3D-printed lens measured results. (a) Measurement setup at the UCLA NSI near-field spherical chamber. (b) Simulated vs measured radiation patterns at 13.4 GHz. (c)-(e) Measured E-plane normalized directivity comparison: the feed is placed at position 1-4 (as illustrated in Fig. 2.12), position 5, and is rotated 90° to scan the H-plane of the feed.

positions 2-5. The measured performance statistics are listed in table 2.4 and the measured radiation patterns are shown in Fig. 2.17. The measurements demonstrated that the lens can consistently scan the beam at all distinct locations with a maximum directivity difference of 0.1 dB and maximum beam peak angle deviation of 0.21°. The measurements with the feed placed at locations 2-4 duplicate the results of the lens when the feed is placed at position 1 within measurement uncertainty (the maximum directivity difference for these measurements was 0.05 dB) and have been averaged and placed into a single column in table 2.4. Additionally, the feed at position 1 was rotated 90° along the local vertical axis with respect to the feed to scan along the H-plane of the feed to study the effect of the feed polarization. The measured results agree well with the previous cases where the feed was placed at positions 1-5, as shown in Fig. 2.17 and table 2.4, indicating that the designed lens

antenna can produce the conical scan through successive excitation of feeds placed along the body of revolution ring focus.

2.10   Summary

We presented a novel lightweight 3D-printed shaped and material-optimized lens antenna for spaceborne wind scatterometer weather radars. The 3D-printed lens is designed to contain a ring-type focus which can be populated with individual feed antennas for switched beam type conical pattern sweep of a highly-directive beam. The antenna is designed as an all-electronic replacement for the traditional mechanically driven design. Motivated by real-life application requiring conical beam scanning, our work significantly enhances previous works only addressing the on-axis beam case. Special attention was given to the optimization and prototyping of the lens. The lens was designed using curved-ray GO and PSO. An 18 cm example was designed, 3D-printed using FDM printing process, and characterized through far-field measurements. The measurements prove the conical beam sweep by comparing measurements taken at five locations within the ring focus. The lens can be used in future scatterometer instruments requiring all electronic scanning mechanisms.

CHAPTER 3

Flat-Layered Meta-Lens Antennas: Synthesis, Prototyping and Measurements

3.1 Current State of the Art: Flat-Layered Meta-Lenses

The 3D-printed shaped and material-optimized lens that was presented in Chapter 2 has two main drawbacks: a) 3D-printed lenses are inherently solid and non-deployable and b) one major limitation of 3D-printing techniques is the limited dynamic index range that can be obtained as the permittivity of the polymer provides the upper end of the range. Attempts to realize GRIN lenses using these solely dielectric methods resulted in thick lenses [100, 101]. In order to overcome these disadvantages, the concept of flat meta-lenses resulting into lightweight and slimmed alternatives to the spherically symmetric lenses has recently gained attention [12, 25, 102, 103]. A high-level diagram showing the lens evolution is shown in Fig. 3.1.

Flat meta-lenses are based on the inhomogeneous distribution of the refractive index and are realized using metamaterials [12, 103]. Metamaterials simulate the molecular crystalline lattice in an actual dielectric and are usually formed by a suitable distribution of conducting elements within a host dielectric material [104]. An effective refractive index can be thereby defined which can be tuned by varying the size of the metallic inclusions to form a gradient refractive index medium. In this manner, metal and dielectric are combined such that the index of refraction can be tuned over a greater range than with the dielectric alone. Additionally, advancements in lithography allow us to manufacture metamaterials on demand by simply patterning conducting elements on commercially available dielectric substrates. Metamaterials offer a promising solution for controlling the refractive index in a large range and open the door
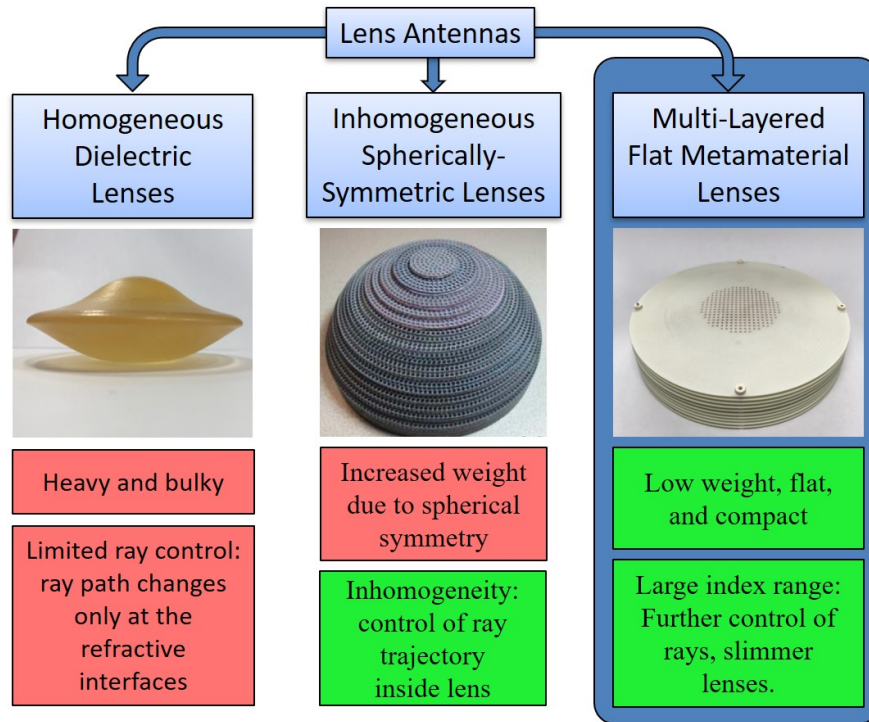
Figure 3.1 Representative classes of lens antennas. In this work, we focus on multi-layered flat metamaterial lenses, which have been proposed as lightweight and thin alternatives to conventional lenses [25].

for the realization of slimmed lenses. Recently, the scientific community has focused on the design and fabrication of slimmed metamaterial-based lenses, also referred to as meta-lenses, which are now conceivable because of the advent of metamaterials and lithography techniques. Flat metamaterial lenses and their analysis, construction and measurement have attracted a lot of attention from antenna engineers (see, for example, references [24, 26, 29, 105–108]). Some representative prototypes of meta-lenses that have been reported in the literature are shown in Fig. 3.2. In this chapter, we present the synthesis, prototyping and measurement of flat-layered meta-lens antennas.

3.2 Meta-Lens Synthesis

The flat meta-lens inhomogeneity synthesis involves two main methods, as shown in Fig. 3.3. The first method to synthesize the flat lens inhomogeneity is to assume that the ray path is
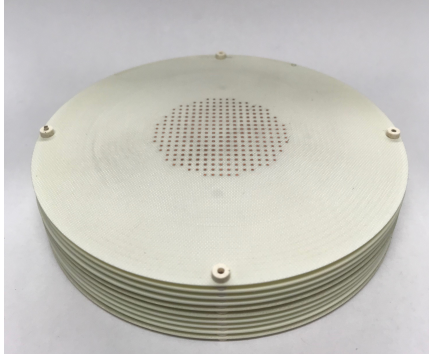
(a) Flat-Layered Metamaterial Gradient-Refractive-Index (GRIN) Lens [25].
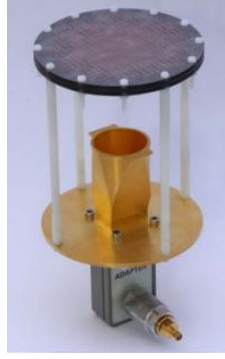
(b) Low-Profile Lens Antenna Based on High-Refractive-Index Meta-surface [24].
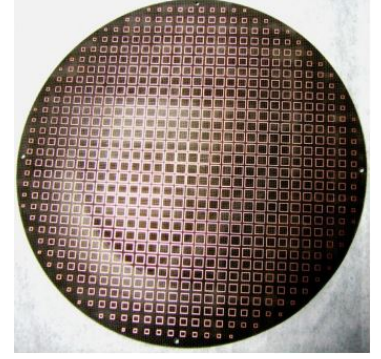
(c) Photograph of a metamaterial layer sample of the lens presented in [26].

Figure 3.2 Representative slimmed flat metamaterial GRIN lens antennas.

straight within the volume of the lens, as discussed in references [24, 102, 109]. According to [24, 102, 109], the straight path approximation can be used to obtain analytical formulas for the refractive index distribution of the lens. This method, however, is approximate and its application is limited to on-axis fed lenses. The second method is a numerical synthesis algorithm that is based on a linkage between GO and PSO, as discussed in detail in [20]. The distinct advantages of the latter method include its applicability for both on-axis and off-axis fed designs and the GO ray tracing for the determination of the ray path rather than the straight ray path approximation. A high-level flowchart of the numerical synthesis algorithm is shown in Fig. 3.4, where GO is linked with PSO to obtain the best meta-lens design.

The configuration of the lens is shown in Fig. 3.3. For the cases studied in Section 3.2, the lens diameter is $D = 12$ cm, the thickness is $T = 3$ cm, the focal distance is $F = 8$ cm, the maximum refractive index is $n_{\mathrm{max}} = 2.6$ (which can be realized using the metamaterial element that was used in [25]), and the frequency is $f = 13.4$ GHz. We will refer to the lens that was obtained using the analytical formula of [24, 102]

$$ n(\rho) = n_{\mathrm{max}} - \frac{\sqrt{\rho^2 + \left(F - \frac{T}{2}\right)^2} - \left(F - \frac{T}{2}\right)}{T} \tag{3.1} $$

as "analytical", where ρ is the axial distance from z axis. Note that the refractive index of

43
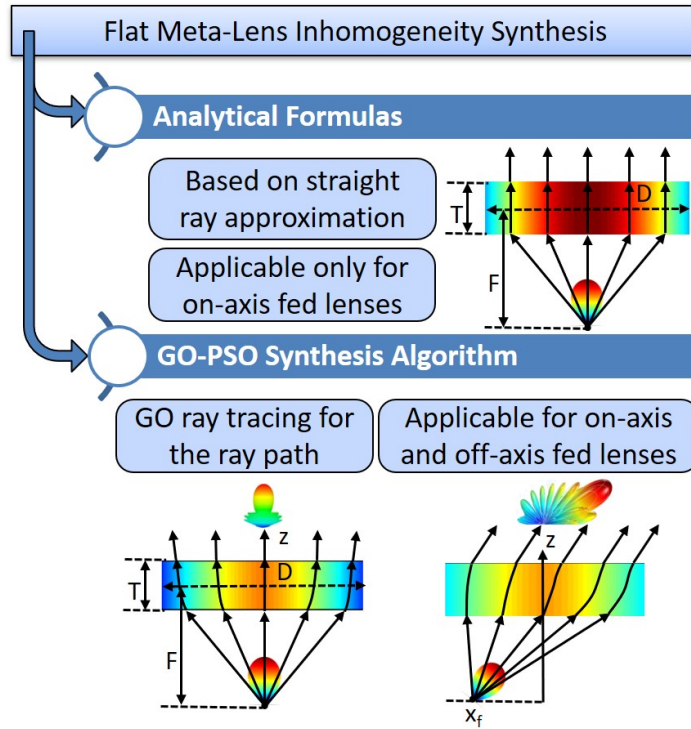
Figure 3.3 Illustration of two flat meta-lens inhomogeneity synthesis methods.
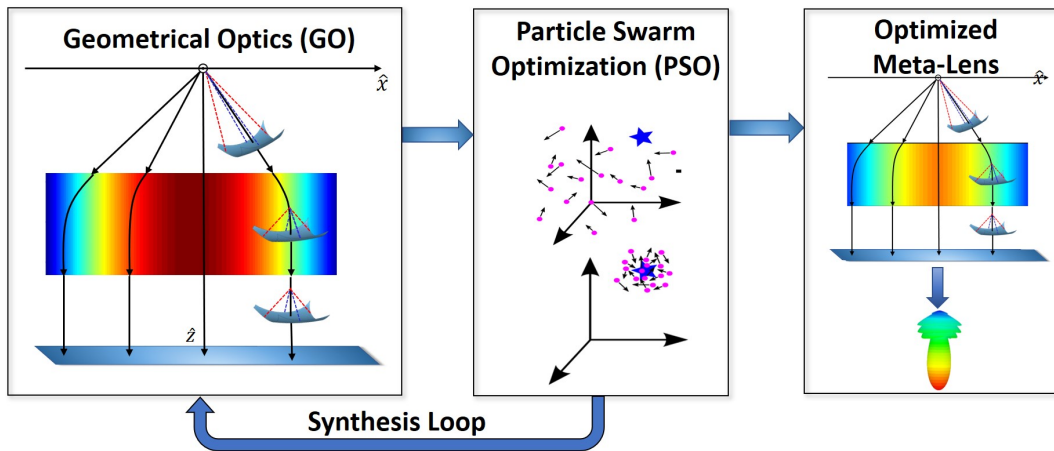
Figure 3.4 High-level flowchart of the numerical synthesis algorithm. GO is linked with PSO to obtain the best flat meta-lens design.

equation (3.1) is dependent on ρ and is constant along z. In order to compare and contrast directly to equation (3.1), the refractive index of the lens is chosen to vary only in ρ and is constant in z according to the following definitions and parametrizations.

44

3.2.1 Definitions and Parametrizations

In what follows, we present several aspects of the GO-PSO synthesis algorithm. An excellent overview of the algorithm can be found in [20]. We use the same feed definitions and lens surface parametrizations as in [94]. The feed is located at the origin and carries a $\cos^{4.45}(\theta)$ amplitude pattern to taper the illumination to approximately -10 dB at the center of lens. It is polarized in the $\hat{x}$-direction and described by the following mathematical equation:

$$\vec{E}(r,\theta,\phi) = \cos^q(\theta)\left(\cos\phi\hat{\theta} - \sin\phi\hat{\phi}\right)\frac{e^{-jkr}}{r} \tag{3.2}$$

Unlike the 3D-printed lens of chapter 2, where the lens profile is shaped, the lens boundaries are flat (to facilitate the prototyping of the lens using flat layers, as discussed in section 3.3) and described by the surface vector:

$$\vec{r}_s(\rho,\phi) = [\rho\cos\phi, \rho\sin\phi, z_c + t_{1,2}] \tag{3.3}$$

where ρ is the axial distance from z axis, $t_{1,2}$ are constants that correspond to the top and bottom surfaces and determine the thickness of the lens. A separate expansion for the lower and upper surfaces of the lens is used and each side can be generated by limiting the domain of the generating curve $z = z_c + t_{1,2}$ to $[0, D/2]$ (D is the lens diameter), and revolving the curve around z axis.

The electric permittivity is defined at N points within the volume of the lens. $N = 10$ points allow for efficient optimization since the algorithm is able to converge while the number of unknowns representing the permittivity is reduced to 10. The lens volume is equally spaced in the radial ρ direction to create a total of 10 uniformly distributed sample points. A curve is fit to these points and is described by the following equation:

$$\epsilon_r(\rho) = \sum_{n=0}^{3} a_n \rho^n \tag{3.4}$$

The body of revolution symmetry allows to revolve this expansion along ϕ to obtain the

45

permittivity distribution within the entire volume of the lens. Note that the permittivity is only ρ-dependent and is constant along z to facilitate the direct comparison with the results based on the analytical formula of equation (3.1). Assuming that the filling material has a permeability close to 1, the refractive index expansion can be found by taking the square root of the permittivity $n(\rho) = \sqrt{\epsilon_r(\rho)}$. Same refractive index profile can be used for the case of materials where μ is not equal to 1 considering that only $n = \sqrt{\mu_r \epsilon_r}$ controls the ray path, electric field phase, and polarization in homogeneous and inhomogeneous media and not ϵ_r and μ_r separately [20].

3.2.2 Particle Swarm Optimization

After the definitions and parametrizations of section 3.2.1, GO ray tracing is used to calculate the electric field in the aperture plane, which is placed a quarter of the free-space wavelength far from the exit aperture of the lens. We choose the fitness function:

$$\text{fitness} = 2 \times \sigma_{\text{phase}} + 7.5 \times \text{RayRatio} + 1 \times \sigma_{\text{par}} + 1 \times (1 - \min(\text{AperAreaRatio}, 1)) \quad (3.5)$$

where σ_{phase} is the standard deviation of the aperture field phase and attempts uniform aperture phase; RayRatio is the ratio of the actual number of rays which impinged upon the aperture over the total number of launched rays and aims to minimize the totally internally reflected rays; σ_{par} is the standard deviation of the rays angle and requires the rays to exit in parallel; the $+1 \times min(1 - \text{AperAreaRatio})$ term aims to maximize the effective aperture for high directivity, where AperAreaRatio is the area ratio of the convex hull of rays at the aperture plane over the lens' physical area. Note that attempts were made through trial and error to develop a fitness function that best represents the relative importance of each goal. The fitness function is the same that was used in section 2.5 of chapter 2.

Lens Statistics	Analytical	Optimized
Directivity	21.0 dBi	23.7 dBi
HPBW E	15.1°	11.2°
HPBW H	15.4°	11.3°
SLL E	-18.6 dB	-25.4 dB
SLL H	-20.2 dB	-25.7 dB
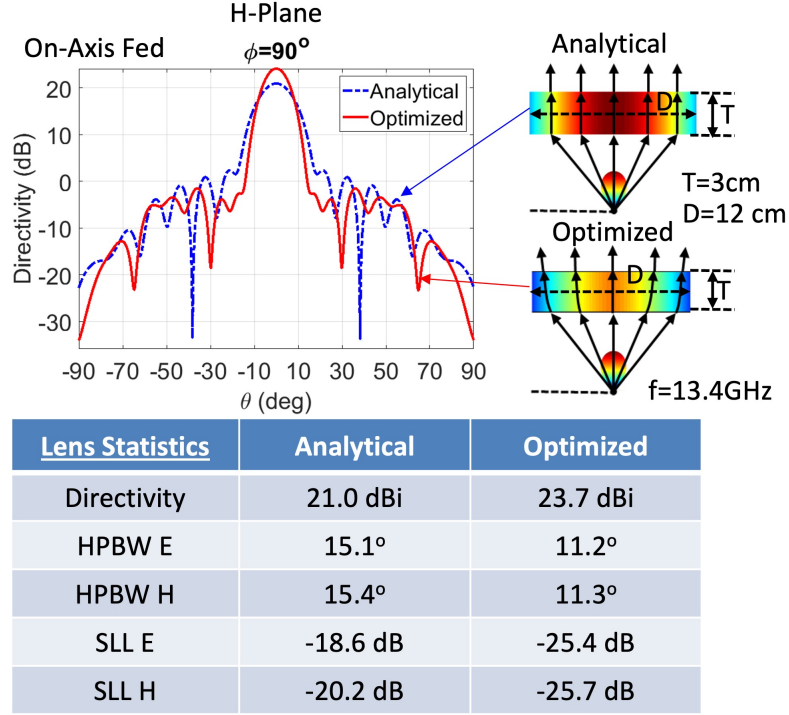
Figure 3.5 On-axis fed simulation results and lens statistics for the optimized lens and the lens based on equation (3.1) and the straight ray path approximation (referred to as "analytical").

3.2.3   On-Axis Simulation Results

The lens synthesis algorithm was used to synthesize an on-axis fed flat meta-lens antenna. The meta-lens diameter is $D = 12$ cm, the thickness is $T = 3$ cm, the focal distance is $F = 8$ cm, the frequency is $f = 13.4$ GHz, and the feed is chosen to taper the illumination to -10 dB at the rim of the lens. The refractive index based on the straight ray path approximation (i.e. equation (3.1) and referred to as "analytical" hereafter) and the optimized index profile are shown in Fig. 3.5. The two lenses are simulated using CST Microwave Studio, and a comparison of the far-field radiation patterns as well as the lens statistics are shown in Fig. 3.5. It can be observed that the directivity of the optimized lens is 23.7 dBi, which is 2.7 dB higher than the analytical case, the beamwidths are narrower, and the sidelobe envelope has dropped. The superior performance of the optimized flat meta-lens is attributed to the accuracy of the proposed algorithm that does not involve any straight ray path approximation.

3.2.4 Off-Axis Simulation Results

A spaceborne application of particular interest is the weather scatterometer radars that measure the ocean vector wind and velocity [23]. The existing scatterometer systems involve a parabolic reflector antenna which produces a conical beam via a motorized scanning mechanism [21]. An alternative solution that avoids moving parts is the off-axis fed flat-meta lens with circular symmetry, where successive excitation of feeds in a focal ring produces the electronic conical scan. In this section, we present off axis-fed flat meta-lens designs with circular symmetry that can potentially be used in next-generation spaceborne scatterometer radars. The on axis optimized lens design of section 3.2.3 is now fed off axis, as shown in Fig. 3.3, and is denoted by OnAxisOpt-OffAxisFed in Fig. 3.6. The feed is positioned $x_f = 5$ cm from z axis, tilted by $\theta = 29°$ and the intended beam angle is $\theta_b = 29°$. Full-wave simulation results showed that the on axis design performs poorly when fed off axis. The directivity drops by 2.3 dB to 21.7 dBi, the E-plane beamwidths broaden to 15° (from 11.2° when fed on axis), the E-plane sidelobe level has risen to -10.6 dB (from -18.6 dB when fed on axis). Therefore, an optimization for off axis feed is necessary in an attempt to restore the performance. The optimized off-axis fed lens is denoted by OffAxisOpt-OffAxisFed and the refractive index profile and far-field patterns are shown in Fig. 3.6. It can be observed that after optimizing the lens for off axis feed, we were able to restore part of the performance. In particular, the directivity increased by 0.7 dB, the sidelobes are lower and the beamwidths are narrower when compared to the OnAxisOpt-OffAxisFed lens.

3.3 Lens Discretization and Prototyping

Once the continuous refractive index distribution of the flat meta-lens is synthesized, the next step towards the realization of the multi-layer lens is the lens pixelization. In particular, the continuously spatially changing refractive index is approximated by discretized steps, where each grid represents a metamaterial unit cell that corresponds to a specific index value, as shown in Fig. 3.7. The refractive index of each unit cell of the discretized lens is mapped to the metamaterial element dimension, with higher refractive index n typically requiring larger
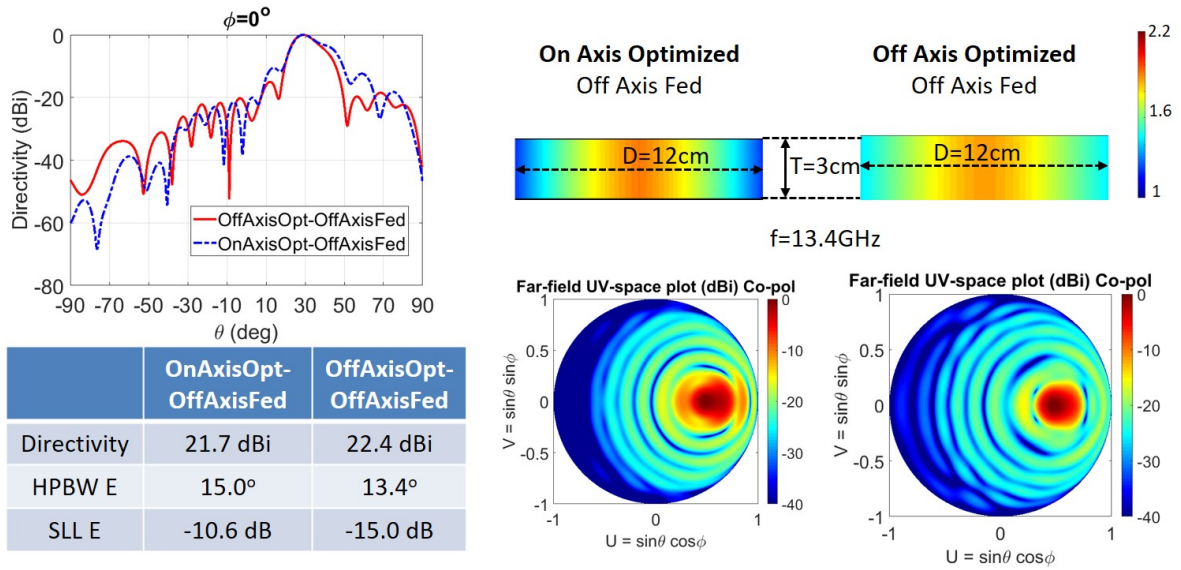
Figure 3.6 Off-axis fed lens full-wave simulation results and statistics for (i) the lens that was optimized for on axis feed and fed off axis (OnAxisOpt-OffAxisFed) and (ii) the lens that was optimized for off axis feed and fed off axis (OffAxisOpt-OffAxisFed).

metamaterial element dimension. In what follows, the continuous refractive index distribution that was adopted in [25] is used to prototype a multi-layered flat meta-lens. Note that the same discretization methodology can be used for different refractive index distributions and for off-axis performance, as discussed in detail in [110]. The lens prototype has a diameter of $D = 11.2$ cm, the thickness is $T = 2.1$ cm, and the focal length is $F = 3\lambda_0 = 6.7$ cm at f=13.4 GHz.

3.3.1 Unit Cell

The first step is to discretize the lens into cubic grids. The size of the fundamental element of the grid is subwavelength such that the effective medium assumption is valid [26, 111]. Each unit cell occupies a volume of $P_x \times P_y \times P_z = \lambda_0/10 \times \lambda_0/10 \times \lambda_0/10$ and is filled with a metamaterial unit cell that corresponds to a specific index value. There are three main aspects to be considered when designing the metamaterial unit cell: 1) The effective refractive index of the scatterers should be able to be tuned to cover the required index range. Namely, the upper index limit is 2.6, which should be achievable by scaling the the unit cell
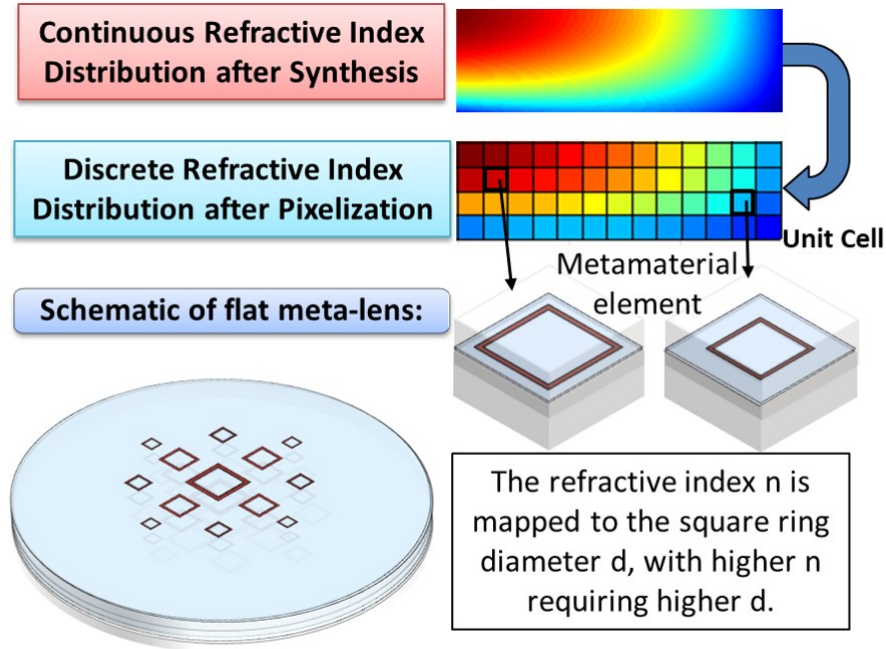
Figure 3.7 Lens Discretization. The continuous refractive index distribution is approximated by discretized steps, where each grid represents a metamaterial unit cell that corresponds to a specific index value.

dimensions. 2) Metamaterials should be utilized in their non-resonant frequency regime such that they exhibit broadband features due to slight index variation and negligible losses, and 3) The configuration of metamaterial layers should allow their arrangement in two modes, i.e. stored/collapsed and operating/deployed, with the first occupying significantly less space than the second. In this section, we present the proposed metamaterial unit cell and explain why this selection is consistent with the above considerations.

The proposed metamaterial unit cell is depicted in Fig. 3.8(a) and (b). It consists of copper closed square-rings of variable sizes distributed on both sides of dielectric substrates. The substrate is the 0.42 mm thick dielectric material RO4350B with $\epsilon_r = 3.48$ and $\tan \delta = 0.0037$. Adjacent dielectric layers are separated by a fixed 1.82 mm air gap. The gap size can be found as we subtract the 0.42 mm thickness of the substrate from the size of the unit cell. The unit cell of the periodic structure is modelled in CST Microwave Studio full-wave simulation software. Periodic boundary conditions are imposed on the right, left, front and
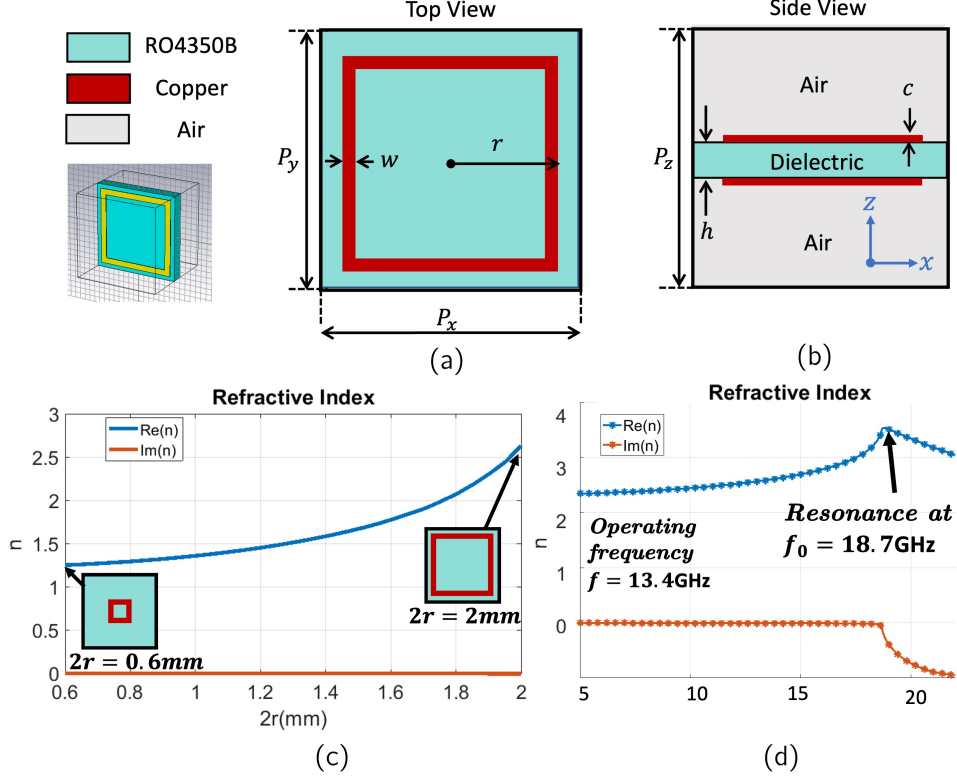
Figure 3.8 (a) Top view (b) side view of the proposed metamaterial unit cell. $f = 13.4$ GHz ($\lambda_0 = 2.24cm$), $P_x = P_y = P_z = \lambda_0/10$, $c = 0.017$ mm, $w = 0.2$ mm, $h = 0.42$ mm. The substrate is the dielectric material RO4350B with $\epsilon_r = 3.48$ and $\tan\delta = 0.0037$. (c) Retrieved refractive indices n of the unit cell as a function of the square ring radius r. (d) The dispersion curve of refractive index of a unit cell with $r = 1$ mm.

rear sides and the structure is excited by a linear transverse electric electromagnetic wave propagating in z-direction, which is modelled using the fundamental TE Floquet mode. The operating frequency is $f = 13.4$ GHz. The effective refractive index is obtained by the standard electromagnetic parameter retrieval method for different square ring sizes r. The effective refractive index n can be calculated from the S parameters using the following relation [112–114]:

$$n = \frac{1}{k_0 d} \cos^{-1}\left[\frac{1}{2S_{21}} \left(1 - S_{11}^2 + S_{21}^2 \right) \right] \tag{3.6}$$

In the above equation, $k_0 = 2\pi/\lambda_0 = \omega/c$ is the wavenumber of the incident wave. In general, S_{11} and S_{21} are complex numbers, so using (3.6) in determining n yields a complex number. For the case studied hereafter, the imaginary part of n is negligible ($|Im(n)| < 0.005$) and

51
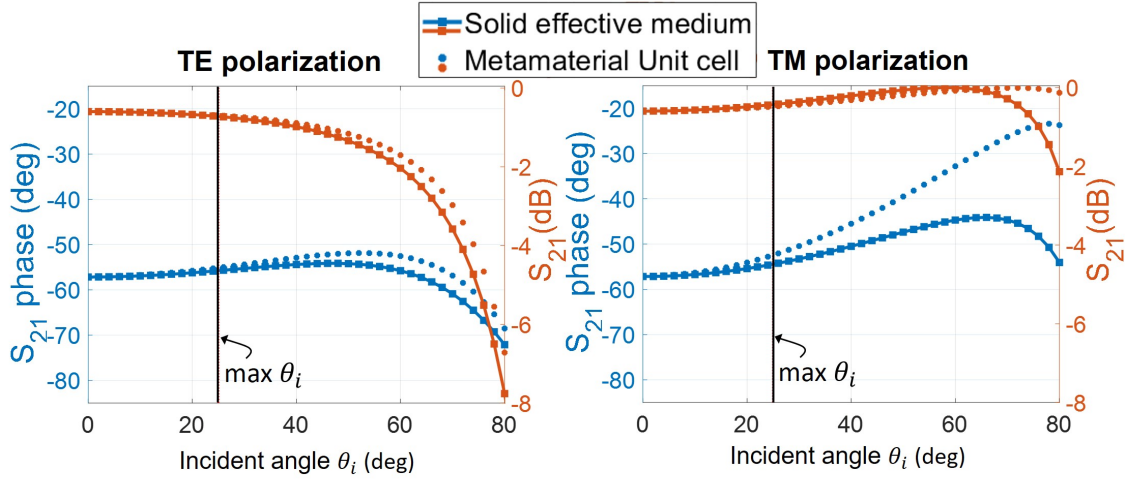
Figure 3.9 Simulated transmission coefficient S_{21} of a metamaterial element with radius $r = 0.7$ mm and a solid unit cell with same effective electromagnetic parameters to illustrate the oblique incidence and polarization effects on the element performance. The maximum angle of incidence with respect to the normal to the metamaterial unit cell for the configuration of the lens of this chapter is 25 degrees.

therefore neglected. The standard electromagnetic parameter retrieval method considers normally incident waves. Rays yet enter the lens at different angles and polarizations. The angle of incidence θ_i of each ray with respect to the normal to the metamaterial unit cell for the configuration of the lens of this chapter varies from 0 degrees (for the largest square ring with $r = 1$ mm that is located at the center of the lens) to approximately 36 degrees (for the smallest square ring with $r = 0.3$ mm that is located close to the rim of the lens). Fig. 3.9 shows the simulated transmission coefficient S_{21} of a metamaterial element with radius $r = 0.7$ mm and a solid unit cell with same effective electromagnetic parameters for TE/TM polarization versus angle of incidence θ_i. A vertical line has also been added to pinpoint the maximum incident angle with respect to the normal to the metamaterial unit cell. The maximum S_{21} phase error for the rings with $r = 0.7$ mm is 0.7 degrees for TE polarization, and 2 degrees for TM polarization. Additional simulations for various ring sizes showed that the maximum S_{21} error occurs for the ring that was selected in Fig. 3.9. The illustration of oblique incidence and polarization effects on the element performance together with the simulation results of the next section demonstrate that the standard electromagnetic

Table 3.1:
Comparison of our proposed unit cell with other unit cells.

	Proposed unit cell: double-sided square ring	One-sided square ring [26]	3D-printed [20]
Maximum refractive index	2.6	2	1.64
Continuous lens thickness	$1.1\lambda_0$	$2\lambda_0$	$2.7\lambda_0$
Layers after discretization	10	19	-

parameter retrieval method gives good results for the subtended angle of the lens and the ratio F/D used in this chapter.

As illustrated in Fig. 3.8(c), it can be observed that by tuning the length $2r$ from 0.6 to 2 mm, the refractive index varies from 1.2 to 2.6, thereby realizing the meta-lens inhomogeneity. Note that this dynamic index range is considerably larger than that achieved by other artificially engineered materials such as 3-D printing polymers [10, 11, 19, 20, 23], drilled-hole approach on commercial dielectric boards [12, 115, 116], and other metamaterials that combine metals with dielectrics [111, 117]. Table 3.1 shows a comparison between the proposed unit-cell architecture and other cited unit cells. In [20], the upper index range of the 3-D printed polymer is 1.64 which corresponds to a $2.7\lambda_0$ lens thickness, and the 3-D printed lens would not be collapsible but rather inherently solid and non-deployable. In [26], one-sided copper square rings were used for the realization of a GRIN lens. The maximum achievable refractive index using this element and same dielectric panels and dimensions is 2 which results in a lens thickness of $2\lambda_0$ and 19 layers. The proposed double-sided square ring element is advantageous in terms of the larger maximum achievable index value of 2.6 that reduces the lens thickness and number of required layers.

To demonstrate the advantages of the proposed metamaterial in terms of bandwidth, the extracted refractive index of a unit cell with $r = 1$ mm is plotted in Fig. 3.8(d) versus frequency. As the unit cell radius becomes larger, the resonance frequency decreases and the dispersion curve is less stable around the resonance frequency. Fig. 3.8(d) shows the largest

unit cell that has the lowest resonance frequency. It can be observed that the dispersion curve undergoes an electrical resonance at $f_0 = 18.7$ GHz. Below resonance frequency, the real part of the refractive index monotonically increases and the imaginary part is close to zero which indicates low-loss. Hence, working in the non-resonant region allows us to control the refractive index throughout the lens over a broad frequency range. It should be emphasized that the utilized metamaterial is different from transmitarrays [116], Zero-Index materials (ZIM) [118], and Low-Index materials (LIM) [119], which usually comprise elements operating efficiently in the tail of their resonances and suffer from very low bandwidth.

Further, the choice of the proposed metamaterial unit cell facilitates lens compression. In particular, adjacent dielectric layers are separated by a fixed 1.82 mm air gap in operational mode, and can be collapsed by eliminating the air separation to minimize storage space. That allows the lens to be stowed collapsed in the form of stacked substrates and expand when functioning. The collapsed lens occupies significantly less height in storage configuration than the deployed lens in operational mode, with a thickness which is equal to $0.19\lambda_0$ reduced by roughly five times with respect to the expanded case. Note that the outermost top and bottom rows of discrete unit cells correspond to a refractive index equal to 1. Therefore, these layers are omitted and the total number of 12 layers is reduced to 10. More details on the realization of the unit cell within fabrication tolerances and the actual manufacturing are provided in section 3.3.2.

3.3.2 Lens Fabrication

The lens layers were constructed on 0.42 mm thick Rogers 4350B copper coated substrate. A PCB substrate solution was adopted because of the high quality and low cost of modern commercial PCB manufacturing and milling services. The Rogers 4350B material used in this work has low loss ($\tan\delta = 0.0037$) and stable dielectric constant of 3.48 over the band of interest and is one of the cheapest RF materials available. The lens layers were fabricated in a standard double-sided PCB milling process provided by Cirexx International Inc. The copper patterns were produced by means of a wet etch process in which the undesired copper
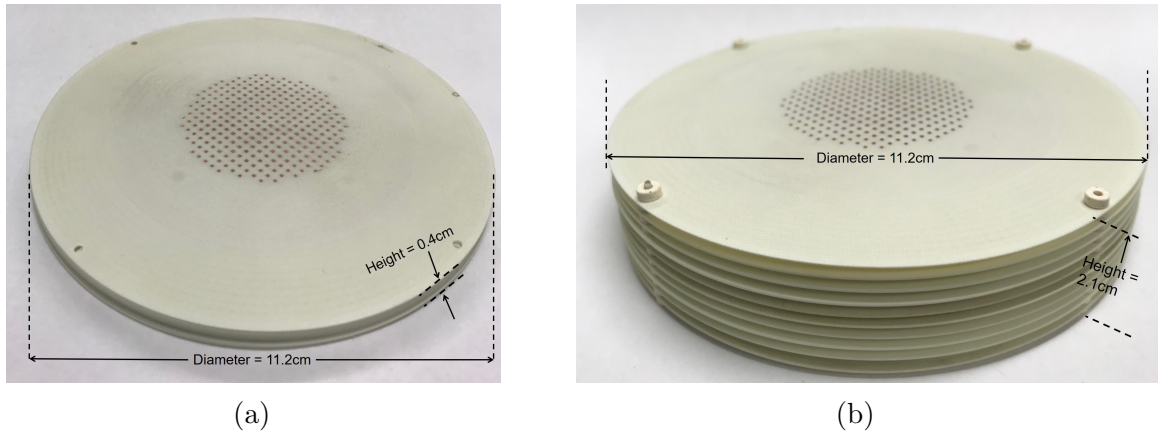
Figure 3.10 (a) Fabricated folded lens when collapsed. All lens layers stacked without rods and spacers; the height is 0.4 cm. (b) Fabricated unfolded lens in operational configuration. Lens fully assembled with rods/spacers and deployed; the height is 2.1 cm.

is removed by acid.

The lens structure is rigidly supported by 1.6 mm diameter acrylic rods which pass through the guide holes in each layer. Nylon spacers, each 1.82 mm thick, maintain the correct inter-layer spacing. Rogers 4350B is one of the stiffest available dielectric materials with very high tensile modulus, and four rods and spacers are sufficient to maintain stable different layers. These dielectric components are kept discreet and are positioned near the low edge illumination taper area so as to limit their electromagnetic interference. The air gap, which is equal to the thickness of the spacers, can be found if we subtract the dielectric layers' thickness from the unit cell size. The lens layers, stacked and without support rods, are shown in Fig. 3.10(a). The total thickness of the layers when dissembled is 0.4 cm. The fully built up lens with rods/spacers inserted is shown in Fig. 3.10(b). In this configuration, the lens stands at 2.1 cm (not including the spacers on top and bottom). The proposed constructed lens can be collapsed and deployed by hand. This gives rise to a compact design (occupies 80% smaller volume compared to the unfolded state), which can be conveniently transported and deployed in the unfolded state. Collapsing both the feed and the lens can be advantageous to increase the absolute space saving factor. In particular, if the feed is PCB-based, and the lens is also formed by flat-layered dielectric substrates, the feed can be collapsed together with the lens and stowed in the form of stacked PCB substrates to

	Homogeneous 3-D printed lens	Inhomogeneous 3-D printed lens	Flat-Layered Meta-lens
Height (cm)	5.2 cm	5.2 cm	2 cm deployed 0.42cm collapsed
Mass (grams)	96 g	87 g	79 g
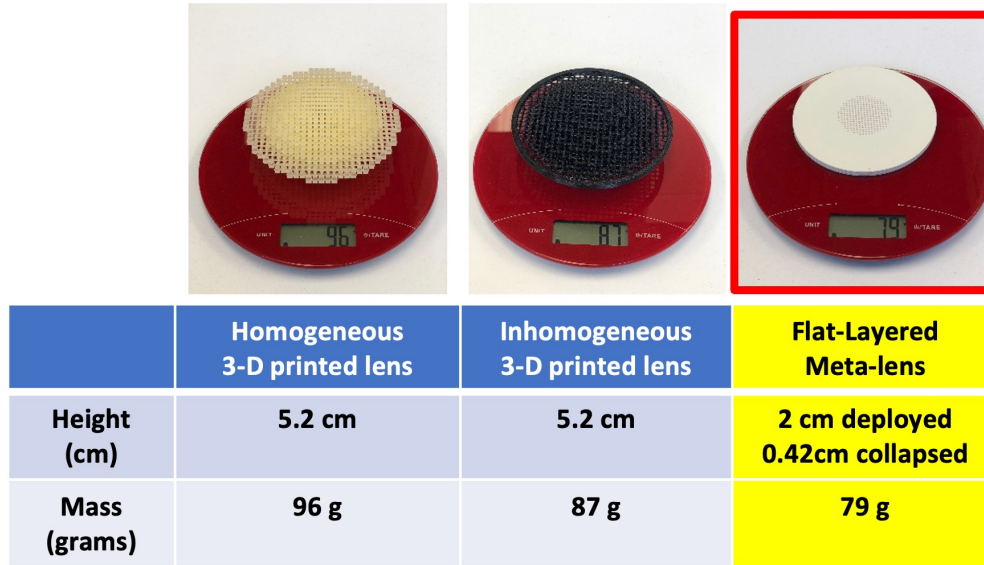
Figure 3.11 Weight and height comparison of 3D-printed lenses that were reported in [121] and the fabricated meta-lens of Fig. 3.10. All lenses operate at 13.4 GHz, and the 3D-printed lenses have a diameter of 12 cm.

reduce the distance and thus the total packaging height. Note that the idea of collapsing the feed and the wavefront transformation device to reduce the focal distance of the collapsed structure has already been studied for the case of reflectarray antennas (see, for example, reference [120]) and here we focus on the original collapsible lens concept.

It should be emphasized that weight reduction is an additional advantage of this new lens. The volume of the excessively heavy dielectric was minimized and thin dielectric layers were used as a host to support conducting elements. In particular, the weight of the fabricated prototype is 79g, while a solid lens of the same dimensions and dielectric material would weigh 381g. This weight can be further reduced if one takes away the surrounding dielectric section beyond the printed metamaterial features at each of the layers. In other words, not only is the proposed lens roughly five times lighter than the solid analogue of the same dielectric material, but it also occupies ~ 5 times less volume when collapsed in height for packaging purposes. Fig. 3.11 shows a weight and height comparison of the flat-layered meta-lens and the 3D-printed lenses that were reported in [121] for on-axis beams. All lenses operate at 13.4 GHz and the 3D-printed lenses have a diameter of 12 cm. It can be observed that the meta-lens height and weight are reduced when compared to the 3D-printed lenses.
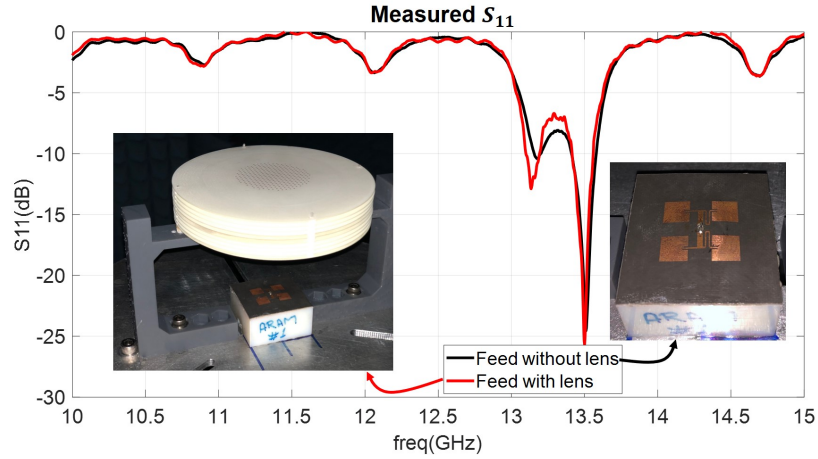
Figure 3.12 Measured reflection coefficient S_{11} of the resonant 4-patch array feed with and without the lens. The frequency of interest is 13.4 GHz.

3.3.3   Meta-lens Measurements

The fabricated meta-lens was affixed in the UCLA Plane Bi-Polar Near Field measurement range [122] and was illuminated by a 4-element patch array resonant at 13.4 GHz with 13.43 dBi of measured directivity. This radiator is designed to emulate the feed source described by (3.2) which gives a -10 dB edge taper at the angle of 36.7 degrees. The same feed was used in the previous works [20, 21, 23, 25] where similar ratio F/D was kept and showed good results. The measured reflection coefficient S_{11} of the resonant 4-patch array with and without the presence of the lens is shown in Fig. 3.12. The measured reflection coefficient of the feed is almost unaffected by the presence of the lens.

The mounting apparatus and the measurement setup inside the anechoic chamber are shown in Fig.3.13(a), where two dielectric posts rigidly support the lens at the required distance from the feed. The lens antenna illuminated by the resonant four patch array was also modelled using CST Microwave Studio transient solver. Simulated and measured far-field patterns resemble well for both E-plane and H-plane in terms of directivity and half-power beamwidth, as shown in table 3.2. The radiation pattern comparison is shown for the H-plane in Fig. 3.13(b) demonstrating the consistency between full-wave simulation and measured results. The measured sidelobe levels are -20.5 dB and -18.8 dB, and the 3-dB beamwidths
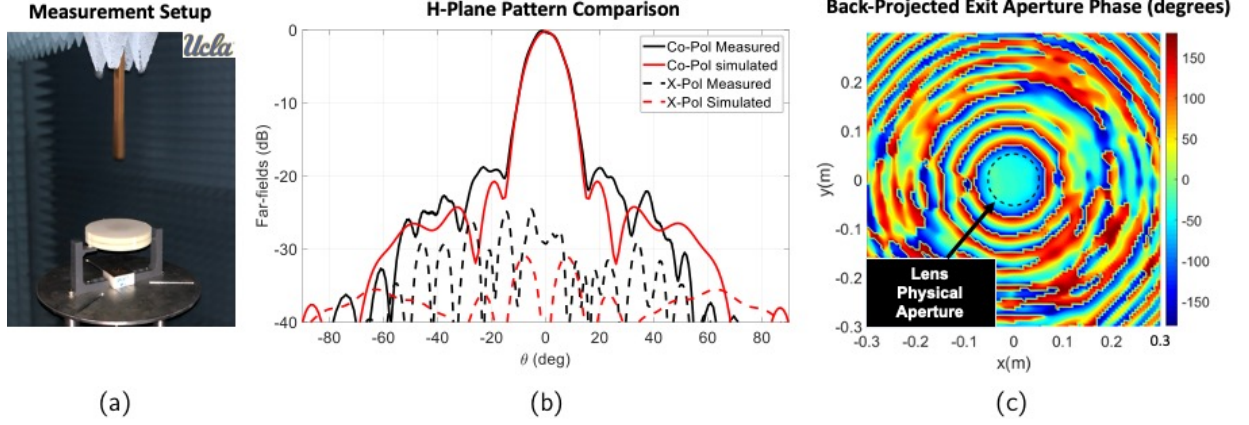
Figure 3.13 (a) Lens measurement setup in the UCLA Plane-bipolar Near-Field measurement range. (b) Simulated and measured radiation patterns of the proposed lens antenna. (c) Back-projected measured exit aperture phase.

are 13.8° and 12.2° for E-plane and H-Plane, respectively. The cross polarization level is below −24 dB for both principal planes and the measured directivity is $\mathcal{D} = 23.06$ dBi. The simulated sidelobe levels are −22.6 dB and −20.5 dB, and the 3-dB beamwidths are 12.9° and 12° for E-plane and H-Plane, respectively. The cross polarization level is below −30 dB and −35 dB the simulated directivity is $\mathcal{D} = 22.73$ dBi. Discrepancies between simulated and measured results of Fig. 3.13(b) and table 3.2 are attributed to implementation tolerance caused by antenna assembly, misalignment and accuracy of measurement. Note that the valid angle for the near field measurement was 60 degrees. To further assess the performance of the lens antenna and provide an insight into the high directivity, the measured near field that was captured at the probe plane location was back-projected to the exit aperture of the lens. The field phase distribution is illustrated in Fig. 3.13(c). The phase uniformity inside the physical aperture area of the lens is a manifestation of the transformation of the spherical wave emitted by the feeding source into plane wave.

Another key parameter that measures the lens performance is the aperture illumination efficiency which is defined as the ratio $e_{ap} = \mathcal{D}/\mathcal{D}_{max}$, where $\mathcal{D}_{max}$ is calculated by

$$\mathcal{D}_{max} = \frac{4\pi A}{\lambda^2} \tag{3.7}$$

Table 3.2:
Multi-Layered Flat Metamaterial Lens Performance Statistics. Simulated and measured
results agree well for both E- and H-plane.

	Simulated	Measured
Directivity (dBi)	22.73 dBi	23.06 dBi
E-Plane Half-Power Beamwidth	12.9°	13.8°
H-Plane Half-Power Beamwidth	12.0°	12.2°
E-Plane Sidelobe Level	−22.6 dB	−20.5 dB
H-Plane Sidelobe Level	−20.5 dB	−18.5 dB
Cross-Pol Level E-plane	−35 dB	−24 dB
Cross-Pol Level H-plane	−30 dB	−24 dB

where A is the physical area of the lens and λ is the wavelength at the frequency of operation. The results indicate that the proposed lens has a 76% simulated and 82% measured aperture illumination efficiency. The radiation efficiency is defined as $e_{rad} = G/\mathcal{D}$, where G is the gain of the antenna, and the overall antenna efficiency could be determined from $e_{tot} = e_{rad} \times e_{apt} = G\lambda^2/(4\pi A)$. The radiation efficiency includes the efficiency that accounts for losses from the dielectric layers (e_d), copper cladding (e_{cop}), radiation losses from the patch array feed (e_{feed}), and mismatch ($e_{\text{match}} = (1 - |S_{11}|^2)$). Table 3.3 shows the simulated values for the efficiencies of the proposed lens antenna at $f = 13.4$ GHz. The simulated overall antenna efficiency is 72.2% which corresponds to a 22.51 dBi gain. The gain was measured using the gain transfer method and a standard gain horn antenna [99]. The measured gain is 22.2 dBi, the measured overall antenna efficiency is 67.3% and the measured −3 dB gain bandwidth is 4.7%.

To further assess the bandwidth of the antenna, table 3.4 shows the simulated directivities for different frequencies of 5% increments with respect to the center frequency. The ideal feed described by (3.2) is used and we are only concerned about the bandwidth of the lens itself. The $\cos^q \theta$ type of feed provides the same radiation pattern for all frequencies and the overall bandwidth is determined by the lens. The simulated −1 dB directivity bandwidth is 40% (from 12.7 GHz to 16.8 GHz). Note that simulation results show that the lens itself is a

Table 3.3:
Detailed simulated efficiencies of the proposed lens antenna of Fig. 3.13(a) at $f = 13.4$ GHz.

Efficiency	Value (%)
mismatch e_{match}	99.0%
feed radiation e_{feed}	98.7%
dielectric loss e_d	97.6%
copper loss e_{cop}	99.8%
aperture illumination e_{ap}	75.9%
overall e_{tot}	72.2%

Table 3.4:
Simulated directivities of the proposed lens for different operating frequencies across the bandwidth. An ideal feed is used and we are only concerned about the bandwidth of the lens itself and not the overall bandwidth including the feed.

f	$\frac{f-13.4GHz}{13.4GHz}\%$	Directivity (dBi)
12.1 GHz	-10%	22.3 dBi
12.7 GHz	-5%	22.7 dBi
13.4 GHz	0%	23.0 dBi
14.1 GHz	5%	23.3 dBi
14.7 GHz	10%	22.9 dBi
15.4 GHz	15%	23.2 dBi
16.1 GHz	20%	23.1 dBi
16.8 GHz	25%	23.0 dBi
17.4 GHz	30%	22.0 dBi

broadband design assuming an ideal feed that could provide stable radiation pattern for all frequencies. The measured gain bandwidth is limited by the patch array feed that was used in this chapter. The resonant patch array feed is narrowband (see Fig. 3.12) and the gain bandwidth of the lens antenna is limited by the S_{11} bandwidth of the feed and not by the lens.

Table 3.5 shows a comparison of our proposed lens antenna with other designs published in the literature in terms of peak measured aperture illumination efficiency e_{ap} and thickness-diameter ratio. In [108], eight layers of frequency selective surfaces were stacked with seven layers of bonding materials to form a non-collapsible lens, and a thin metasurface lens with a single panel was used in [29]. [116] presents the design of a transmitarray which was mounted

Table 3.5:
Comparison of our proposed design with previous works.

	Proposed lens	[108]	[29]	[116]	[111]
Measured aperture illumination efficiency e_{ap}	82%	26%	60%	59%	48%
Thickness-Diameter ratio	0.18, 0.04 when collapsed	0.12	0.02	0.18	0.50
Aperture area (λ_0^2)	19.6	38.9	34.2	58.5	8

at the aperture of a conical horn to produce a more directive radiation pattern than that of the standard conical horn antenna. A non-flat half Maxwell fish-eye was implemented in [111] by gradient refractive index metamaterials. As shown in Table 3.5, the proposed collapsible flat-layered metamaterial lens antenna outperforms the previous designs in terms of aperture illumination efficiency e_{ap}, while maintaining minimal thickness-diameter ratio when collapsed, which results in low packaging height.

3.4 Summary

This chapter presented the design, prototyping and measurement results of multi-layered meta-lenses. A numerical synthesis algorithm based on GO and PSO was revisited and applied to synthesize both on-axis and off-axis fed meta-lenses. It was shown that the lens designs based on the numerical synthesis algorithm outperform the designs that were produced using previous synthesis methods that are based on the straight path approximation. This chapter also introduced the concept of collapsible flat-layered meta-lens antenna based on gradient-refractive-index metamaterials. The attractiveness of this new lens is its low packaging height, weight, while maintaining high performance. The proposed lens antenna consists of multi-layer double-sided square-ring units of variable sizes distributed on planar dielectric substrates to satisfy the required refractive index distribution. Experimental and simulation results showed good agreement. Owing to the air gap between adjacent dielectric

layers, the lens can be stored compressed in a stacked configuration with minimal height. This gives rise to a design that can collapse, thus occupying five times less height compared to the deployed state. A proof of concept prototype operating at 13.4 GHz was fabricated and measured in the UCLA Plane Bi-Polar Near Field measurement range.

CHAPTER 4

Low-Profile Transmitarray Antenna for Conical Beam Scanning: Concept, Optimization, and Measurements

4.1 Transmitarrays Antennas for Conical Beam Scanning

Of the few design choices available in the literature, spherical Luneburg lenses, shaped 3D-printed lenses, and flat-layered meta-lenses have been proposed to create the conical beam scanning, as discussed in chapters 2 and 3. A more lightweight design with reduced thickness than the previous lenses that can achieve the conical beam sweep is desirable. In this chapter, we propose transmitarrays as a low-profile antenna alternative that can produce the conical beam scanning, as shown in Fig. 4.1(b).

Transmitarray antennas have attracted considerable attention as collimating devices in a variety of antenna systems in microwave and millimeter-wave frequencies because of their high gain and low profile [123]. Transmitarrays typically consist of an arrangement of unit cells on a flat transmissive surface placed at a distance from the antenna feed. Each unit cell is designed to provide a phase shift to the incident wave so that the phase of the exit aperture field has the intended phase gradient for the desired beam peak angle [124]. Thus, the transmitarray acts as a mask that converts the incident spherical wavefront from the antenna feed to a planar wavefront. A schematic showing a conventional transmitarray that is fed on axis and generates the broadside beam is shown in Fig. 4.1(a).

Various studies and experiments have reported the design of transmitarrays. For example, transmitarrays with the main beam direction at the boresight and at non-zero scan angles were presented in a series of recent works [31, 32, 125–130]. The common characteristic of the
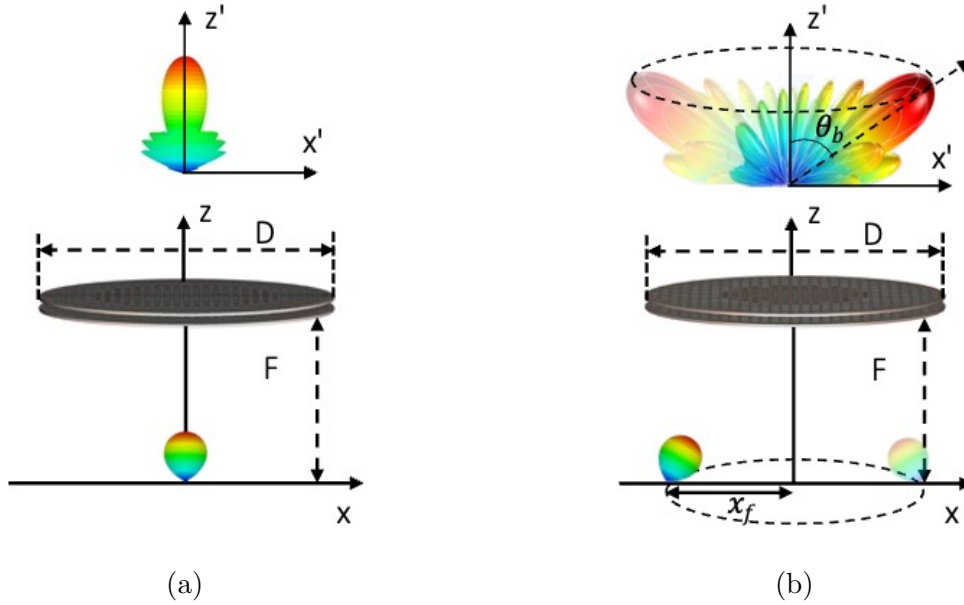
Figure 4.1 Transmitarray evolution: (a) Conventional transmitarray that is fed on axis and generates the broadside beam. (b) Proposed transmitarray that is fed off axis and produces the conical beam scanning.

previously reported transmitarrays is that they are designed to focus the beam at a single direction when the feed is placed at a specific location; therefore, the off-axis performance when the feed is placed at various locations along the transmitarray focal ring is degraded. Note that the off-axis performance of antennas that can produce the conical scan through successive excitation of feeds placed along the body of revolution ring focus is desirable for real-life application necessitating scanning in a conical sweep [21, 95, 131]. Some potential applications requiring conical beam scanning are shown in Fig. 4.2 and include spaceborne wind scatterometers that take multiple (at least four) measurements along an azimuthal conical scan to retrieve the wind speed and direction [21, 33–35]; geosynchronous satellite-based navigation and guidance systems that serve moving vehicles, where the antenna is mounted on the mobile vehicle and has a pencil-beam pattern that sweeps out a cone in space to continuously communicate with the satellite [45–47]; spaceborne microwave radars [36–38] as well as millimeter wave imaging systems [39–44].

The key contributions of this chapter are: (a) Transmitarray antennas are proposed as an antenna alternative that can potentially achieve the conical beam sweep for the first time.

(a)   (b)
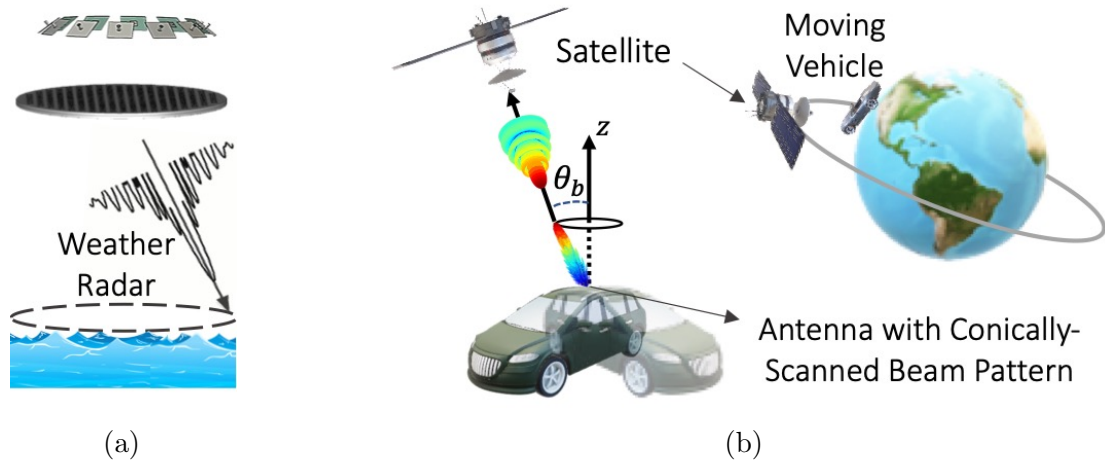
Figure 4.2 Potential applications requiring conical beam scanning: (a) Spaceborne wind scatterometer weather radars. (b) Geosynchronous satellite-based navigation and guidance systems that serve moving vehicles.

(b) Unlike conventional transmitarrays that are designed for single feed location and beam direction, the synthesis of transmitarrays for conical beam scanning is a challenging problem. Therefore, a novel synthesis algorithm is presented based on the optimization of the feed location and a modified transmitarray phase compensation. (c) The thickness and therefore the weight of the previously reported lenses that were proposed for conical beam scanning scales with the lens diameter (see, for example, chapters 2 and 3 and the references therein). Contrary to the previously reported lenses, the thickness of the proposed transmitarray does not scale with the transmitarray diameter. Therefore, the transmitarray is low-profile, more lightweight and has reduced thickness when compared to the lens of the same diameter. The transmitarray consists of only two pairs of stacked printed circuit boards (PCBs) separated by an air gap.

4.2 Transmitarray Design Overview

4.2.1 Unit Cell Element

The transmitarray unit cell that is employed in this chapter is shown in Fig. 4.3. The unit cell was first introduced in [31] and is used here because: (a) A spaceborne application of

particular interest requiring conical beam scanning is the weather scatterometer radars that measure the ocean wind [21]. The most recent Ku-Band scatterometers operate at 13.4 GHz. Inspired by the real-life application, we choose f=13.4 GHz as the operating frequency throughout this chapter. The original unit cell presented in [31] was designed to operate at 13.5 GHz, and therefore choosing this unit cell eliminates the need for the development of a new unit cell operating at the required frequency band. (b) The transmitarray comprising the unit cell of Fig. 4.3 maintains a reduced profile of 0.8 cm ($0.36\lambda_0$, where λ_0 is the free-space wavelength), while achieving a wideband operation with a measured 1-dB bandwidth of 13.1% as discussed in section 4.5. Note that other transmitarrays that achieve similar gain bandwidth have higher profiles. For example, the transmitarray presented in [125] has a thickness of $0.76\lambda_0$ with a 11.7% 1 dB gain bandwidth, and the transmitarray presented in [132] has a thickness of $0.65\lambda_0$ with a 15% 1 dB gain bandwidth.

Fig. 4.3(a)-(b) shows the configuration and dimensions of the unit cell, where two pairs of stacked PCBs are separated by an air gap. Each PCB pair consists of two square patches and one square loop with four microstrips printed on two RO4003C dielectric substrates with permittivity $\epsilon_r = 3.55$ and dielectric loss tangent $\tan\delta = 0.0027$. The phase shift of the unit cell is achieved by simultaneously varying the square size W_1 of the patches printed on the first and third layers. The unit cell of the periodic structure was modeled in CST Microwave Studio full-wave simulation software. We used the frequency domain solver that is based on the finite element method (FEM). Periodic boundary conditions are imposed on the right, left, front, and rear sides and the structure is excited by a linear transverse electric electromagnetic wave propagating in z-direction, which is modeled using the fundamental Floquet mode, as discussed in [25, 31]. Fig. 4.3(c) shows the simulated phase and amplitude of the transmission coefficient S_{21} under normal plane wave incidence as W_1 varies. When W_1 changes from 1.7 to 5 mm, a 360°phase shift is obtained while the transmission amplitude is better than the typical requirement of -3 dB [123]. A thorough description of the unit cell with more details on the development, oblique incidence and bandwidth performance can be found in [31].
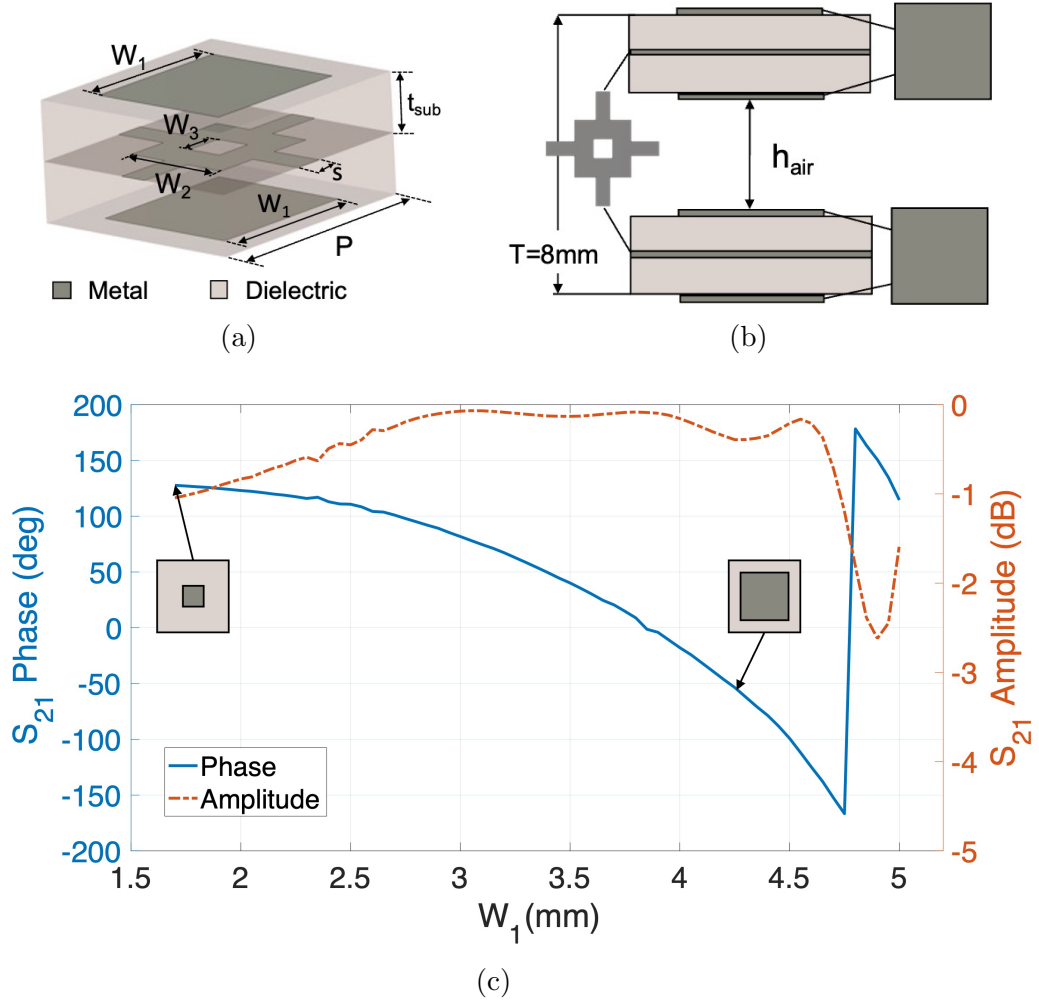
Figure 4.3 Transmitarray unit cell: (a) Perspective view and (b) Side view. $P = 6$ mm, $s = 0.75$ mm, $W_2 = 3$ mm, $W_3 = 1$ mm, $t_{\text{sub}} = 0.8$ mm, $h_{\text{air}} = 4.9$ mm. (c) S_{21} phase and amplitude with varied values of W_1 at 13.4 GHz.

4.2.2 Transmitarray Synthesis

The geometry of the synthesis problem under consideration is shown in Fig. 4.4. A transmitarray is illuminated by a feed that is located at $(-x_f, 0, -F)$ and tilted at an angle $\theta_f = \tan^{-1}(x_f/F)$ with respect to z axis to point at the transmitarray center to reduce spillover loss. The feed is assumed to radiate a spherical wavefront. The transmitarray diameter is D and the vertical distance of the feed from the transmitarray center is F. The intended beam peak is denoted by (θ_b, ϕ_b). The transmitarray aperture is discretized into rectangular grids each occupying an area of P^2, where $P = 6$ mm is the size of the
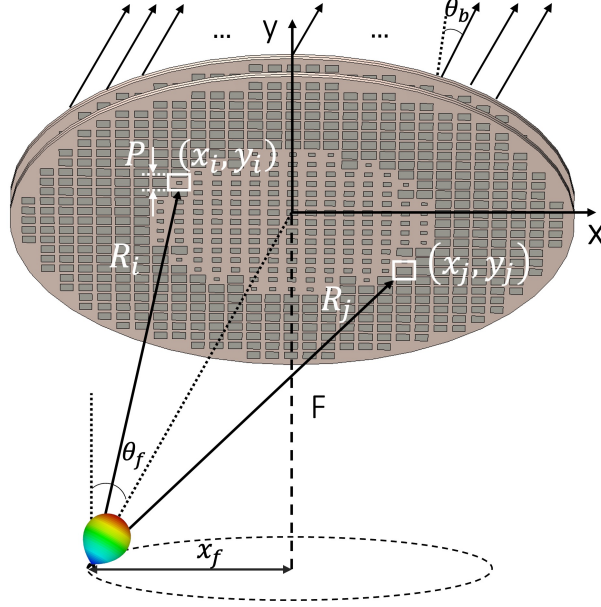
Figure 4.4 Transmitarray geometry for the calculation of the required transmitarray phase compensation.

transmitarray unit cell of section 4.2.1. The transmitarray phase compensation to generate the intended beam is accomplished by varying the transmission phase of each transmitarray element ϕ_i according to the element position (x_i, y_i) in the array as follows [131, 133]:

$$\Delta\Phi_i(x_i, y_i) = k_0(R_i - x_i \sin\theta_b \cos\phi_b - y_i \sin\theta_b \sin\phi_b) \tag{4.1}$$

where λ_0 is the free-space wavelength, $k_0 = 2\pi/\lambda_0$ is the free-space wavenumber, and $R_i = \sqrt{(x_i - x_f)^2 + y_i^2 + F^2}$ is the distance from the feed to the center of the ith transmitarray element.

In what follows, the transmitarray diameter is $D = 18$ cm, the focal length is $F = 13$ cm (resulting in a F/D ratio of 0.7, which within the typical range of 0.5-1 [134] and the same as in [131, 135]), the operating frequency is $f = 13.4$ GHz (the free-space wavelength is $\lambda_0 = 2.24cm$). The feed is a Narda 639 Ku-band standard gain horn antenna [136]. Note that other feeds could also be considered.

4.3   The Necessity for New Synthesis Algorithm

4.3.1   18 cm On-Axis Transmitarray Design

An on-axis fed transmitarray with a diameter of $D = 18$ cm and $F = 13$ cm at $f = 13.4$ GHz is considered. The feed is placed on axis ($x_f = 0$) and the intended beam peak is $\theta_b = 0°$. The transmitarray phase compensation is synthesized based on (4.1). The target aperture phase is the superposition of the feed phase at the aperture and the transmitarray phase compensation, as shown in Fig. 4.5. The transmitarray acts as a mask to compensate the differential spatial delay of the spherical wave ray emitted from the antenna feed and provide uniform aperture phase for broadside beam. For each location at the aperture, the dimension W_1 of the unit cell of section 4.2.1 is tuned based on Fig. 4.3(c) to provide the required phase shift that is equal to the required transmitarray phase compensation. The final on-axis fed transmitarray design is shown in Fig. 4.5(d).

The performance of the transmitarray design that is designed for on-axis feed is assessed through full-wave simulations. We used the transient solver of CST that is based on the finite integration technique and hexahedral mesh. It is worthwhile mentioning that the simulation of the transmitarray is computationally intensive. The computer used for our CST simulations has a 64-bit operating system and 256 GB RAM. A single simulation was completed in about 17 h and required 75.1 GB of memory. The feed is placed on axis, and this particular case will be referred to as OnAxisDes-OnAxisFed as the transmitarray is designed for on-axis feed and is fed on axis. The transmitarray demonstrates a directional far-field pattern at f=13.4 GHz, as shown in Fig. 4.6(a). The simulated performance statistics of the OnAxisDes-OnAxisFed transmitarray are shown in table 4.1. The simulated directivity and gain are 24.9 dBi and 24.7 dBi, respectively, corresponding to an aperture illumination efficiency e_{ap} (as defined in [25,97]) of 48.4% and an aperture efficiency of 46.1%. The half-power beamwidth (HPBW) for H- and E-planes are 8.5°and 9.1°, the sidelobe level (SLL) for H- and E-planes are -22.0 dB and -20.3 dB, respectively, and the beam peak is at $\theta_b = 0°$. Note that in previous work, transmitarrays designed for on-axis feed and broadside beam have similar aperture efficiency values. For example, the OnAxisDes-OnAxisFed simulated aperture efficiency of 46.1% is
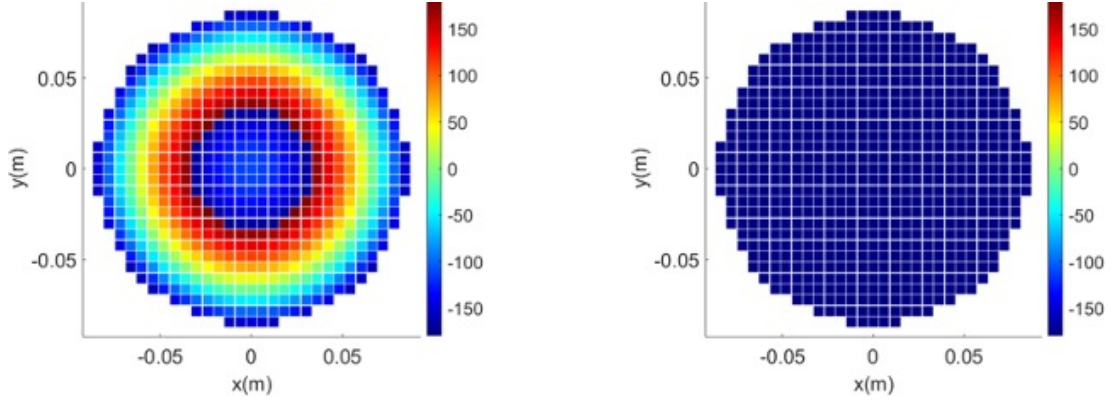
(a) Feed Phase at Aperture.

(b) Target Aperture Phase.
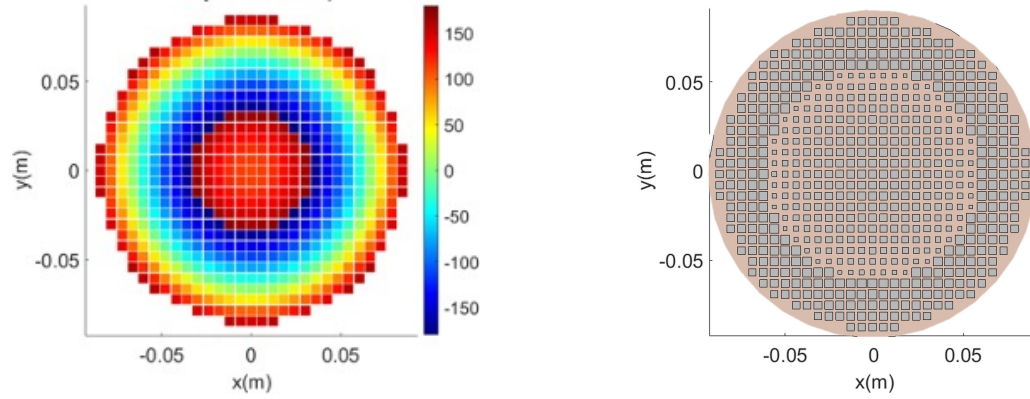
(c) Transmitarray Phase Compensation.

(d) Transmitarray Model.

Figure 4.5 Transmitarray that is designed for on-axis feed.

close to the previously reported values of 47% in [125] and 50.9% in [32].

In general, the phase compensation of a transmitarray that is designed for on-axis feed and broadside beam is circularly symmetric. In particular, for $x_f = 0$ and $\theta_b = 0$, (4.1) reduces to:

$$\Delta\Phi_i(x_i, y_i) = k_0 R_i = k_0\sqrt{\rho_i^2 + F^2} \tag{4.2}$$

where (x_i, y_i) is the center of the ith element position at the transmitarray aperture; $\rho_i = \sqrt{x_i^2 + y_i^2}$ and ϕ_i are the radial and azimuthal coordinates of the ith transmitarray element in the cylindrical coordinate system. (4.2) is ρ_i-dependent and ϕ_i-independent resulting in a transmitarray with circular symmetry, as shown in Fig. 4.5(c)-(d). A design with circular symmetry is desirable for conical beam scanning applications because it can potentially take advantage of the azimuthal symmetry of the feeds placed along the ring focus that
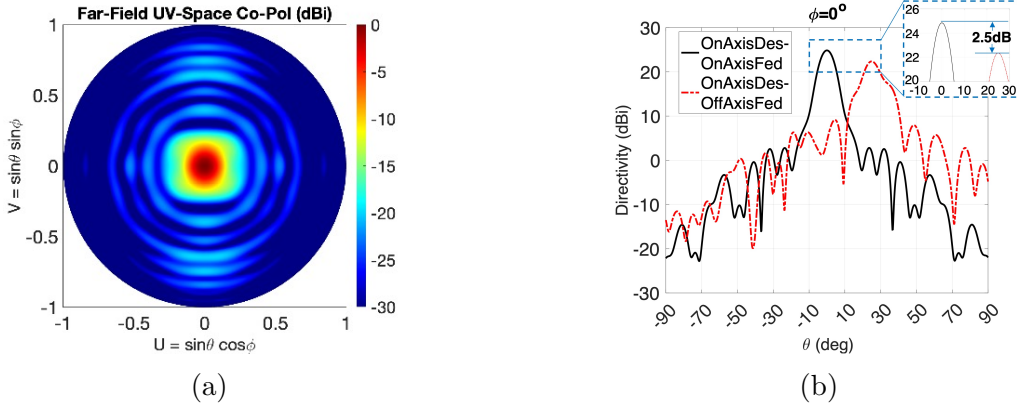
Figure 4.6 Simulation results of the 18 cm transmitarray that is designed for on-axis feed (f=13.4 GHz): (a) Simulated far-field normalized radiation pattern of the OnAxisDes-OnAxisFed transmitarray. (b) Simulated directivities of the OnAxisDes-OnAxisFed and OnAxisDes-OffAxisFed transmitarrays for the H-plane.

Table 4.1:
18 cm transmitarray simulated performance statistics (f=13.4 GHz).

	OnAxisDes-OnAxisFed	OnAxisDes-OffAxisFed	OffAxisDes-OffAxisFed-Pos.1	OffAxisDes-OffAxisFed-Pos.3	Optimized Pos.1-4
Directivity (dBi)	24.9 dBi	22.4 dBi	24.2 dBi	20.7 dBi	24.1 dBi
HPBW H-plane	8.5°	9.9°	8.2°	13.7°	8.3°
SLL E-plane	-22.0 dB	-13.0 dB	-13.1 dB	-6.7 dBi	-11.4 dBi
$|\theta_b|$	0°	25.0°	25.0°	44.2°	44.2°
e_{ap}	48.4%	27.2%	41.2%	18.4%	40.3%

will ultimately produce the conical beam sweep. Therefore, the circularly-symmetric design of Fig. 4.5(c)-(d) that is designed for on-axis feed and broadside beam can be a potential solution to conically-scan the beam. To assess the conical scanning capability of the design of Fig. 4.5(c)-(d), the OnAxisDes-OnAxisFed transmitarray is now fed off axis and we set $x_f = 6.9$ cm[1]. The latter design is denoted by OnAxisDes-OffAxisFed hereafter. The simulated H-plane radiation pattern and performance statistics are shown in Fig. 4.6(b) and table 4.1. The directivity drops by 2.5 dB to 22.4 dBi, e_{ap} reduces to 27.2% from 48.4%, the

---

[1]We choose $x_f = 6.9$ cm to be the same as the optimized feed location of the transmitarray that is presented in section 4.4. This allows fair comparison between the simulated performance statistics of the OnAxisDes-OffAxisFed and the Optimized transmitarray, as shown in table 4.1.

H-plane beamwidths broaden to 12.3° from 9.9°, the H-plane sidelobe level has risen to -13.0 dB from -22.0 dB compared to the OnAxisDes-OnAxisFed transmitarray. It can be observed that the transmitarray that was designed for particular geometrical parameters (i.e on-axis feed and beam beak at $\theta_b = 0°$) performs best only for these parameters. When the feed is placed at an arbitrary position $(-x_f, 0, 0)$, the off-axis performance required for conical beam scanning is noticeably degraded.

4.3.2 18 cm Off-Axis Transmitarray Design

In an attempt to achieve a better off-axis performance compared to the OnAxisDes-OffAxisFed design, an off-axis fed 18 cm transmitarray is designed based on the synthesis methodology that was described in section 4.2.2 and (4.1). The latter design is denoted by OffAxisDes-OffAxisFed. The feed is placed off axis at $x_f = 10$ cm for approximately -8 dB edge taper. For scatterometer applications, the beam peak has to be greater than 20° to allow the unambiguous retrieval of the wind speed and direction (see references [33, 34]) and, therefore, we choose $(\theta_b = 25°, \phi_b = 0°)$ as an example. The target aperture phase, the feed phase at the aperture, the transmitarray phase compensation, and the top view of the OffAxisDes-OffAxisFed transmitarray are shown in Fig. 4.7.

Fig. 4.8 shows five distinct feed positions $(-x_f, 0, 0)$, $(0, x_f, 0)$, $(x_f, 0, 0)$, $(0, -x_f, 0)$, and $(-x_f\sqrt{2}/2, x_f\sqrt{2}/2, 0)$ (Positions 1-5), where the feeds are placed along the body of revolution ring focus of the transmitarray. The OffAxisDes-OffAxisFed transmitarray is simulated in CST for the feed placed at positions 1-4. The simulated far-field patterns are shown in Fig. 4.9. When the feed is placed at position 1, the OffAxisDes-OffAxisFed transmitarray achieves higher directivity and narrower beamwidth when compared to the OnAxisDes-OffAxisFed design. In particular, the H-plane half-power beamwidth is 8.2°, the H-plane sidelobe level is -13.1 dB, and the beam peak is at $\theta_b = 25°$. The simulated directivity is 24.2 dBi, corresponding to an e_{ap} of 41.2%. Note that the scan loss for this beam angle is 0.43 dB and that the OffAxisOpt-OffAxisFed transmitarray directivity is 0.7 dB lower than the OnAxisDes-OnAxisFed case and 1.8 dB higher than the OnAxisDes-OffAxisFed
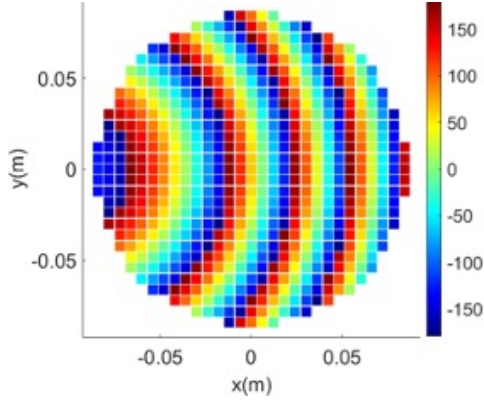
(a) Feed Phase at Aperture.
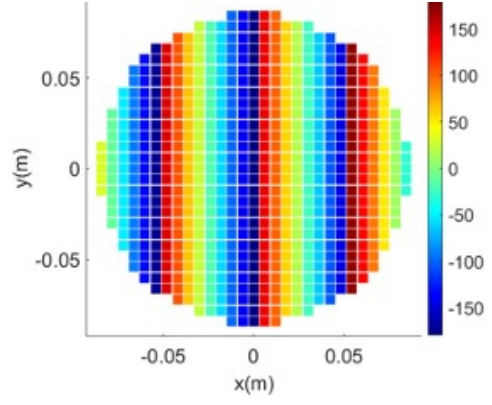
(b) Target Aperture Phase.
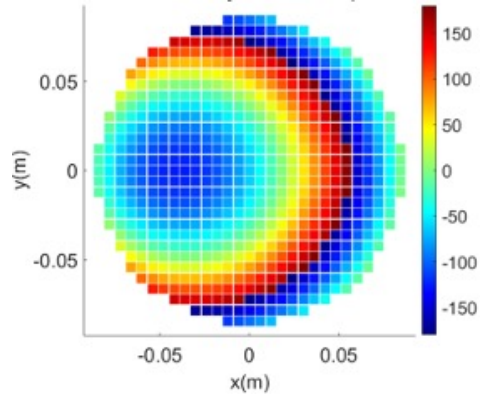
(c) Transmitarray Phase Compensation.
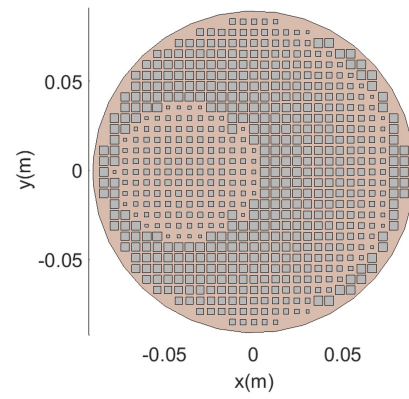
(d) Transmitarray Model.

Figure 4.7 Transmitarray that is designed for off-axis feed.

case. Also, note that the OffAxisDes-OffAxisFed transmitarray is not circularly-symmetric as was the OnAxisDes-OffAxisFed design. Consequently, the performance is degraded and the beam peak shifts from the intended value of 25°when the feed is placed at positions 2-4, as shown in Fig. 4.9. The simulated performance statistics of the OffAxisDes-OffAxisFed transmitarray when the feed is placed at position 3 are shown in table 4.1. The beam peak shifts from 25° to 44.2°, the sidelobe level rises from -13.1 dB to -6.7 dB, the beamwidth broadens from 8.2°to 13.7°, and the directivity drops by 3.5 dB from 24.2 dBi to 20.7 dB corresponding to $e_{\mathrm{ap}} = 18.4\%$.
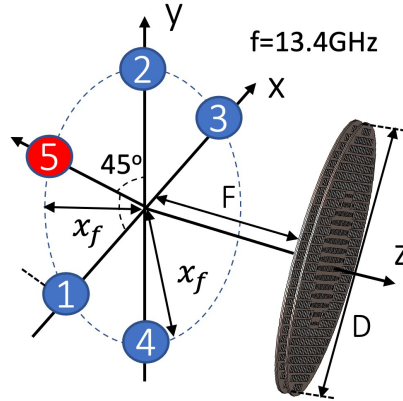
Figure 4.8 Five distinct feed positions $(-x_f, 0, 0)$, $(0, x_f, 0)$, $(x_f, 0, 0)$, $(0, -x_f, 0)$, and $(-x_f \sqrt{2}/2,\ x_f \sqrt{2}/2, 0)$ (Positions 1-5). The feeds are placed along the body of revolution ring focus of the transmitarray.

4.4 Transmitarray for Conical Beam Scanning: Novel Synthesis Algorithm

As discussed in section 4.3, a transmitarray designed to produce the conical beam scanning is desired to:

(a) Maintain circular symmetry. This is required to achieve the scan in a conical sweep through successive excitation of feeds placed along the body of revolution ring focus, as shown in Fig. 4.8.

(b) Maximize the achieved directivity when the feed is placed off-axis. This is desirable for applications requiring off-axis fed designs producing highly-directive beams [21].

The design presented in section 4.3.1 satisfies (a) but not (b), whereas the design presented in 4.3.2 satisfies (b) but not (a). In this section, we present a novel methodology for the synthesis of a transmitarray that satisfies both (a) and (b) and can achieve the conical beam scanning.

As discussed in section 4.3.2 and illustrated in Fig. 4.7, the transmitarray phase compensation does not maintain circular symmetry for an arbitrary feed location x_f and intended

74

Figure 4.9 Simulated normalized radiation patterns of the co-pol of the OffAxisDes-OffAxisFed transmitarray with feed at positions 1-4.

beam peak angle θ_b. To illustrate this, the target aperture phase, the feed phase at the aperture, and the transmitarray phase compensation for the same intended beam peak $(\theta_b = 25°, \phi_b = 0°)$ and various feed locations $(x_f = 0, x_f = -3 \text{ cm, and } x_f = -6.9 \text{ cm})$ are shown in Fig. 4.10. The first column illustrating the target aperture phase is the same for all cases to ensure that the phase of the aperture field has the intended phase gradient for the desired beam scan angle. The second column, i.e. the feed phase at the aperture, is the $-k_0 R_i$ term in (4.1). It is equal to the differential spatial delay of the spherical wave ray emitted from the antenna feed and it depends on the feed position. The third column, i.e. the transmitarray phase compensation, is obtained using (4.1). The goal is to synthesize a modified transmitarray phase compensation $\Delta\phi_m(\rho_i)$ that is ϕ_i-independent to satisfy (a) and is close to the transmitarray phase compensation obtained by (4.1) to satisfy (b).

To synthesize $\Delta\phi_m(\rho_i)$, we take the center of each pixel (x_i, y_i) in the transmitarray aperture and calculate its radial coordinate $\rho_i = \sqrt{x_i^2 + y_i^2}$ as well as the value of the transmitarray phase compensation $\Delta\phi(\rho_i)$ based on (4.1). Note that there are 641 total pixels based on the transmitarray and unit cell dimensions that are used in this chapter. The
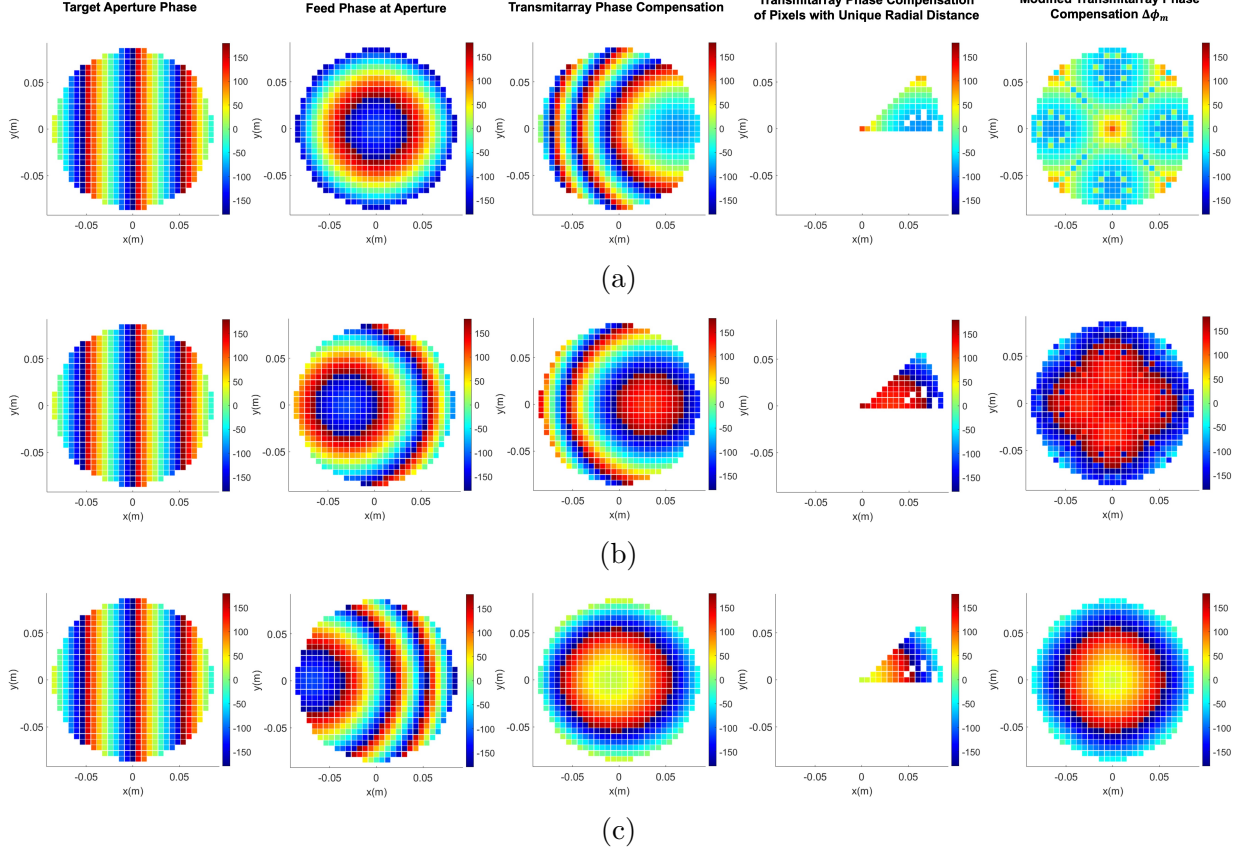
Figure 4.10 18 cm transmitarray analysis for the intended beam peak ($\theta_b = 25°, \phi_b = 0°$) (f=13.4 GHz). The target aperture phase; the feed phase at the aperture; the transmitarray phase compensation obtained using (4.1); the transmitarray phase compensation of pixels with unique radial distance; the modified ϕ_i-independent transmitarray phase compensation based on $\Delta\phi_m(\rho_i)$ for various feed positions: (a) $x_f = 0$, (b) $x_f = -3$ cm, and (c) $x_f = -6.9$ cm.

points in the grid with the same ρ_i are omitted to allow the definition of a unique functional mapping $\Delta\phi_m : \mathbb{A}_u \rightarrow \mathbb{B}_u$, with the domain $\mathbb{A}_u = \{\rho_{i_u}\}$ and range $\mathbb{B}_u = \{\Delta\phi(\rho_{i_u})\}$, where $i_u = 1, 2, \ldots$ indicates the i_u^{th} transmitarray pixel with unique radial distance. There are 77 pixels corresponding to unique radial distance ρ_{i_u} in $\mathbb{A}_u$, as shown in the fourth column of Fig. 4.10. Note that these pixels cannot occupy more than an octant of the transmitarray. This is because the transmitarray aperture is eight-way symmetric, and the center of at least one pixel at the first octant has the same radial coordinate with at least one pixel at each one of the other seven octants [137].

Once the modified transmitarray phase compensation $\Delta\phi_m(\rho_i)$ is defined, i.e. there is a unique mapping of the radial distance of the transmitarray pixel position to the value of the transmitarray phase compensation, the entire transmitarray aperture phase shift for each pixel can be calculated using $\Delta\phi_m(\rho_i)$, as shown in the final column of Fig. 4.10. The standard deviation of the phase difference between the transmitarray phase compensation calculated by (4.1) and the modified version shown in the fifth column of Fig. 4.10 is a metric indicating the resemblance of the third and fifth column. For example, the standard deviation of the phase error for $x_f = 0$ (Fig. 4.10(a)), and $x_f = -6.9$ cm (Fig. 4.10(c)) are 90.2° and 22.4°, respectively.

The goal is to find the feed location x_f such that the modified transmitarray phase compensation and the transmitarray phase compensation calculated by (4.1) have the minimum standard deviation of the phase difference. For this purpose, the transmitarray analysis tool to calculate the standard deviation of the phase difference is linked with PSO to obtain the best design [93]. A high-level flowchart of the novel synthesis algorithm is shown in Fig. 4.11. The feed position is allowed to vary within the $[-D/2, 0]$ range, and the feed at each location is tilted towards the center to reduce spillover loss. The fitness function is chosen to be the standard deviation of the phase difference between the modified transmitarray phase compensation and the transmitarray phase compensation calculated by (4.1). The optimization of 4 particles in total (4 per unknown) and invisible boundaries is run for 50 iterations with randomly chosen start points for the single optimization variable. The PSO convergence plot for the obtained optimized transmitarray off-axis fed design is shown in Fig. 4.12. The final optimized feed position $x_f = 6.9$ cm corresponding to a fitness function of 22.4° was found after only 13 iterations and the optimized modified transmitarray phase compensation that is circularly-symmetric is shown in Fig. 4.10.
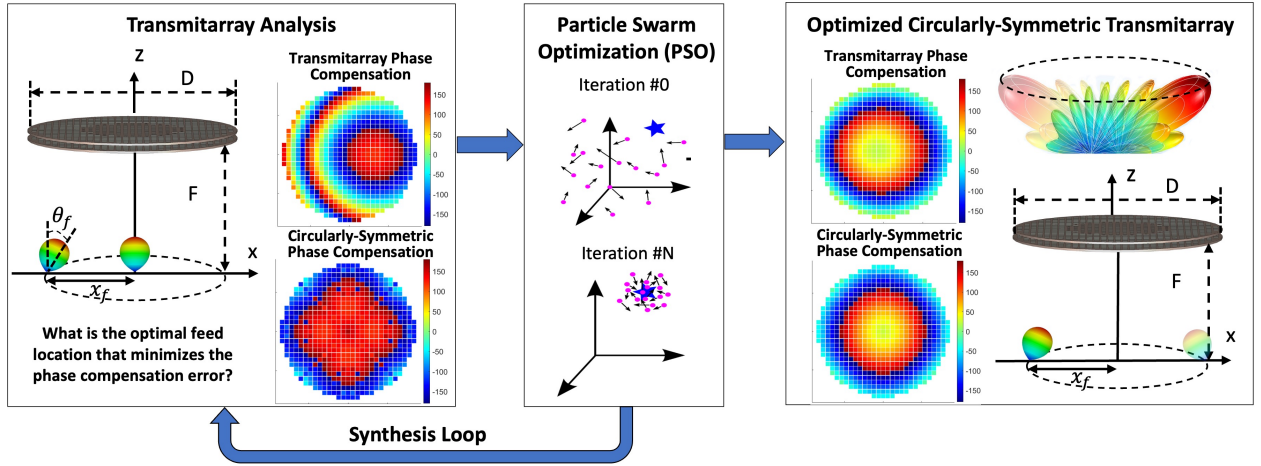
Figure 4.11 High-level flowchart of the transmitarray synthesis algorithm. The transmitarray analysis tool to calculate standard deviation of the phase difference between the transmitarray phase compensation calculated by (4.1) and the modified transmitarray phase compensation $\Delta\phi_m$ is linked with PSO to obtain the best transmitarray design.

4.5   Transmitarray Prototyping, Simulation, and Measurement Validation

The optimized transmitarray was fabricated using a standard PCB manufacturing process. The copper patterns were produced by means of wet etching where the unwanted copper is dissolved when immersed in a chemical solution. Two pairs of stacked 0.8 mm-thick Rogers RO4003C copper-coated substrates are separated by an air gap based on the unit cell configuration of section 4.2.1 and Fig. 4.3. Nylon spacers, each 4.9 mm thick, are positioned near the edge area so as to limit their electromagnetic interference and maintain the required inter-layer spacing. The top view, side view, and a close-up view of some representative unit cells of the transmitarray prototype are shown in Fig. 4.13(a). The transmitarray has a diameter of 18 cm, a total thickness of only 0.8 cm that does not scale with the diameter. The measured transmitarray weight is 0.171 kg, which is less than 20% of the weight (0.911 kg) of the 3D-printed lens of the same diameter that was presented in Chapter 2 for conical beam scanning, as shown in Fig. 4.14. The setup suitable for measurements with the Narda 639 Ku-band horn antenna as a feed and three posts rigidly supporting the transmitarray is shown in Fig. 4.13(b).
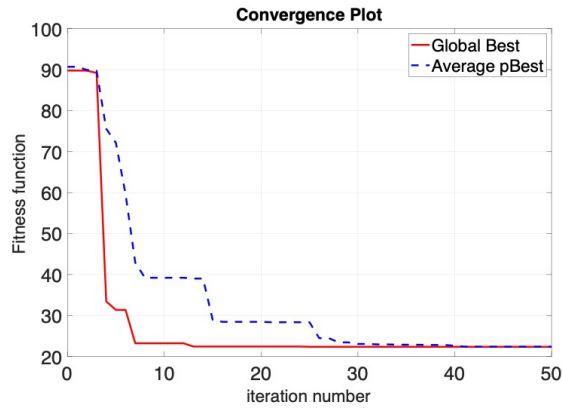
Figure 4.12 PSO convergence plot for the optimized off-axis fed transmitarray.

(a)   (b)
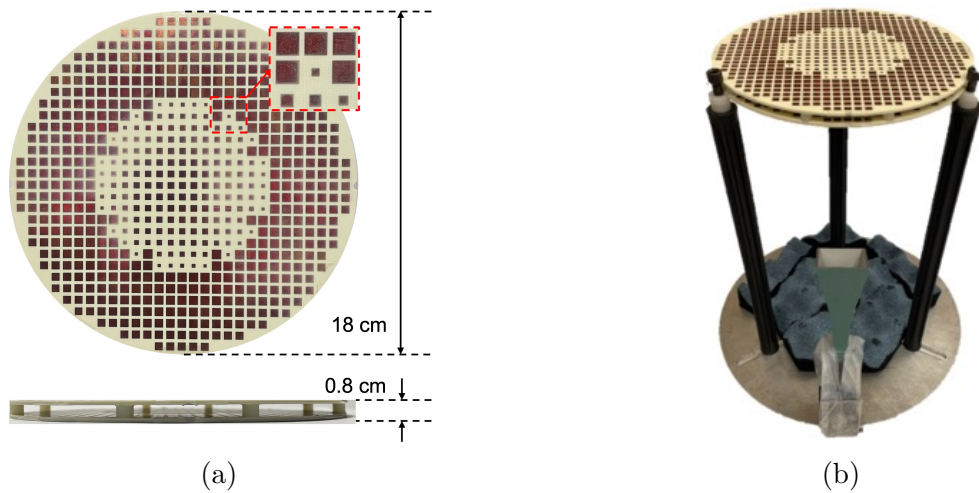
Figure 4.13 Fabricated transmitarray prototype: (a) Top view, side view, and zoom-in view of the 18 cm 3D-printed lens prototype. (b) Setup suitable for measurements with the Narda 639 Ku-band horn antenna as a feed.

To demonstrate the conical scanning capabilities of the optimized transmitarray, the transmitarray is simulated in CST when illuminated by the feed at five distinct positions along the focal ring with constant radius $x_f = 6.9$ cm, as shown in Fig. 4.8. Note that the full-wave simulation accounts for the effect of oblique incidence, anisotropy, and edge effects. The simulated directivity of 24.1 dBi is the same for positions 1-4 because of symmetry, and is only 0.1 dB lower for position 5. The simulated conically-scanned radiation patterns are shown in Fig. 4.15 and encouraged the measurement of the transmitarray for experimental validation.

The transmitarray was affixed at the UCLA spherical near-field chamber, as shown in Fig.

79

Figure 4.14 Weight Comparison of 18 cm 3D-printed lens that was presented in chapter 2 and the 18-cm transmitarray (both operate at 13.4 GHz). The measured weight of the transmitarray is 0.171 kg, which is less than 20% of the weight (0.911 kg) of the 3D-printed lens of the same diameter.

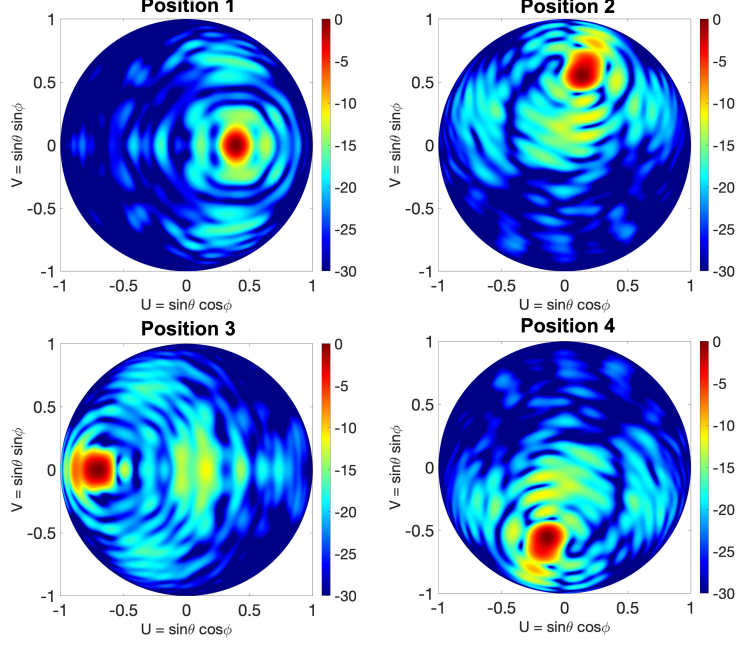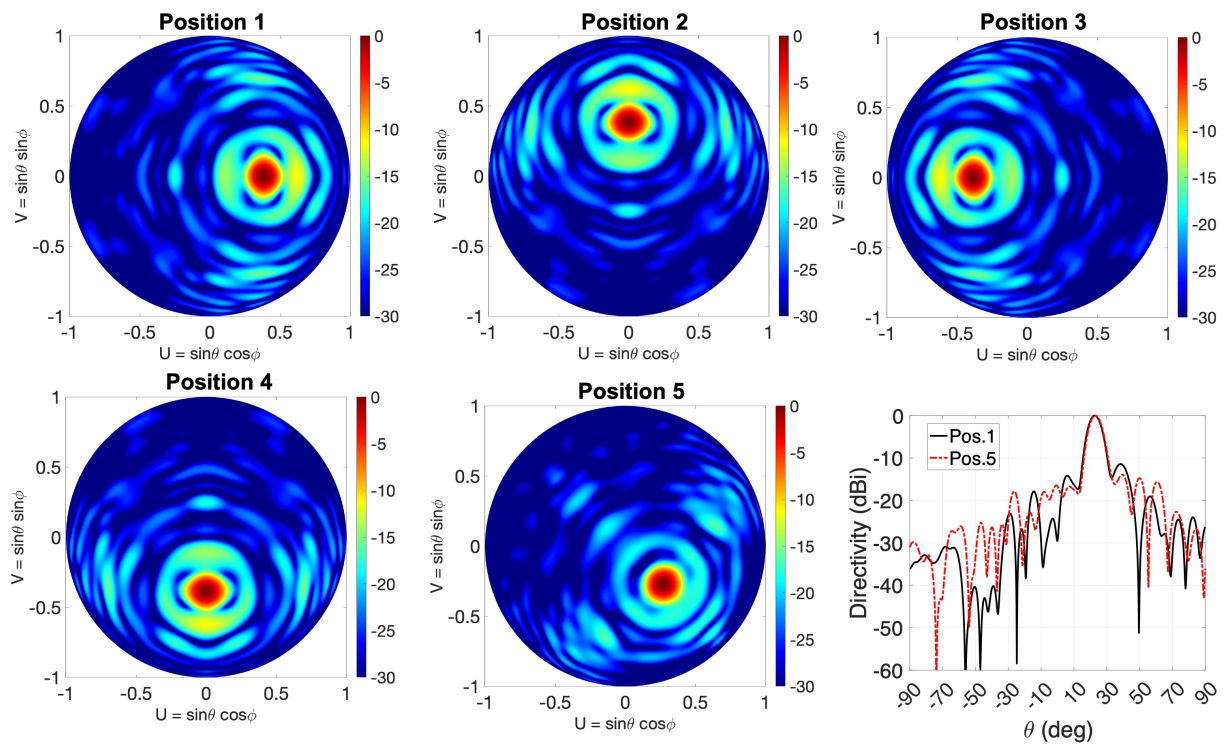

Figure 4.15 Simulated normalized radiation patterns of the co-pol of the optimized transmitarray with feed at position 1-5.

4.16(a). Three posts are used to support the transmitarray and the feed horn is placed at position 1. The transmitarray is modelled in CST and the simulated and measured radiation

patterns are shown in Fig. 4.16(b). The simulated and measured directivity is 24.1 dBi and 24.2 dBi, e_{ap} is 40.3% and 41.2%, the half-power beamwidth for the H-plane is 8.3°and 8.3°, the sidelobe level is -11.4 dB and -12.5 dB, and the beam peak angle is 25°and 24.9°. The gain was measured using the gain transfer method [99]. The measured gain is 23.6 dBi, corresponding to an aperture efficiency of 35.9%. The proposed transmitarray achieves an aperture efficiency that is within the typical range for scanned cases with scan angle between 20°and 30°. For example, the aperture efficiency of the transmitarray that was presented in [32] is 36.5% for a scan angle of 30°. Note that the design in [32] does not have the conical scanning capability due to the lack of circular symmetry.

To demonstrate the conical scanning capabilities of the transmitarray presented in this chapter, the feed was placed at positions 2-5. The measured results with the feed at positions 2-4 duplicate the results of the case when the feed is placed at position 1 within measurement uncertainty (the maximum directivity discrepancy is 0.1 dB) and have been averaged and placed into the second column of table 4.2. The radiation pattern when the feed is placed at position 5 is shown in as shown in Fig. 4.16(c). The measured directivity is 24.2 dBi, the half-power beamwidth is 8.5°, the sidelobe level is -12.8 dB, and the beam peak angle is 25.2°. Additionally, the horn at position 1 was rotated 90°along its local vertical axis to scan along the E-plane of the horn to study the effect of the feed polarization. The measured performance statistics of the measured transmitarray are shown in Fig. 4.2. The measurements agree well with predictions obtained by full-wave simulations. Discrepancies between the simulated and measured results are attributed to implementation tolerance caused by antenna assembly, misalignment and accuracy of measurements. The results show that the transmitarray can achieve the conical beam scanning by comparing the measurements taken at five locations within the ring focus. Note that the scanning capabilities could be achieved by several means including mechanically rotating the feed (see, for example, [138, 139]) or electronically scanning a feed array (as discussed in [21]).

The transmitarray was also measured at different frequencies across the bandwidth with the horn feed placed at position 1. The simulated and measured radiation patterns at four distinct frequencies (12.5 GHz, 13 GHz, 14 GHz, 14.5 GHz) around the center frequency of
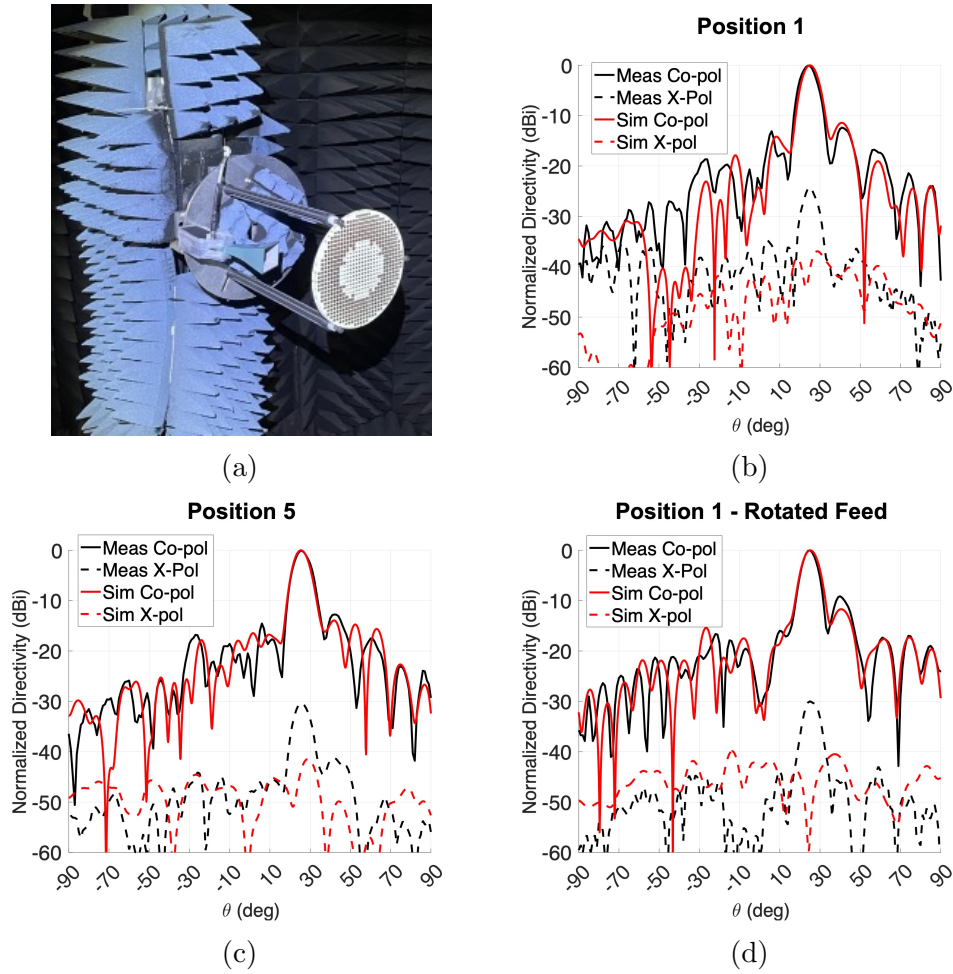
Figure 4.16 Transmitarray measured results (f=13.4 GHz): (a) Measurement setup at the UCLA spherical near-field chamber. Simulated and measured radiation patterns at 13.4 GHz with the feed horn (b) at position 1, (c) at position 5, (d) at position 1 and rotated 90°to scan the E-plane.

13.4 GHz are shown in Fig. 4.17. Overall, there is excellent agreement between simulation and measurements. The measured cross polarization for all cases presented in this chapter is below -25 dB. Fig. 4.18 shows a comparison between the simulated vs measured values for the directivity and gain of the fabricated transmitarray at different frequencies across the bandwidth. The measured 1dB gain bandwidth is 13.1%. Overall, there is very good agreement between simulations and measurements. Table 4.3 shows a comparison of our proposed transmitarray antenna with other designs published in the literature in terms of thickness, aperture efficiency, -1dB gain bandwidth, beam peak angle, and conical scanning capability.

82

Table 4.2:
Off-axis fed 18 cm transmitarray measured performance statistics (f=13.4 GHz).

	Position 1 Simulated	Positions 1-4 Measured Averaged	Position 5 Simulated	Position 5 Measured	Position 1 Simulated Rotated Feed	Position 1 Measured Rotated Feed
Directivity (dBi)	24.1 dBi	24.2 dBi	24.0 dBi	24.2 dBi	24.3 dBi	24.1 dBi
HPBW	8.3°	8.3°	8.4°	8.5°	8.5°	8.3°
SLL E-plane	-11.4 dBi	-12.7 dB	-13.9 dB	-12.8 dBi	-11.7 dBi	-9.2 dBi
$|\theta_b|$	25.0°	25.0°	25.2°	25.2°	25.2°	25.0°
e_{ap}	40.3%	41.2%	40.0%	41.2%	42.2%	40.3%
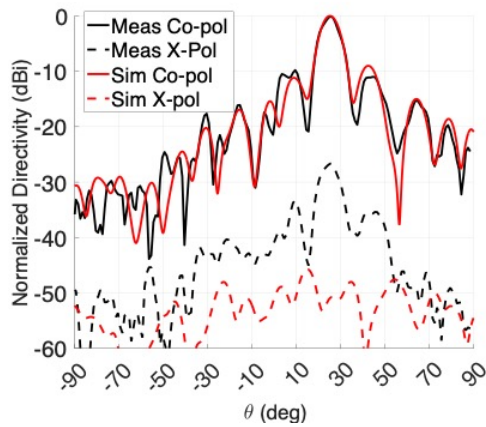
(a) f=12.5 GHz
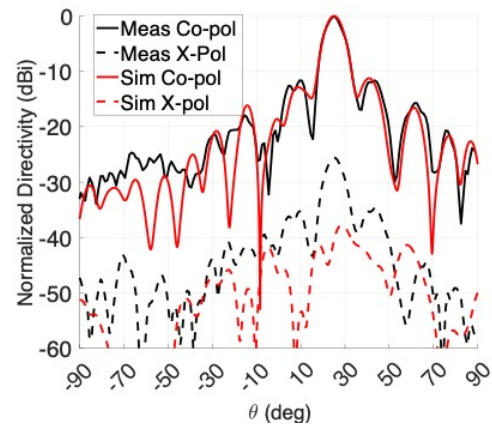
(b) f=13.0 GHz.
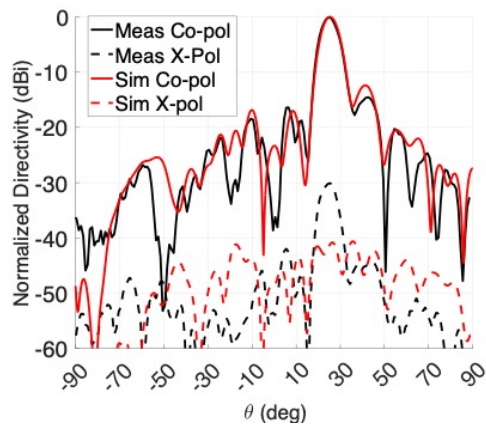
(c) f=14.0 GHz.
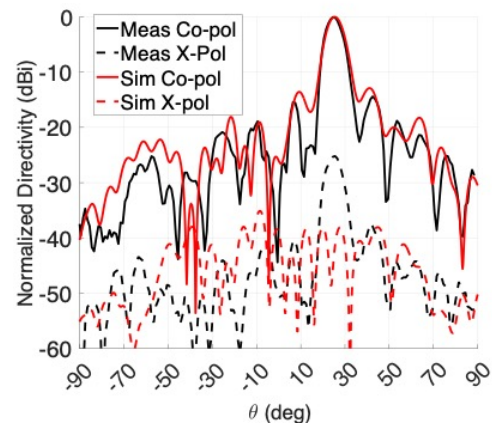
(d) f=14.5 GHz.

Figure 4.17 Transmitarray off-axis fed design measured normalized radiation patterns at different frequencies.
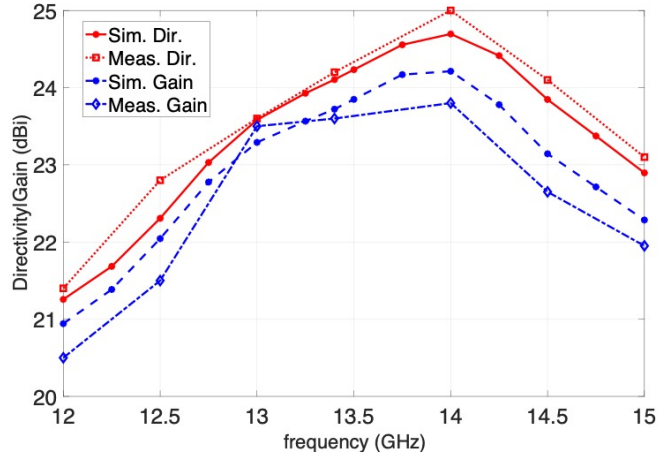
Figure 4.18 Simulated vs measured values for the directivity and gain of the fabricated transmitarray at different frequencies.

Table 4.3:
Comparison of the proposed transmitarray with other references.

Ref.	Thickness	Aperture Efficiency	-1dB Gain Bandwidth	Beam Peak θ_b	Conical Scanning Capability
[125]	$0.76\lambda_0$	47.0%	11.7%	0°	No
[32]	$0.27\lambda_0$	36.5%	-	30°	No
[129]	$0.58\lambda_0$	14.6%	4.9%	30°	No
[21]	$4.60\lambda_0$	37.0%	-	33°	Yes
This work	$0.36\lambda_0$	35.9%	13.1%	25°	Yes

4.6   Summary

This chapter presented a novel transmitarray antenna for switched beam type conical pattern sweep of a highly-directive beam. The scan in a conical sweep is produced through successive excitation of feeds placed along the body of revolution ring focus. This is the first transmitarray that is designed for conical beam scanning. To address this challenging problem, a novel transmitarray synthesis algorithm was presented based on a modified transmitarray phase compensation coupled to the PSO of the feed location. An 18 cm transmitarray was designed using this approach and a proof-of-concept prototype was manufactured. The transmitarray with a ring-type focus was populated with individual feed antennas at five positions within the

ring focus and characterized through far-field measurements. The measured results agree well with predictions obtained from full-wave simulations and demonstrate the conical scanning capabilities of the proposed transmitarray.

CHAPTER 5

Orbital Angular Momentum Beams: Novel Mathematical Insights, Transmitarray Generation and Measurement Validation

5.1   OAM Beams: Perspectives and Research Objectives

For antenna applications, the synthesis of proper antenna aperture field allows the generation of the desired far-field radiation pattern. Conventionally, an aperture field with uniform phase distribution is desired to achieve a directive antenna radiation pattern. For example, the lens antennas presented in chapters 2-4 aim to achieve uniform exit aperture phase (or the intended phase gradient for the desired beam scan angle) for maximum directivity [25, 30]. Synthesizing novel antenna aperture fields will allow one to generate unconventional radiation patterns with out-of-the-box characteristics.

A case of particular interest is the OAM beams. Table 5.1 summarizes the theoretical and experimental milestones regarding OAM in chronological order. OAM's aperture field has an $e^{jl\phi}$ dependency in its phase, where ϕ is the azimuthal variable in the aperture and l is an integer corresponding to the OAM mode number [140, 141]. This unique azimuthal phase variation is also referred to as "vortex" or "helical" phase. OAM beams exhibit two unique properties: the orthogonality of different OAM modes and the cone-shaped far-field pattern of OAM beam. The large number of orthogonal OAM modes provides additional sets of data carriers, which offers the potential to increase the capacity and spectral efficiency of wireless communication links. The cone-shaped pattern of the OAM beam can be advantageous for applications that require cone-shaped patterns, such as geosynchronous satellite-based

Table 5.1: Chronicle of milestones regarding OAM.

Reference	Year	Main Contribution
[147]	1909	Theoretically studied angular momentum of circularly-polarized waves
[148]	1936	Experimentally studied the SAM of light and demonstrated that SAM can cause the rotation of a mechanical system
[140]	1992	Recognized that light beams with an azimuthal phase dependence of $e^{jl\phi}$ carry OAM
[149]	2004	Conducted first experiment on OAM free space optical communications
[150]	2006	Reported the generation of an OAM-carrying optical vortex in optical fibers
[151]	2007	Numerically showed that OAM can be used in the radio frequency domain
[152]	2012	Performed the first experimental test of encoding multiple channels on the same radio frequency through OAM
[153]	2013	Conducted the first OAM-DM experiment suggesting that OAM could provide an additional degree of freedom for data multiplexing in future fiber networks
[50]	2018	Suggested a potential application that takes advantage of the OAM cone-shaped pattern in the far-field

navigation and guidance systems that serve moving vehicles and ceiling-mounted indoor wireless systems, as shown in Fig. 5.1 [50, 142]. Note that since OAM beam is divergent, a large receiving aperture is required to capture the entire beam for OAM-DM modulation applications, as shown in Fig. 5.2. This poses a challenge for far-field communication links since the size of the receiving antenna might become impractical. The requirement to collect enough power of the divergent OAM beam with a very large aperture (compared to wavelength) significantly limits the achievable distance of OAM communication links [143], especially for radio frequencies, where the wavelengths are larger compared to optical frequencies. In particular, references [49, 144, 145] question the possibility of using OAM antennas in long-distance communication links. They highlight that in order to achieve the required signal-to-noise ratio at the receiver endpoint the physical size of the receiving antenna becomes very large. The impact of the finite receiving aperture size and the misalignment (lateral and angular) between the transmitter and the receiver on the performance of an optical OAM communication link was investigated in [146].

Harnessing the unique features of OAM for real-life communications applications entails
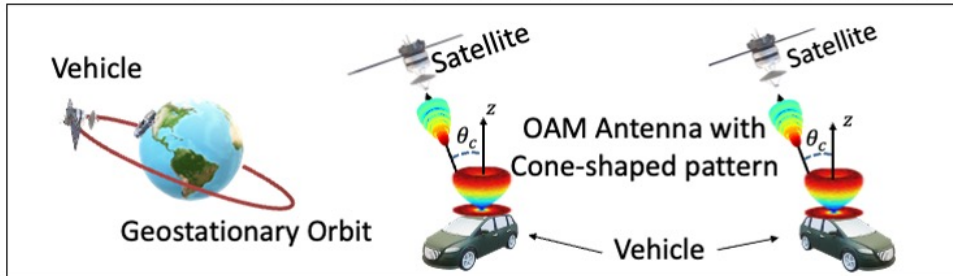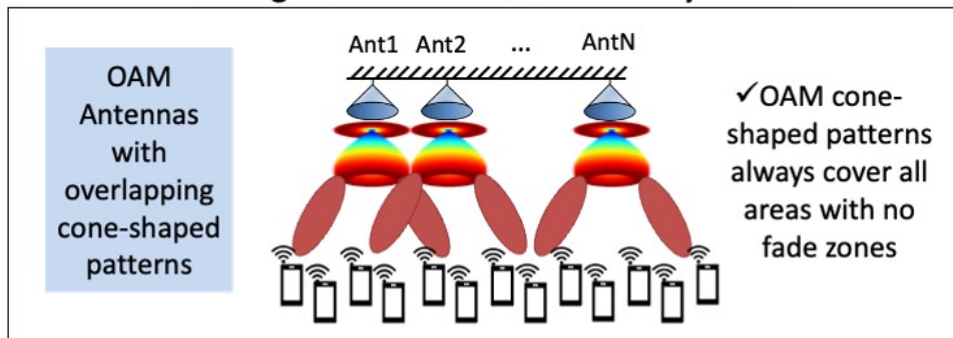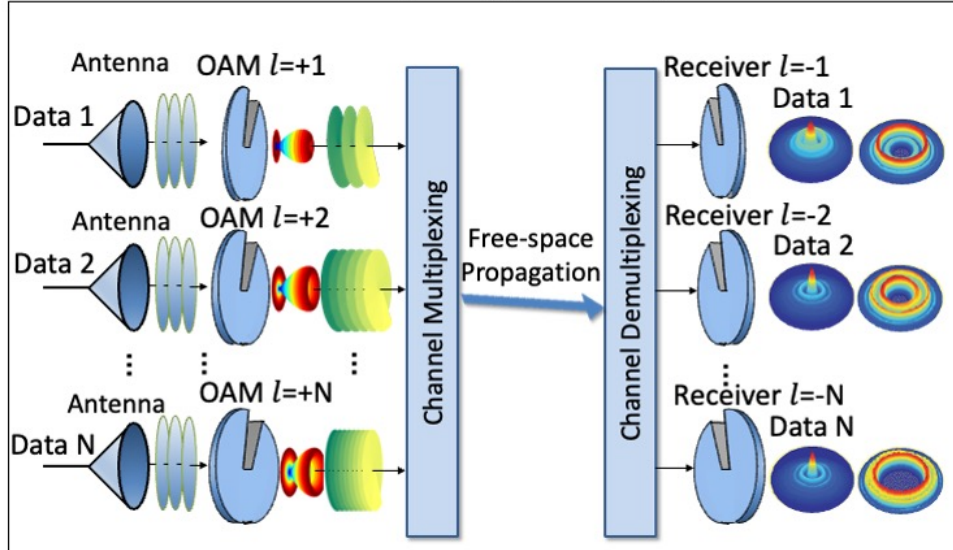
Figure 5.1 Potential applications involving OAM antennas.
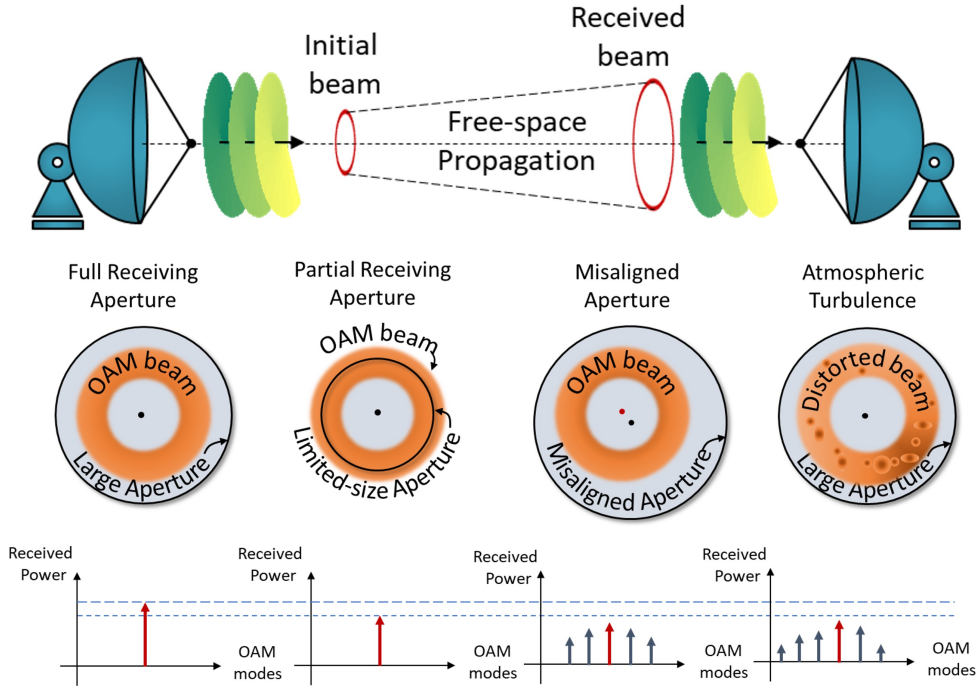
Figure 5.2 OAM beam is divergent: A large receiving aperture is required to capture the entire beam for OAM-DM modulation. This poses a challenge for far-field communication links since the size of the receiving antenna might become impractical.

numerous engineering challenges yet to be overcome, one of which falls on the development of antennas that can generate CP OAM beams. This challenge also comes with the lack of a comprehensive and systematic characterization of the far field properties of OAM beams that would potentially facilitate the design of OAM antennas. This chapter addresses these challenges as follows: First, we provide insight into the far field properties of OAM beams using the antenna aperture field method. Semi-analytical expressions for the far field of a general cylindrically-symmetric OAM aperture field are derived using the classical antenna aperture field method. The far-field properties of both LP and CP OAM carrying fields are considered. In particular, we reveal the major far-field characteristics including the polarization and phase variation. For two common OAM-carrier aperture field distributions, i.e., the generalized Airy disk with uniform amplitude distribution and the Laguerre-Gaussian distribution, analytical expressions of their fields are also obtained in closed forms. The equations obtained in this chapter lead to several insightful observations that are validated through full-wave simulations.

89

The derived analytical and semi-analytical formulas can potentially guide the design of OAM communication systems. Second, we propose transmitarray antennas for the generation of CP OAM beams. A novel "S-ring" transmitarray element is designed to sustain CP operation with only three metal patterned layers. We present the synthesis, prototyping and measurement validation of a proof-of-concept prototype with a thickness of 3 mm operating at 19 GHz. The measurements agree well with predictions obtained by full-wave simulations and demonstrate that the proposed transmitarray antenna can be a unique apparatus that generates OAM CP cone-shaped patterns.

5.2 Mathematical Insights into the Far-Field Properties of OAM Beams

Driven by the recent increasing scientific interest and research on OAM communications, we revisit the fundamentals of OAM beams and provide insight into their far-field properties. Our main analysis tool is the classical antenna aperture field method, which is well-established in electromagnetics textbooks and widely applied in the analysis of conventional antennas [30, 51, 154, 155]. To the author's best knowledge, there has not been a comprehensive and systematic characterization of the far-field properties of OAM beams [49, 50] (some aspects have been discussed in [49, 50] but not thoroughly investigated). The significance of understanding the far-field properties of OAM beams is manifested as the following: (i) in many application scenarios, an OAM-carrying radiation is characterized in the far-field. Therefore, the understanding of OAM's far-field polarization, phase, etc. can be crucial to establishing effective OAM communications links and understanding inherent limitations; (ii) analytical or semi-analytical expressions for the OAM far-fields can provide proper guidelines to the design of OAM antennas (an example can be found in the domain of conventional reflector antennas where the analytical formulas of the Airy disk, i.e. the uniform amplitude and phase aperture field distribution, facilitate the antenna design [30, 51]).

5.2.1 OAM Beams: Field Evolution and Analogies with Conventional Beams

To provide insight into the OAM field distribution at various distances far from the antenna, we studied the changes of amplitude pattern shape from the reactive near-field toward the far-field. The first case of study is a conventional reflector antenna with uniform aperture phase and -10 dB edge taper. The aperture field distribution is modeled using the two-parameter (2P) model [30, eq. (16)], and the field at various distances is calculated using the Fresnel–Kirchhoff diffraction integral [156]. The second case of study is a helicoidal reflector, where the aperture field is modeled using the [30, eq. (16)] multiplied by the phase term $e^{-jl\phi}$, for $l = 1$. The aperture diameter for both cases is $D = 10\lambda$ at 19 GHz. The changes of amplitude pattern shape from the reactive near-field toward the far-field for the two cases are shown in Fig. 5.3. The pattern is calculated at $r = 4.9\lambda, 24\lambda, 8000\lambda$ corresponding to the reactive near-field, radiating near-field and far-field regions. It can be observed that the amplitude null at the center is maintained at all distances.

5.2.2 Aperture Field Method

The classical antenna aperture field method has been discussed in many popular textbooks (see for example, [154, 155]) and is one of the common tools for the analysis of aperture antennas. Note that any antenna can be regarded as an aperture antenna with the proper choice of an aperture plane, as discussed in [49, 155]. A schematic of the antenna aperture field method as applied for the case of a conventional reflector antenna and an OAM antenna is shown in Fig. 5.4. In what follows, we use the antenna aperture field method to study the far-field characteristics of OAM beams and provide significant insights.

5.2.2.1 LP OAM Field

The tangential aperture field of an OAM-carrying LP field with a cylindrically-symmetric amplitude distribution can be written as:

$$\vec{E}_{\mathrm{LP}}(\rho', \phi') = E(\rho')e^{-jl\phi'}\hat{x}, \quad 0 < \rho' < a \tag{5.1}$$

91
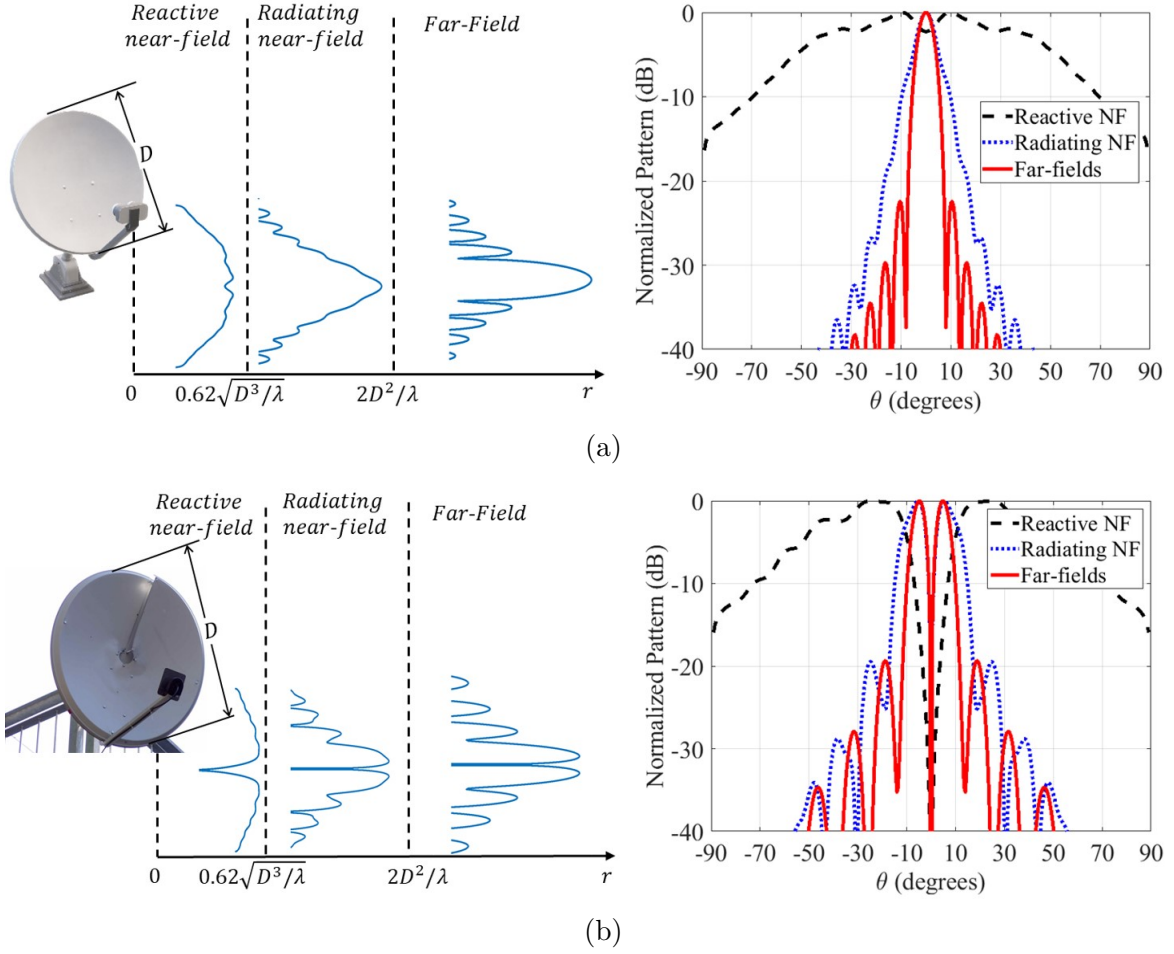
Figure 5.3 Changes of amplitude pattern shape from the reactive near-field toward the far-field for (a) a conventional antenna and (b) an OAM antenna. The dimensions are $D = 10\lambda$ and the pattern is calculated at $r = 4.9\lambda, 24\lambda, 8000\lambda$ corresponding to the reactive near-field, radiating near-field and far-field regions.

where ρ' and ϕ' are the radial and azimuthal coordinates in the cylindrical coordinate system; a is the transverse extend of the aperture field; $j = \sqrt{-1}$ is the imaginary unit; l is the OAM mode number; $\hat{x}$ represents the direction of the linear polarization. The equivalent magnetic current density can be calculated from [154, eq. 6-129b] as:

$$\vec{M}_s = -\hat{z} \times \vec{E}(\rho', \phi') = -\hat{y}E(\rho')e^{-jl\phi'}, \quad 0 < \rho' < a \tag{5.2}$$
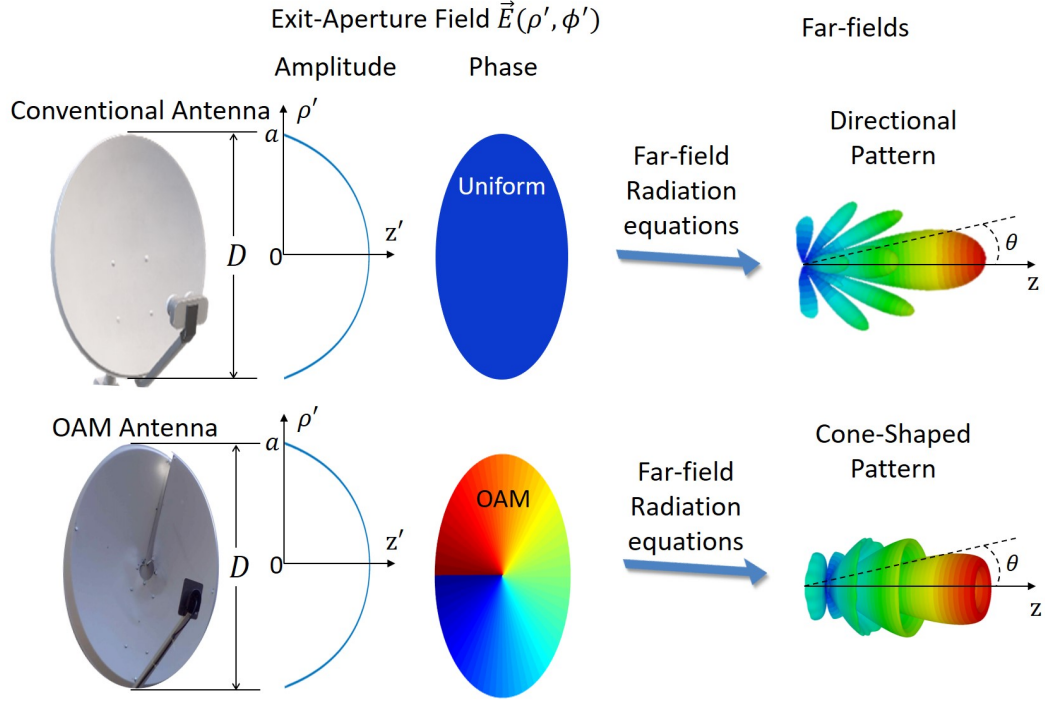
Figure 5.4 Schematic of antenna aperture field method for conventional and OAM antennas.

Using the integral identity [50, eq. 5]:

$$\int_0^{2\pi} e^{-jl\phi'} e^{jk_0\rho'\sin\theta\cos(\phi-\phi')} d\phi' = 2\pi(-j)^l J_l(k_0\sin\theta\rho') e^{-jl\phi} \tag{5.3}$$

where $k_0 = 2\pi/\lambda$ is the free-space wavenumber with λ being the free-space wavelength, we find the expression of the far-field integrals using [154, eq. 6-125c, 6-125d]:

$$L_\theta = -2\pi\cos\theta\sin\phi(-j)^l e^{-jl\phi} I \tag{5.4}$$

$$L_\phi = -2\pi\cos\phi(-j)^l e^{-jl\phi} I \tag{5.5}$$

where

$$I = \int_0^a E(\rho') J_l(k_0\sin\theta\rho')\rho' d\rho' \tag{5.6}$$

and $J_l(\cdot)$ is the lth-order Bessel function of the first kind [157]. Note that the integration in (5.6) is performed on the radial coordinate ρ' in the aperture, and I is a function of θ

with the wavenumber k_0 being a constant. The expression of the far-field electric field can be written as [154, eq. 6-122b, 6-122c]:

$$\vec{E}_{\mathrm{LP}}^{ff}(r,\theta,\phi) = \frac{jk_0 e^{-jk_0 r}}{2r}(-j)^l e^{-jl\phi}\left(\hat{\theta}\cos\phi - \hat{\phi}\cos\theta\sin\phi\right)I \qquad (5.7)$$

In what follows, we apply the aperture field method for the calculation of the far-field electric field of a circularly-polarized field.

5.2.3 CP OAM Field

The tangential aperture field of an OAM-carrying CP field with a cylindrically-symmetric amplitude distribution $E(\rho')$ can be written as:

$$\vec{E}_{\mathrm{CP}}(\rho',\phi') = E(\rho')e^{-jl\phi'}(\hat{x}\pm j\hat{y})/\sqrt{2}, \quad 0 < \rho' < a \qquad (5.8)$$

where "$-$" and "$+$" signs in (5.8) indicate RHCP and LHCP waves, respectively. The equivalent magnetic current density is calculated from [154, eq. 6-129b]:

$$\vec{M}_s = (j\hat{x}\mp\hat{y})/\sqrt{2}\times E(\rho')e^{-jl\phi'}, \quad 0 < \rho' < a \qquad (5.9)$$

The far-field integrals can be found using equations [154, eq. 6-125c, 6-125d] by virtue of the integral identity (5.3):

$$L_\theta = \pm j\cos\theta e^{\pm j\phi}\sqrt{2}\pi(-j)^l e^{-jl\phi}I \qquad (5.10)$$

$$L_\phi = -e^{\pm j\phi}\sqrt{2}\pi(-j)^l e^{-jl\phi}I \qquad (5.11)$$

The expression of far-field electric field is then calculated using [154, eq. 6-122b, 6-122c]:

$$\vec{E}_{\mathrm{CP}}^{ff}(r,\theta,\phi) = \frac{jk_0 e^{-jk_0 r}}{2r}\frac{(-j)^l}{\sqrt{2}}e^{\pm j\phi}e^{-jl\phi}\left(\hat{\theta}\pm j\cos\theta\hat{\phi}\right)I \qquad (5.12)$$

where "$-$" and "$+$" signs in (5.12) correspond to RHCP and LHCP cases. The significance

of the far-field expressions (5.7) and (5.12), as well as the immediate consequences will be expanded upon section 5.2.3.1.

5.2.3.1 Observations on the Far-field Expressions of OAM Beam

In what follows, we examine the general far-field expressions (5.7) and (5.12) of OAM beam with linear and circular polarization. In particular, our goal is to understand the far-field signature and phase characteristics of OAM beams. Some observations are made as the following:

(a) For a LP OAM beam, the electric field maintains the phase term $e^{-jl\phi}$ in the far-field. In other words, the phase observed in the far field maintains the same azimuthal gradient as that in the aperture field.

(b) For a CP OAM beam, an additional phase term of $e^{+j\phi}$ (for RHCP), or $e^{-j\phi}$ (for LHCP) occurs in addition to the helical-phase term $e^{-jl\phi}$ in its far field. In other words, the far-field phase of a CP OAM aperture field has a different azimuthal gradient from that in the aperture: for RHCP OAM beam, an aperture phase variation of $e^{-jl\phi}$ will result in a far field phase variation of $e^{-j(l-1)\phi}$; for LHCP OAM beam, an aperture phase variation of $e^{-jl\phi}$ will result in a far field phase variation of $e^{-j(l+1)\phi}$. The near-field azimuthal phase variation, or more specifically, the constant l, is what determines the OAM order. Whereas the additional term $e^{\pm j\phi}$ is a manifestation of circular polarization in the far field, and has no relation with OAM. In fact, it can be observed from (5.12) that the term $e^{\pm j\phi}$ even appears when the CP aperture has a uniform phase (i.e., $l = 0$). As will be elaborated in the following, it is crucial to acknowledge this far-field phase characteristic in the OAM purity analysis.

(c) The mode decomposition is a common method to assess the OAM mode purity of an OAM beam in antenna applications [158]. This is obtained by applying the Fourier transform on the far-field phase distribution $P(\phi)$ [159]:

$$A_{l_{\text{LP}}} = \frac{1}{2\pi} \int_0^{2\pi} P(\phi)e^{-jl\phi}d\phi \tag{5.13}$$

95

where $P(\phi)$ is the extracted phase of the far field at a constant elevation angle θ, which is usually chosen at the peak of the cone-shaped OAM pattern (see, for example, [158]); A_l is the magnitude weight of the mode l across the OAM spectrum. (5.13) is valid for LP OAM beams. However, according to previous discussion in Section 5.2.3.1(b), (5.13) must be modified for CP OAM beams as follows:

$$A_{l_{CP}} = \frac{1}{2\pi} \int_0^{2\pi} P(\phi)e^{-j(l\mp 1)\phi}d\phi \tag{5.14}$$

with the "$-$" sign taken for RHCP, and "$+$" taken for LHCP. Equation (5.14) cancels the additional term of $e^{\pm j\phi}$ that occurs in the far-field of a CP OAM beam, and exposes the correct azimuthal phase variation for mode purity analysis. This ensures the correct determination of OAM order of a CP OAM beam. Failing to include the correcting factor will result in wrong interpretation of the received OAM order, and consequently lead to impaired signal level. These equations will be verified in Section 5.2.5 with full-wave simulation results.

(d) The sense of polarization in the aperture field is maintained in the far-field: according to (5.7) and (5.12), the phase difference between the $\hat{\theta}$- and $\hat{\phi}$- components is 0° for LP OAM beam, and ±90° for CP OAM beam. For a CP antenna, the axial ratio (AR) is a measure of its CP purity in the far field, and is defined as the ratio of the magnitudes of $\hat{\theta}$- and $\hat{\phi}$- components. For a CP OAM antenna, its AR at a given elevation angle θ_c can be obtained based on (5.12) as:

$$\mathrm{AR} = \frac{1}{\cos(\theta_c)} \tag{5.15}$$

This equation shows that the minimum theoretically achievable AR increases as the observing elevation angle increases. This is an important observation especially when considering the cone-shaped far-field pattern of an OAM beam [50, 160]. Since the OAM far field in general peaks at an elevation angle that is non-zero (except for 0th mode), the far field at the peak can no longer maintain the circular polarization purity, even with a perfectly pure CP aperture field. (5.15) serves as the baseline of achievable

Table 5.2: Minimum theoretically achievable AR of circularly-polarized OAM antennas at various beam peak elevation angles θ_c, as predicted by (5.15).

θ_c	AR_{min}	AR_{min} (dB)
0°	1.00	0 dB
15°	1.04	0.30 dB
30°	1.15	1.21 dB
45°	1.41	3.01 dB
60°	2.00	6.02 dB
75°	3.86	11.74 dB

AR of a CP OAM communication system. As an example, the minimum theoretically achievable AR for an OAM CP antenna with a peak at $\theta_c = 45°$ would be 3.01 dB, which hardly satisfies the common requirement of AR < 3 dB [161]. The minimum achievable AR for different OAM peak angles are tabulated in Table 5.2.

5.2.4 Illustrative Examples

In general, with a given aperture field distribution, the integral I in (5.7) or (5.12) can be numerically evaluated to determine its far-field. In this section we demonstrate two special aperture field distributions, for which the integration of (5.6) can be analytically evaluated to provide closed-form expressions. In particular, the generalized Airy disk and the Laguerre-Gaussian beam are investigated because: (i) both possess analytical expressions that provide insightful observations and can serve as guidelines for the design of OAM antennas; (ii) both cases are among the most common aperture field models of conventional antennas and OAM antennas [30, 142, 149, 162–166].

5.2.4.1 Generalized Airy Disk

The Airy disk pattern is produced by a circular aperture field with uniform amplitude and phase. It is a common and useful model in the design of conventional aperture-type antennas, such as reflectors [30]. The generalized Airy disk is defined as an aperture field with uniform amplitude distribution and with a phase variation described as $e^{-jl\phi}$. Without loss of generality, we begin with a LP aperture field with uniform amplitude and phase,

which is effectively the special case of (5.1) with $l = 0$ and $E(\rho') = E_0^{\text{AD}}$. Using the integral identity [157, eq. 6.561-5]:

$$\int_0^{\delta} z J_0(z) dz = \delta J_1(\delta) \tag{5.16}$$

we find I from (5.6) and the far-field expression from (5.7):

$$\vec{E}_{\text{AD,l=0}}^{ff}(r, \theta, \phi) = \frac{j k_0 E_0^{\text{AD}} a^2 e^{-jk_0 r}}{2r} \left(\hat{\theta} \cos \phi - \hat{\phi} \cos \theta \sin \phi \right) \frac{J_1(\Psi)}{\Psi} \tag{5.17}$$

where $\Psi = k_0 a \sin \theta$. Note that the electric field of the Airy disk in (5.17) has a maximum at the boresight when $\theta = 0$ when $l = 0$, and corresponds to a directed far-field pattern. For any other $l \neq 0$ and $\theta > 0$, the far-field of an OAM-carrying field with uniform aperture distribution can be calculated using the integral identity [157, eq. 6.561-13] can be written as:

$$\vec{E}_{\text{AD},l}^{ff}(r, \theta, \phi)$$
$$= \frac{j k_0 E_0^{\text{AD}} a^2 e^{-jk_0 r}}{2r} (-j)^l e^{-jl\phi} \left(\hat{\theta} \cos \phi - \hat{\phi} \cos \theta \sin \phi \right) \tag{5.18}$$
$$\left[\frac{2\Gamma(l/2 + 1)}{\Psi^2 \Gamma(l/2)} + \frac{l J_l(\Psi) S_{0,l-1}(\Psi) - J_{l-1}(\Psi) S_{1,l}(\Psi)}{\Psi} \right]$$

In (5.18), $J_l(\cdot)$ is the lth-order Bessel function of the first kind, $S_{\mu,\nu}(\cdot)$ is the Lommel function, and $\Gamma(\cdot)$ is the Gamma function [157].

Similar to the relationship between (5.7) and (5.12), the far-field expression of a CP generalized Airy disk can be readily found by simply multiplying the LP expression by $e^{\pm j\phi}(-j)^l/\sqrt{2}$ and replacing $(\hat{\theta} \cos \phi - \hat{\phi} \cos \theta \sin \phi)$ in (5.18) with $(\hat{\theta} \pm j \cos \theta \hat{\phi})$.

5.2.4.2 Laguerre-Gaussian Beam

The Laguerre-Gaussian modes are a special subset among all OAM-carrying beams that are cylindrically-symmetric solutions to the paraxial wave equation in the cylindrical coordinate system [140]. The Laguerre-Gaussian modes are chosen to be presented because they are one of the most popular example of OAM-carrying beams (see, for example, [149, 165, 166]). More importantly, a general OAM-carrying beam can be expanded by a complete basis of Laguerre-

Gaussian modes [162–164]. The tangential electric aperture field of a LP Laguerre–Gaussian beam at $z = 0$ can be written as [50, 140]:

$$\vec{E}_{\text{LG}}(\rho', \phi', z' = 0) = \sqrt{\frac{2p!}{\pi(p + |l|)!}} \frac{E_0^{LG}}{w_g} \left(\frac{\rho'\sqrt{2}}{w_g}\right)^{|l|} e^{-\frac{\rho'^2}{w_g^2}} L_p^{|l|}\left(\frac{2\rho'^2}{w_g^2}\right) e^{-jl\phi} \hat{x} \quad (5.19)$$

where ρ' and ϕ' are the radial and azimuthal coordinates in the cylindrical coordinate system; E_0^{LG} is a complex amplitude coefficient; l and p are integers known as azimuthal and radial mode numbers; w_g is the equivalent beam waist that can be related to the antenna aperture diameter D (refer to [50] for more details) and is equal to the half-width of the normalized aperture field amplitude at $1/e$ controlling the transverse extent of the beam; $L_p^l(\cdot)$ is the associated Laguerre polynomial [157]:

$$L_p^l(x) = \frac{1}{p!} e^x x^{-l} \frac{d^p}{dx^p}\left(e^{-x} x^{p+l}\right) = \sum_{m=0}^{p} (-1)^m \binom{p+l}{p-m} \frac{x^m}{m!} \quad (5.20)$$

where the binomial coefficient is [157]:

$$\binom{n}{k} = \frac{n!}{k!\,(n-k)!} \quad (5.21)$$

when $k \le n$ and is zero when $k > n$. For $l = 0$, the Laguerre-Gaussian beam carries no OAM since the phase term $e^{-jl\phi}$ vanishes. For any other l, the field carries the phase term $e^{-jl\phi}$, which gives rise to an OAM state of l-order. The normalized electric field intensity (i.e. the electric field amplitude squared given by (5.19)) distributions of Laguerre-Gaussian beams with different azimuthal and radial modes l and p are shown in Fig. 5.5, where each Laguerre-Gaussian mode for different l, p is normalized to its own maximum. It can be observed that the number of side lobe intensity rings is equal to the integer p. For the same p, the null size (i.e. the divergence angle) increases as the azimuthal mode number l increases. Using the integral identity [157, eq. 7.421-4]:

$$\int_0^\infty x^{\nu+1} e^{-\beta x^2} L_n^\nu(ax^2) J_\nu(xy) dx = 2^{-\nu-1} \beta^{-\nu-n-1} (\beta - a)^n y^\nu e^{-\frac{y^2}{4\beta}} L_n^\nu\left[\frac{ay^2}{4\beta(a-\beta)}\right] \quad (5.22)$$

99
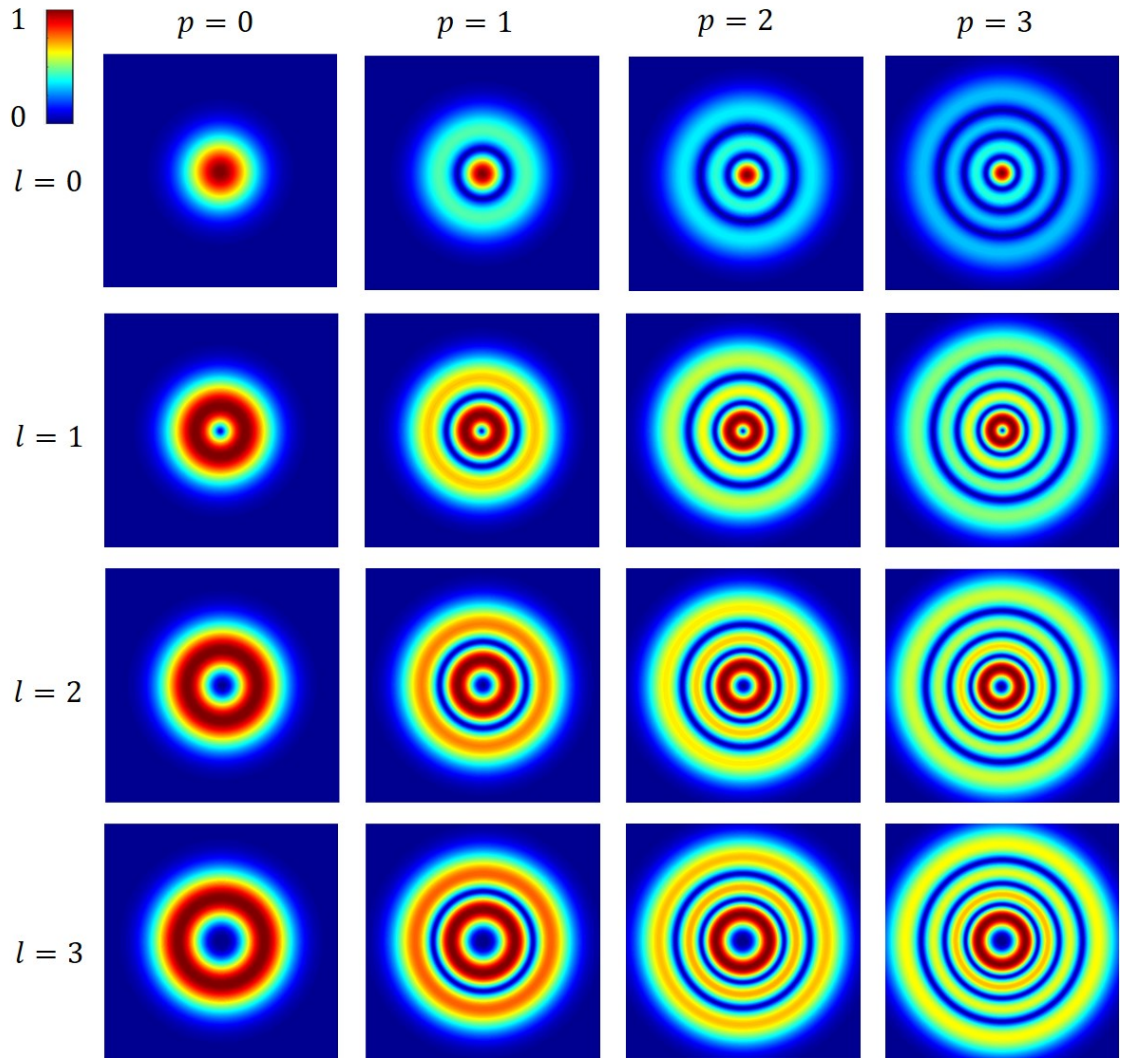
Figure 5.5 Normalized exit-aperture field intensity (i.e. the electric field amplitude squared given by (5.19)) distributions versus ρ/w_g of Laguerre-Gaussian beams with different azimuthal and radial modes l and p, where each mode is normalized to its own maximum.

It is worth noting that, the "∞" in the integral limit originates from the fact that Laguerre-Gaussian functions extend to infinity (unlike the generalized Airy disk) along ρ with an exponential decay (see, for example, [162,163,167]). While ideally we take the integration from 0 to ∞, there exist a point beyond which the function's contribution to the integral becomes negligible. Therefore, in practice, even with a finite aperture (truncating the infinitely defined function) one can still sustain Laguerre-Gaussian beam with reasonable accuracy. With this in mind, we find I from (5.6) and the far-field expression from (5.7):

$$\vec{E}^{ff}_{\text{LG}_{l,p}}(r, \theta, \phi)$$
$$= \frac{jk_0 E_0^{\text{LG}} e^{-jk_0 r}}{4\pi r} \left(\hat{\theta} \cos\phi - \hat{\phi} \cos\theta \sin\phi \right)$$
$$w_g(-1)^p(-j)^l \times \sqrt{\frac{2\pi p!}{(p+|l|)!}} \left(\text{sgn}(l) \frac{\psi}{\sqrt{2}} \right)^{|l|} \qquad (5.23)$$
$$e^{-\frac{\psi^2}{4}} L_p^{|l|} \left(\frac{\psi^2}{2} \right) e^{-jl\phi}$$

where $\psi = k_0 w_g \sin\theta$. Equation (5.23) is a cone-shaped pattern with azimuthal symmetry. The far-field expression for the Laguerre-Gaussian mode with $p = 0$ can be simplified:

$$\vec{E}^{ff}_{\text{LG}_{l,p=0}}(r, \theta, \phi) = \frac{jk_0 E_0^{\text{LG}} e^{-jk_0 r}}{4\pi r} \left(\hat{\theta} \cos\phi - \hat{\phi} \cos\theta \sin\phi \right) w_g(-j)^l \sqrt{\frac{2\pi}{|l|!}} \left(\frac{\text{sgn}(l)\psi}{\sqrt{2}} \right)^{|l|} e^{-\frac{\psi^2}{4}} e^{-jl\phi}$$

For the dominant radial mode $p = 0$, the far-field expression (5.24) peaks at the elevation angle of:

$$\theta_c^{\text{LG}} = \sin^{-1} \left(\frac{\sqrt{2|l|}}{k_0 w_g} \right) \qquad (5.24)$$

Equation (5.24) shows that the cone angle depends on both the azimuthal mode number l and the beam waist (i.e., aperture diameter, as was shown in [50]). For a given l, the cone angle decreases as we increase the beam waist w_g, i.e. the aperture diameter. For constant w_g, the cone angle increases as we increase the mode number l.

5.2.5   Full Wave Simulations and Comparisons

In this section, we present the full-wave simulation results to verify the observations made from the analytical formulas derived in previous sections. In CST Microwave Studio, a planar near-field source containing specified E- and H-field within a finite region was used to represent the radiating aperture. The transient solver in CST was then used to calculate the far field of this aperture source. For example, we defined a circular aperture field with a diameter of $D = 2a = 12$ cm (7.6λ) at 19 GHz to simulate the generalized Airy disk. For
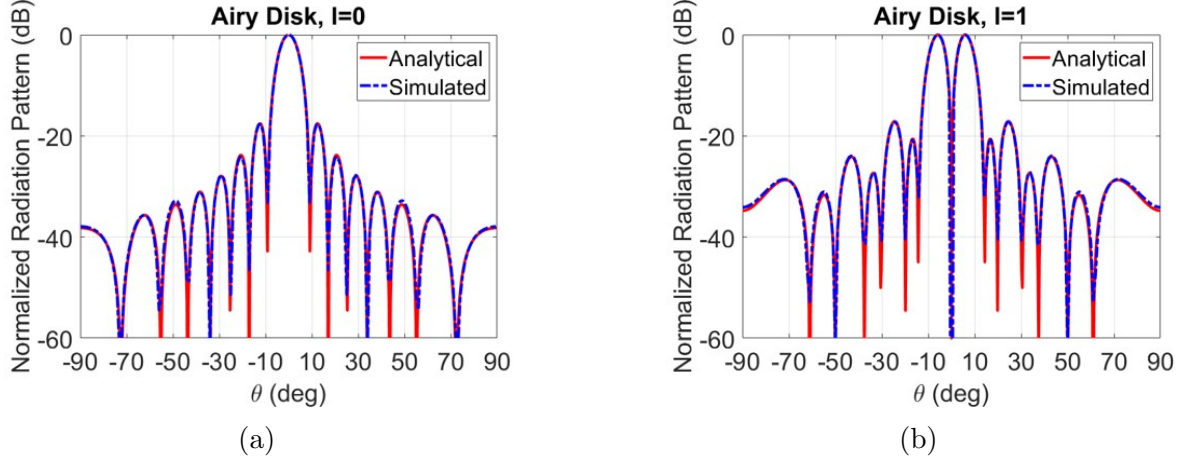
Figure 5.6 Comparison between the analytical expressions (5.18)-(5.17) and the simulated data for the generalized Airy Disk radiation pattern for different OAM mode numbers l for $f = 19$ GHz and $D = 2a = 7.6\lambda = 12$ cm.

OAM mode order $l = 0$ and $l = 1$, the CST simulated far-field patterns are compared with those predicted using (5.18) and (5.17) in Fig. 5.6. We also modeled the Laguerre-Gaussian aperture distribution given by (5.19) for different azimuthal and radial OAM mode numbers p, l, for $f = 19$ GHz and beam waist $w_g = 3.15\lambda$, which is the same that was used in reference [50]. Excellent agreement between the simulated and analytically predicted patterns for both the generalized Airy disk and the Laguerre-Gaussian distribution was achieved as shown in Figs. 5.6-5.7, thus validating our method of aperture field simulations in CST.

Then, several CP (generalized Airy disk) aperture fields for different OAM mode order l were defined and simulated. For both RHCP and LHCP cases, the phase of the E_θ component of the simulated far field are plotted in Fig. 5.8. These phase plots clearly reveal the far-field azimuthal phase variation as predicted by the analytical expressions. More importantly, the rate of change of the phase along azimuth certainly manifests the characteristic predicted in Section 5.2.3.1: the phase changes by $2\pi|l \pm 1|$ after a full turn, with the "$-$" and "$+$" signs corresponding to RHCP and LHCP respectively. As can be told from Fig. 5.8, for $l = 0$, the far-field phase of RHCP and LHCP OAM beam possess an azimuthal phase variation of -2π and 2π, even though neither of them carries OAM. As another example, the far-field phase of the LHCP for $l = -1$ is uniform along azimuth, even though it carries OAM of order -1. This is because the $e^{-j\phi}$ term in (5.12) (manifestation of LHCP) cancels the

102
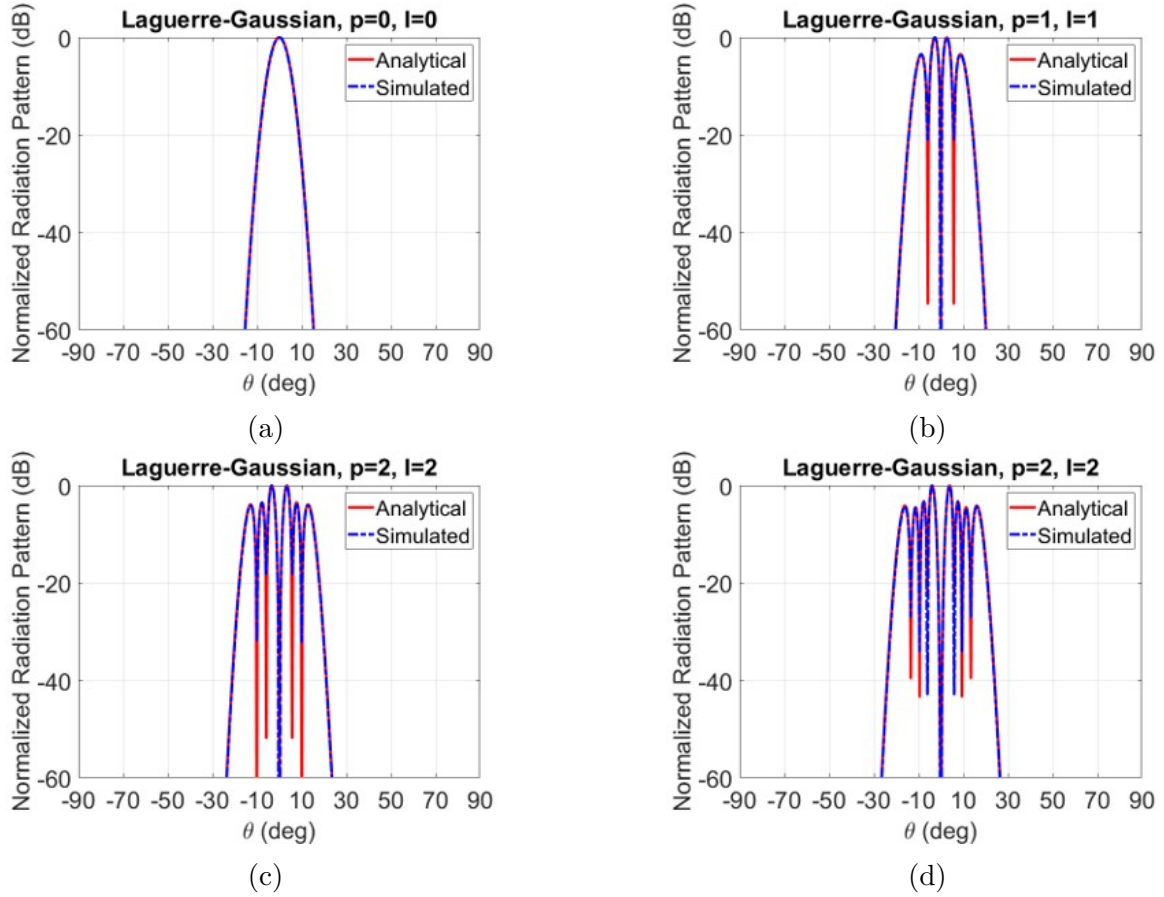
Figure 5.7 Comparison between the analytical expressions (5.23)-(5.24) and the simulated data for the Laguerre Gaussian radiation pattern for different azimuthal and radial OAM mode numbers p, l, for $f = 19$ GHz and beam waist $w_g = 3.15\lambda$ (same as in reference [50]).

helical-phase term $e^{+j\phi}$ of OAM mode number $l = -1$. Additional simulation results show that similar observations regarding the far-field azimuthal phase variation hold for the RHCP and LHCP Laguerre-Gaussian modes. These results validate our observations, and emphasize on the necessity of using the modified equation (5.14) for determination of OAM order in CP scenarios.

Fig. 5.9 shows the simulated AR of the RHCP and LHCP generalized Airy Disk for different OAM mode number l, and their comparison with the minimum theoretically achievable AR predicted by (5.15). The simulated AR agrees really well with the theoretically predicted behavior: when the observing elevation angle θ increases, the AR increases as $1/\cos(\theta)$.

Fig. 5.10(a) shows the simulated directivities of the generalized Airy disk versus the OAM
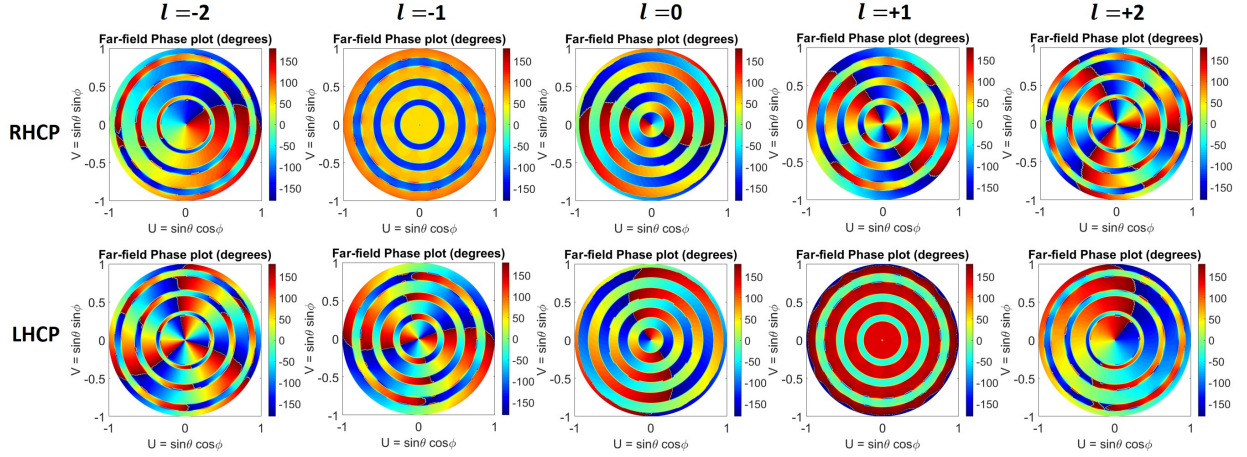
Figure 5.8 Simulated far-field phase of E_θ component for RHCP and LHCP cases of the generalized Airy disk for different OAM mode numbers l. The frequency is $f = 19$ GHz and the aperture diameter is $D = 2a = 7.6\lambda = 12$ cm.
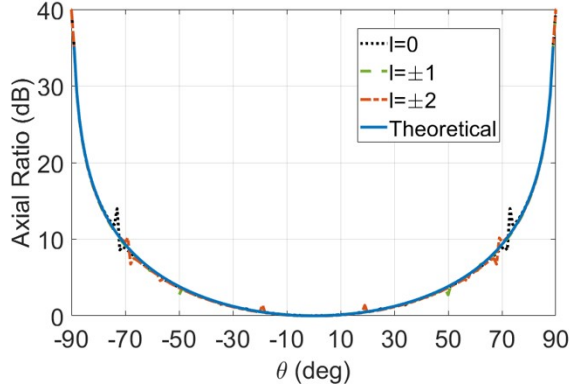
Figure 5.9 AR for RHCP and LHCP generalized Airy disk patterns for different OAM mode numbers l and the minimum theoretically achievable AR that is predicted by (5.15). The frequency is $f = 19$ GHz and the aperture diameter is $D = 7.6\lambda = 12$ cm.

mode number for fixed aperture dimensions: $D = 2a = 7.6\lambda$ at $f = 19$ GHz. The directivity decreases and the cone angle θ_c increases as the OAM number increases. Fig. 5.10(b) shows the effect of the dimension of the aperture, by considering fixed OAM order $l = 2$. It can be observed that the directivity decreases and the cone angle θ_c increases as the aperture diameter increases.
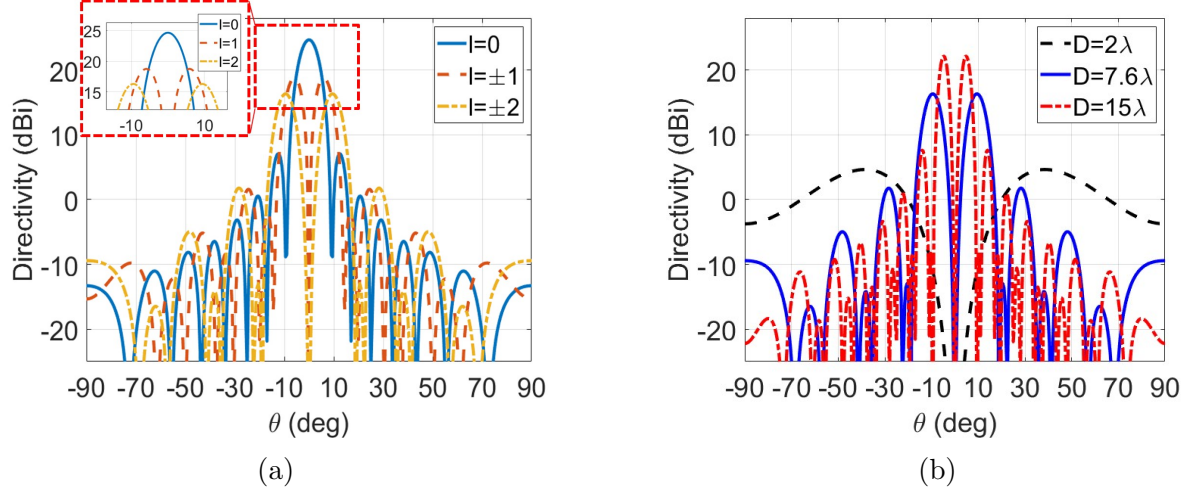
Figure 5.10 Simulated directivities of generalized Airy disk versus (a) the OAM mode number for fixed $D = 2a = 7.6\lambda$ (b) the aperture diameter $D = 2a$ for fixed OAM number $l = 2$.

5.3 Transmitarray Antenna Generating CP OAM Beams

In the second part of this chapter, we present the design, prototyping and measurement results of a novel transmitarray generating OAM CP beams with cone-shaped radiation pattern.

5.3.1 Unit Cell of the OAM Transmitarray

The RF performance of a transmitarray antenna is largely determined by the unit cell. In this section, we present the design of a novel "S-ring" element transmitarray unit cell to support CP. The S-ring element along with the dimensions are shown in Fig. 5.11. The unit cell consists of only three metal patterned layers separated by two dielectric substrates (Rogers RO3003) with dielectric constant $\epsilon_r = 3$ and loss tangent $\tan\delta = 0.001$. The unit cell can provide arbitrary CP phase compensation by proper rotation of the elements, which allows the constituent transmitarray to synthesize the helical OAM aperture phase. This property renders more flexibility to the design of CP unit cells, since the desired unit cell transmission phase can be easily controlled by element rotation, and one can focus dominantly on the optimization of transmission magnitude.

The "S-ring" patterns on three layers are identical and have the same orientations. When

105

P (mm)	Rout (mm)	Rin (mm)	w (mm)	α (deg.)	t (mm)
5.8 (0.37λ)	2.26	1.73	0.53	53	1.52
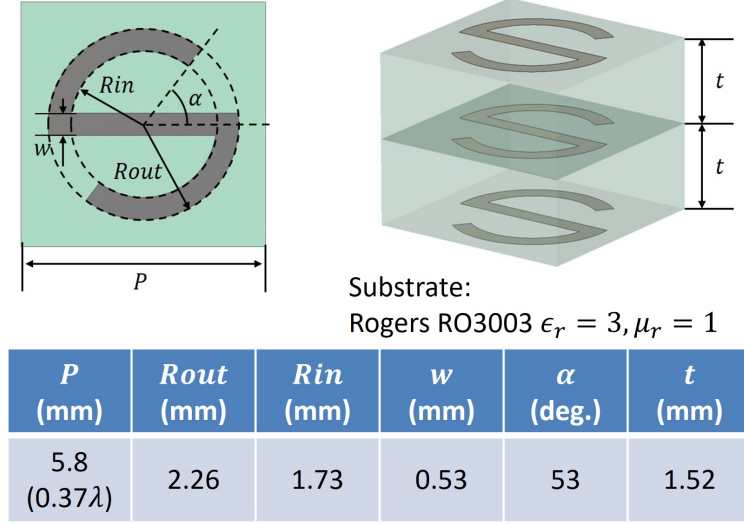
Figure 5.11 The proposed CP transmitarray unit cell using "S-ring" element, designed for 19 GHz. (λ: free-space wavelength at 19 GHz). $P = 0.37\lambda = 5.8$ mm, $t = 1.52$ mm, and other parameters were optimized to maximize the LHCP transmission coefficient that is shown in Fig. 5.12.

the "S-ring" element is rotated about the center, the transmitted CP phase will manifest a linear dependency on the rotation angle. In particular, when the incident wave is RHCP and the element is rotated counter-clockwise by angle ϕ_0, the transmitted LHCP component will experience a phase shift of $2\phi_0$; whereas under LHCP incidence, the transmitted RHCP component will experience the phase shift of $-2\phi_0$ [168]. More detailed derivations of this property can be found in [169] and in the Appendix B. By utilizing this property, the unit cell can easily achieve arbitrary CP phase shift through mere rotation of the element [170]. Moreover, since the rotation-dependent phase shift exists only in the opposite handedness component in the transmitted side, the "S-ring" unit cell was thus optimized to maximize the magnitude of transmission of the oppositely polarized component. In other words, the wave will flip its CP handedness after passing the unit cell.

Fig. 5.12 shows the simulated phase and amplitude of the LHCP transmission coefficient under RHCP incidence, versus the rotation angle ϕ_0. It can be observed that for different element rotation angles ϕ_0, the transmission coefficient remains high (> 0.9, or say > -0.92 dB). The transmission phase also demonstrated a linear dependency on rotation angle ϕ_0 and
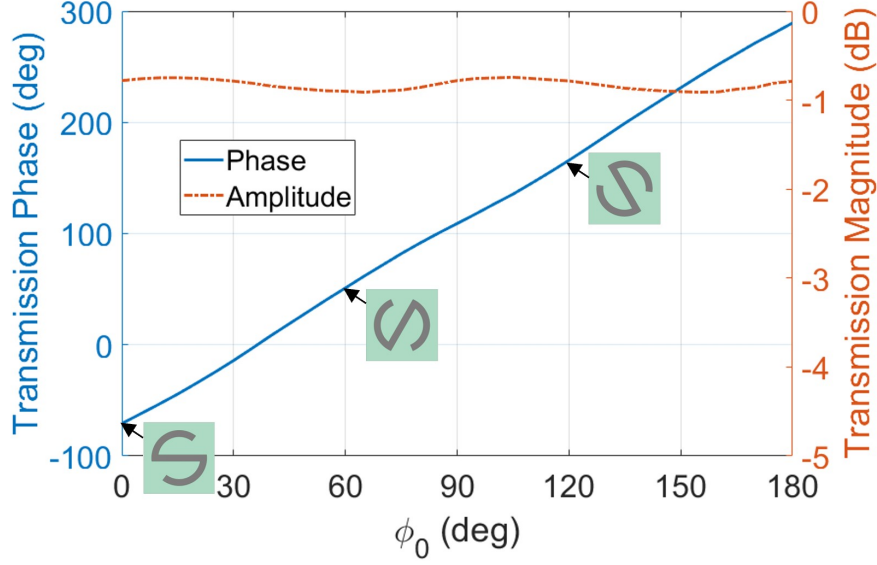
Figure 5.12 The LHCP transmission coefficient versus "S-ring" element rotation angle when the unit cell is under RHCP excitation at 19 GHz.

covers 360°, as expected. Fig. 5.13 shows the unit cell transmission magnitude and phase for different rotation angles ϕ_0 versus frequency, where T_{RL} and T_{LL} are the transmission coefficients of the LHCP component under RHCP and LHCP excitation, respectively. Compared to existing transmitarray unit cells that are based on the variation of the dimensions [171], the proposed "S-ring" unit cell is thinner (has fewer layers), has continuous 360° phase coverage, with high and stable transmission magnitude.

5.3.2 OAM Transmitarray Design

In most existing works, transmitarrays that support circular polarization were designed based on the assumption of normal plane wave incidence, thus the feed source of the transmitarray must be placed far from the transmitarray (see, for example, references [172, 173]). This results in lower efficiency due to high spillover loss and increased system dimensions thus making it unsuitable for satellite or vehicle platforms. In order to overcome this disadvantage, we present a methodology for the design of OAM transmitarrays that can work with feed sources at a reasonably close distance (we choose $F/D = 1$ as an example) where the plane wave assumption is not valid. Instead, the input wave from the feed source has a spherical
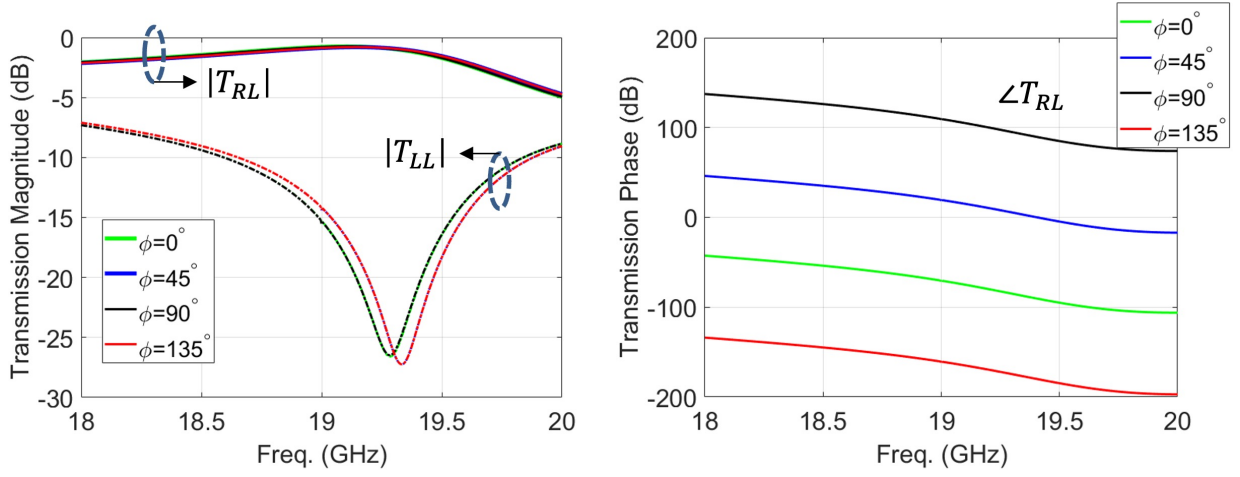
Figure 5.13 Simulated unit cell transmission magnitude and phase for different rotation angles ϕ_0 versus frequency. T_{RL} and T_{LL} are the transmission coefficients of the LHCP component under RHCP and LHCP excitation, respectively.
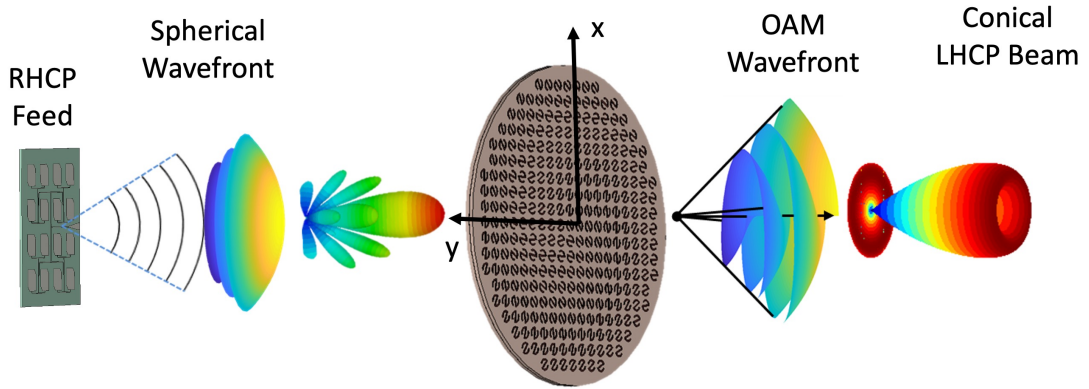
Figure 5.14 Illustration of OAM CP transmitarray operational principle.

wavefront. An illustration of the TA operational principles is shown in Fig. 5.14. Therefore, the ideal phase compensation of the OAM transmitarray should be the superposition of the spherical phase compensation ϕ_{sph} and the helical phase for the generation of OAM ϕ_{OAM} [171, 174]. Following this methodology, the phase compensation $\phi_i(x_i, y_i)$ for each unit cell in the transmitarray can be determined based on their locations (x_i, y_i) in the array as:

$$\phi_i(x_i, y_i) = \phi_{\text{sph}}(x_i, y_i) + \phi_{\text{OAM}}(x_i, y_i) \qquad (5.25)$$
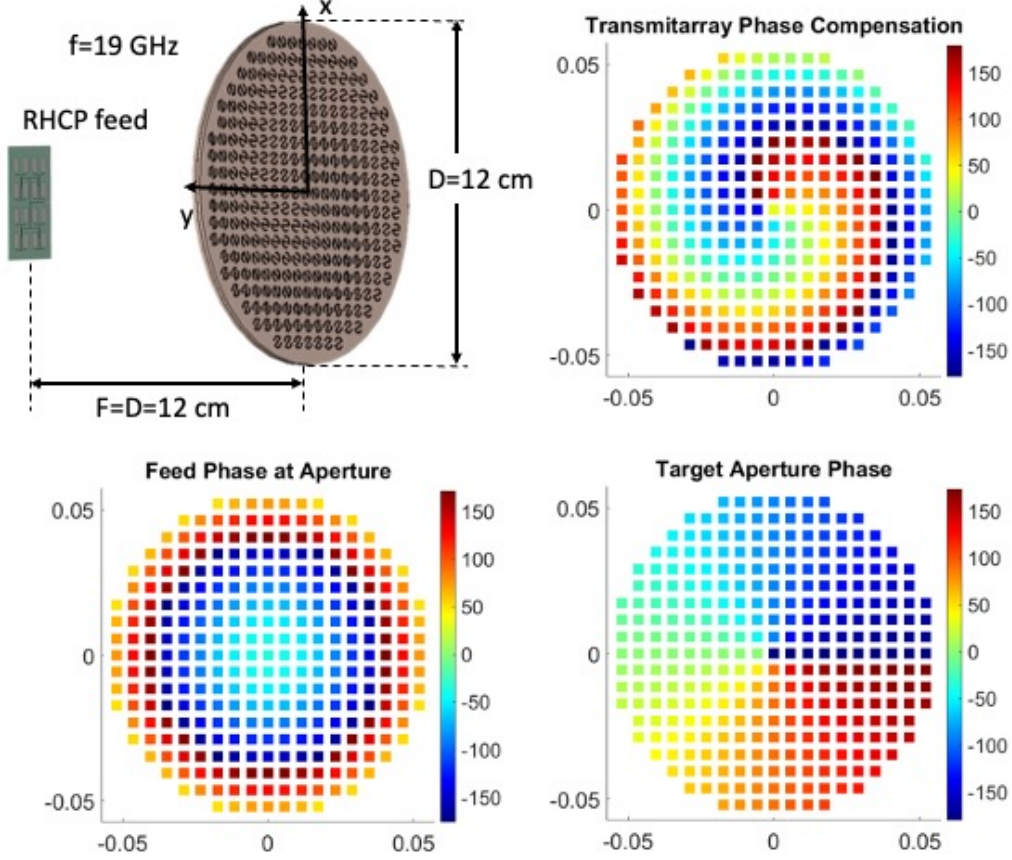
Figure 5.15 Geometry of the transmitarray under consideration.

$$\phi_{\mathrm{sph}}(x_i, y_i) = k_0(\sqrt{x_i^2 + y_i^2 + F^2} - F) \tag{5.26}$$

$$\phi_{\mathrm{OAM}}(x_i, y_i) = l \times \tan^{-1}(y_i/x_i) \tag{5.27}$$

where $k_0 = 2\pi/\lambda$ is the free-space wavenumber and λ is the free space wavelength; l is the OAM mode number; F is the focal distance; $R_i = [(x_i - x_f)^2 + y_i^2 + F^2)]^{(1/2)}$ is the distance from the feed to the i$^{\mathrm{th}}$ transmitarray element. The geometry of the transmitarray under consideration as well as the transmitarray phase compensation are shown in Fig. 5.15. The transmitarray diameter is D=12 cm, the focal distance is F=12 cm, the operating frequency is f=19 GHz and the OAM mode number is chosen to be $l = 1$ as an example. The transmitarray is designed to work with an RHCP feed and to generate an LHCP OAM beam.
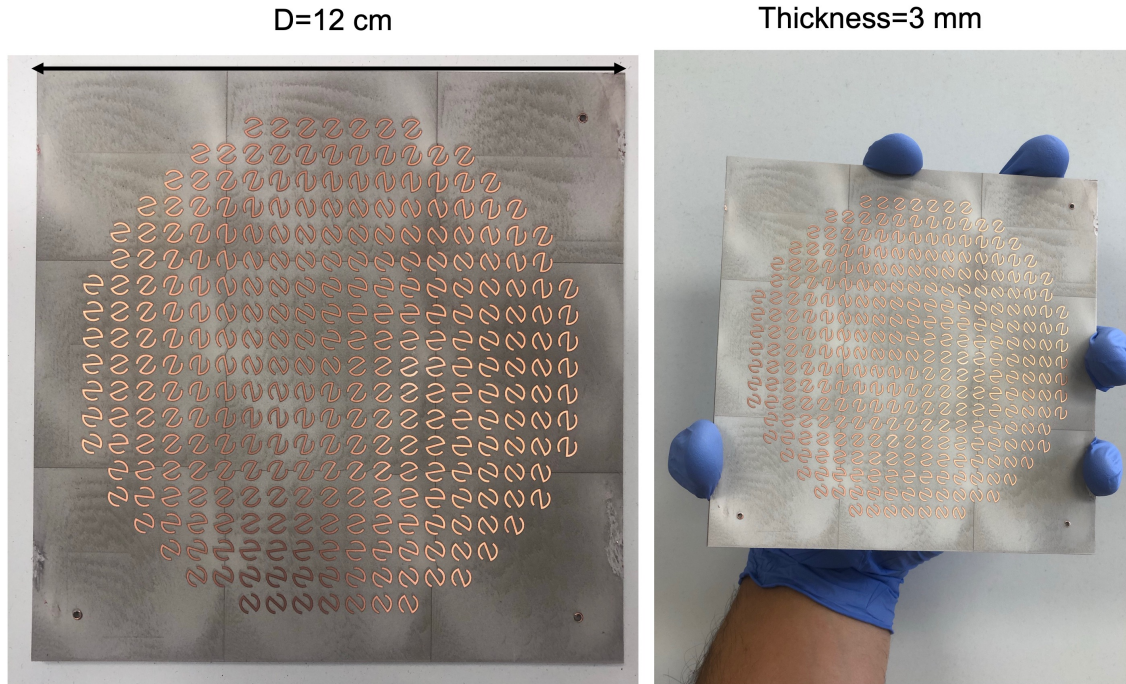
Figure 5.16 Fabricated transmitarray prototype at 19 GHz and laser etching process using a LPKF ProtoLaser U4 machine.

The total thickness of the transmitarray is only 3.04 mm ($\approx 0.19\lambda$). Note that an advantage of this design is that, contrary to the meta-lenses [25], which are analyzed based on the ray approach and their thickness, i.e., the number of required dielectric layers and therefore the thickness and weight, scales with the lens diameter, the proposed design is low-profile (only two dielectric substrates are required) with reduced thickness that is independent of the transmitarray diameter.

5.3.3   Simulations, Prototyping and Measurements

The synthesized transmitarray of section 5.3.2 was constructed with a standard laser etching process using a LPKF ProtoLaser U4 machine on two pieces of 1.52 mm-thick Rogers RO3003 substrates. The fabricated transmitarray prototype at 19 GHz is shown in Fig. 5.16. The transmitarray was positioned at the UCLA spherical near field measurement range and was illuminated by a RHCP patch array feed (Fig. 5.17(a)).

The simulated and measured results are compared in Fig. 5.17(a)-(b) demonstrating a
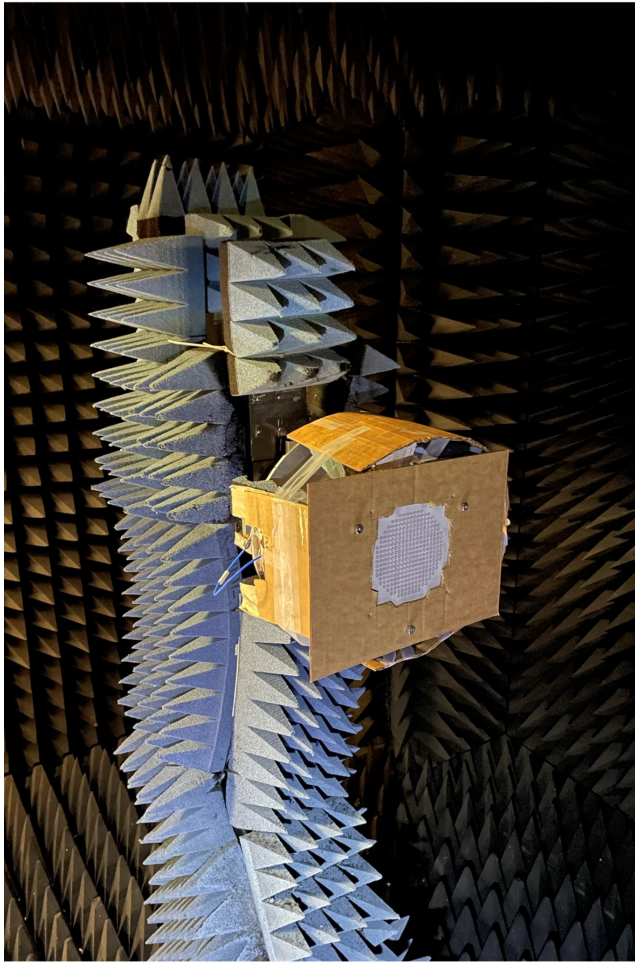
(a)
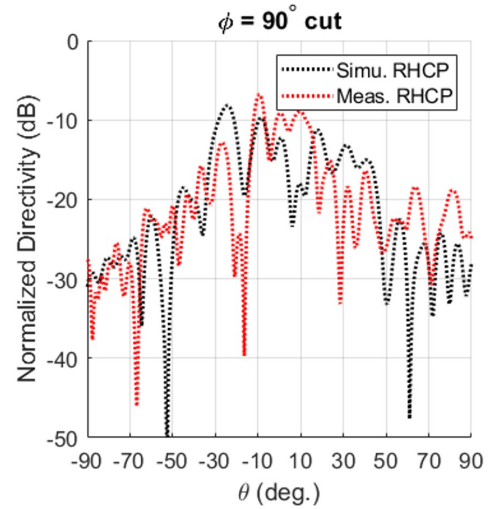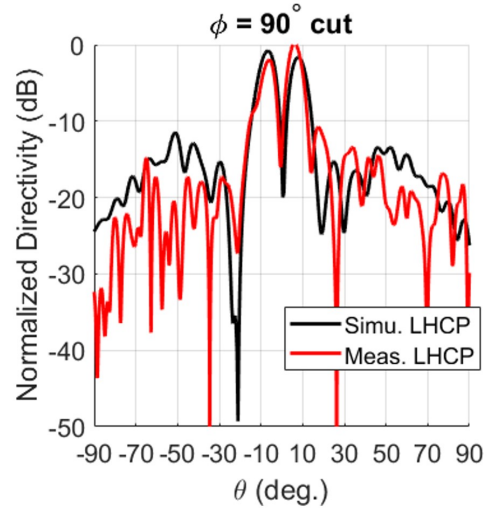
(b)

Figure 5.17 (a) Transmitarray measurement setup in the UCLA spherical measurement range. Simulated and measured (b) co-pol (LHCP) and x-pol (RHCP) radiation patterns of the proposed transmitarray antenna at 19 GHz demonstrating a CP OAM cone-shaped pattern.

LHCP OAM cone-shaped pattern with a deep null at the boresight. The simulated and measured directivities are 16.6 dBi and 17.1 dBi, and the simulated and measured beam peak angles are 7 and 6.8 degrees, respectively. Additionally, the mode decomposition was performed based on (5.14). Fig. 5.18 shows the simulated and measured mode decomposition of the proposed transmitarray with the desired $l = 1$ OAM mode having more than 80% mode purity. To study the bandwidth of the transmitarray itself without the feed, the transmitarray was also simulated around the center frequency of 19 GHz for the AR performance and the
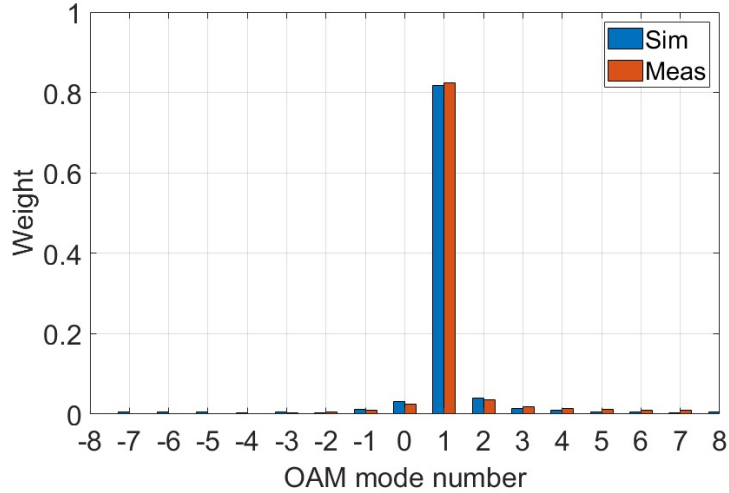
Figure 5.18 Simulated and measured mode decomposition of the proposed transmitarray, demonstrating more than 80% mode purity for the desired $l = 1$ OAM mode.
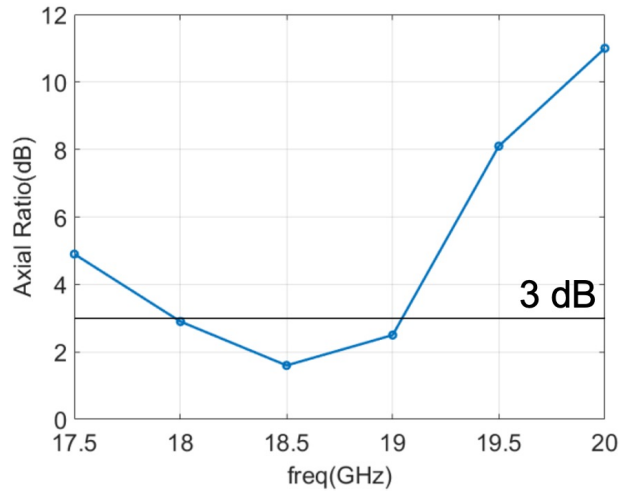
Figure 5.19 Simulated AR bandwidth versus frequency around the center frequency of 19 GHz. The transmitarray demonstrated a 5.2% 3-dB AR bandwidth.

results are shown in Fig. 5.19. The AR bandwidth is 5.2%. The transmitarray was also simulated using an ideal RHCP $\cos^q(\theta)$ feed with q=11.5 for -12 dB edge taper from 16 to 22 GHz with a step of 0.5 GHz. The weight of the desired $l = 1$ OAM mode is greater than 80% for all frequencies demonstrating the broadband features of the transmitarray. The measurements agree well with predictions obtained by full-wave simulations and demonstrate that the proposed transmitarray can generate OAM CP beam.

5.4 Summary

This chapter presented presented both an insightful study on the far-field properties of OAM-carrying beams and the design, prototyping and measurement results of a novel transmitarray generating OAM CP beams with cone-shaped radiation pattern. First, the aperture field method was employed in our theoretical analysis and semi-analytical expressions were derived for the far field of a general OAM aperture field. For two specific OAM-carrying aperture field distributions: the generalized Airy Disk and the Laguerre-Gaussian distribution, we also demonstrated that closed-form expressions can be obtained to explicitly describe their far fields. These theoretical studies lead to several instructive conclusions that are validated with full-wave simulations: (i) Both LP and CP OAM beams maintain the helical phase term $e^{-jl\phi}$ in the far field, but CP OAM far field carries an additional $e^{\pm j\phi}$ term, where "$-$" and "$+$" correspond to RHCP and LHCP waves; (ii) The commonly used OAM mode decomposition technique in (5.13) is valid only for LP cases. In case of CP, one needs to account for the additional $e^{\pm j\phi}$ term to obtain the correct mode order, as in (5.14); (iii) The minimum theoretically achievable AR at the peak angle θ_c of a CP OAM beam is regulated by $1/\cos(\theta_c)$, meaning the CP purity at the peak of an OAM beam becomes worse as the cone angle increases. These unique far-field characteristics of OAM can become advantageous for the modeling, design and analysis of OAM-based communication systems. Second, we proposed a methodology based on superimposing the spherical compensation and the OAM phase compensation to generate the OAM beam without necessitating the plane wave approximation; thus, the feed can be placed near the aperture at about $F/D = 1$. A novel ultra-thin "S-ring" element unit cell that supports CP was introduced to realize the CP OAM flat transmitarray. The fabricated OAM transmitarray was measured at 19 GHz. A conical OAM beam was successfully generated and a good agreement with simulation was achieved. These results have validated our concept and revealed the potential of this transmitarray to generate OAM CP cone-shape patterns.

CHAPTER 6

Conclusion

This dissertation presented four antenna designs directly addressing the needs of real-life applications requiring conical beam scanning and cone-shaped patterns.

First, a novel 3D-printed lightweight inhomogeneous lens antenna for spaceborne wind scatterometers was revisited in Chapter 2. In the past, only on-axis designs were addressed; however, real life application requires conical beam scanning that necessities special attention to the developments, optimization, and prototyping. The developments presented in this dissertation significantly enhance previous works only addressing the on-axis beam case. The presented azimuthally symmetric lens is designed to contain a ring-type focus which can be populated with individual feed antennas for switched beam type conical pattern sweep of a highly-directive beam. The antenna is designed as an all-electronic replacement for the traditional mechanically driven design. The lens was designed using curved-ray GO and PSO. An 18 cm example was designed, 3D-printed using FDM printing process, and characterized through far-field measurements. The measurements prove the conical beam sweep by comparing measurements taken at five locations within the ring focus. The lens can be used in future scatterometer instruments requiring all electronic scanning mechanisms. Future work includes the design and prototyping of 3D-printed lenses with larger diameters as well as the lens 3D-printing using space-qualified materials such as Ultem [23]. Future research on space-qualified materials, including thermal and electrostatic discharge issues, as well as the development of an electronically switched feeding network along the lens ring focus that will ultimately produce the conical scan all electronically will pave the way for the integration of this type of design in next-generation satellite missions.

In Chapter 3, multi-Layered meta-lenses were proposed as lightweight alternatives to

conventional homogeneous dielectric lenses. The methodology presented in Chapter 2 based on a linkage between GO and PSO was customized to synthesize the refractive index of meta-lens antennas. The applied numerical synthesis algorithm was used to synthesize both on-axis and off-axis fed flat lenses with circular symmetry thus providing conically scanned beams for the off-axis designs. Then, metamaterial elements of variable sizes distributed on planar dielectric substrates were used to form a multi-layered flat metamaterial lens and satisfy the required refractive index distribution. Simulation and near-field/far-field measured results of a proof-of-concept prototype of a flat-layered meta-lens operating at 13.4 GHz were also presented. Additionally, microwave holographic approach was used to evaluate the goodness of the exit aperture phase. Future research on the automatic deployment mechanism of the flat-layered meta-lens, space-qualified materials, thermal, and electrostatic discharge issues will pave the way for the integration of collapsible meta-lenses in telecommunications and scientific satellite missions. The concept could also be used for other applications where low weight is important. Future research includes the extension to circular polarization operation and the development of an automatic deployment mechanism for the integration of this new lens in practical applications. The possibility to extend this concept at shorter wavelengths (Ka, V bands) will entail challenges regarding the fabrication tolerances and high dielectric loss at higher frequencies [175]. This is an area that future investigations could be warranted.

Chapter 4 presented a novel transmitarray antenna for switched beam type conical pattern sweep of a highly-directive beam. The scan in a conical sweep is produced through successive excitation of feed placed along the body of revolution ring focus. To address this challenging problem, a novel transmitarray synthesis algorithm was presented based on a modified transmitarray phase compensation coupled to the PSO of the feed location. An 18 cm transmitarray was designed using this approach and a proof-of-concept prototype was manufactured. The transmitarray with a ring-type focus was populated with individual feed antennas at five positions within the ring focus and characterized through far-field measurements. The measured results agree well with predictions obtained from full-wave simulations and demonstrate the conical scanning capabilities of the proposed transmitarray.

Future work includes the design of transmitarrays for conical beam scanning that support circular polarization and/or operating at different frequency bands. The manufacturing of transmitarrays conventionally employs the printed circuit board process, where the metallic patterns at the transmitarray aperture are produced by removing the unneeded metallic parts of a complete piece of copper-plated laminates. Future research includes the fabrication of transmitarrays using additive manufacturing processes such as charge-programmed three-dimensional multi-material printing [130].

Chapter 5 presented both an insightful study on the far-field properties of OAM-carrying beams and the design, prototyping and measurement results of a novel transmitarray generating OAM CP beams with cone-shaped radiation pattern. The aperture field method was employed in the theoretical analysis and semi-analytical expressions were derived for the far field of a general OAM aperture field. It was demonstrated that closed-form expressions can be obtained for the generalized Airy Disk and Laguerre-Gaussian beams to explicitly describe the far fields. These theoretical studies lead to several conclusions that are validated with full-wave simulations: (i) Both LP and CP OAM beams maintain the helical phase term $e^{-jl\phi}$ in the far field, but CP OAM far field carries an additional $e^{\pm j\phi}$ term, where "−" and "+" correspond to RHCP and LHCP waves; (ii) The commonly used OAM mode decomposition technique in (5.13) is valid only for LP cases. In the case of CP, one needs to account for the additional $e^{\pm j\phi}$ term to obtain the correct mode order, as in (5.14); (iii) The minimum theoretically achievable AR at the peak angle θ_c of a CP OAM beam is regulated by $1/\cos(\theta_c)$, meaning the CP purity at the peak of an OAM beam becomes worse as the cone angle increases. These unique far-field characteristics of OAM can become advantageous for the modeling, design and analysis of OAM-based communication systems. In the second part of Chapter 5, a methodology was proposed based on superimposing the spherical compensation and the OAM phase compensation to generate the OAM beam without necessitating the plane wave approximation. A novel ultra-thin "S-ring" element unit cell that supports CP was introduced to realize the CP OAM flat transmitarray. The fabricated OAM transmitarray was measured at 19 GHz. A conical OAM beam was successfully generated and a good agreement with simulation was achieved. These results have validated our concept and revealed the

potential of this transmitarray to generate CP OAM cone-shape patterns. The integration of OAM antennas in practical applications is an area where future research is warranted. Future work includes the development of OAM transmitarrays that support broadband CP as well as the development of OAM mode-reconfigurable transmitarrays.

APPENDIX A

Geometrical Optics Analysis

This appendix provides an overview of the GO tool that was used in chapters 2-3 as part of the GO-PSO synthesis algorithm. GO is a computational electromagnetics techniques for wave propagation in inhomogeneous media and can be used to calculate the far-field pattern of the lenses. The developments of this appendix rely on the previous works [20, 121]. GO is a very convenient formulation for lens design. It derives from the asymptotic solution of Maxwell equations in the high frequency limit. As long as the overall lens dimensions and surface radius of curvature at any point are much larger than the wavelength, the wave propagation inside a homogeneous isotropic lens may be conveniently modelled in terms of elementary ray tubes [92, 156]. The electric field in the high frequency limit can be written as:

$$\vec{E}(\vec{r}) = \vec{e}(\vec{r})e^{-jk_0 n\hat{s}\cdot\vec{r}} = \vec{e}(\vec{r})e^{-jk_0 S(\vec{r})} \tag{A.1}$$

where $\vec{e}(\vec{r})$ is a function describing the electric field, $\hat{s}$ is a unit vector that points along the direction of propagation, $\vec{r}$ is the observation unit vector, k_0 is the free space wave number, n is refractive index, and $S(\vec{r}) = n\hat{s}\cdot\vec{r}$ is the wavefront which is perpendicular to the light ray. The reflection and transmission at an interface are made according to Snell's laws and the ray amplitude is affected by Fresnel coefficients and a divergence factor [176].

A high-level flowchart illustrating the GOanalysis steps is shown in Fig. A.1. The GOanalysis involves the following steps:

- **Step 1: Feed-Lens Surface: Propagation in Homogeneous medium.** Each ray emanated from the feed travels in free space before it impinges upon the lens boundary. The propagation is governed by the laws of geometrical optics in homogeneous
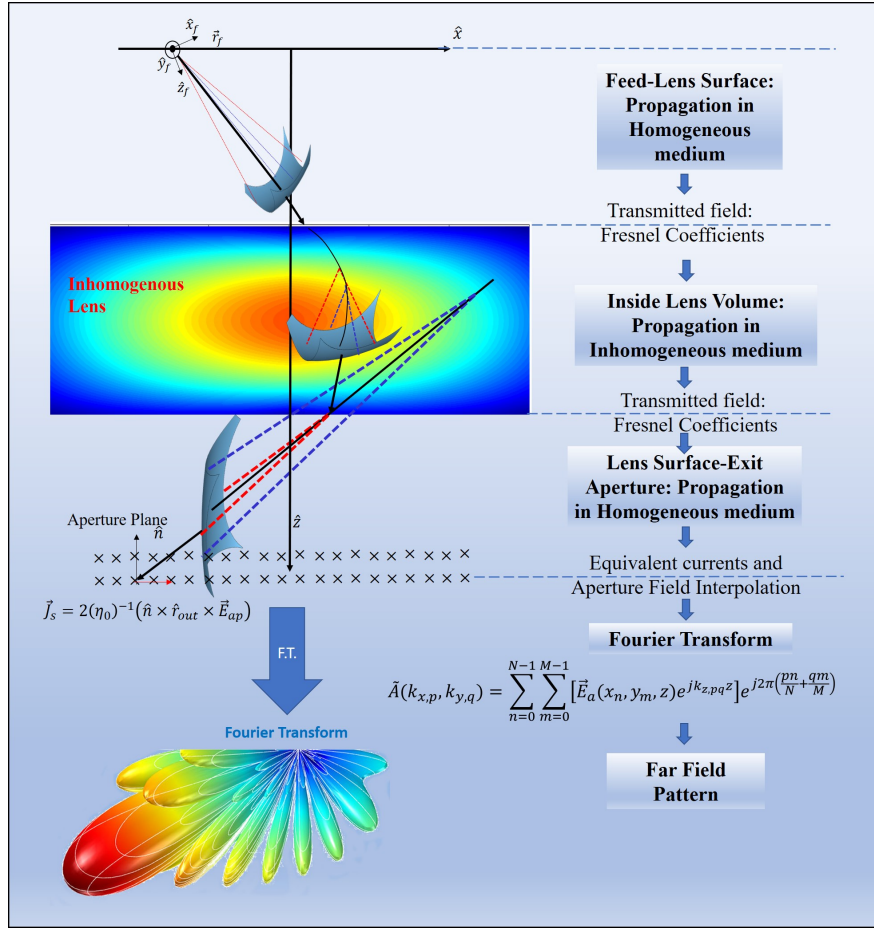
Figure A.1 GO Methodology.

media [92, 177]. The ray travels in a straight path which is described by:

$$\vec{r}(t) = \vec{r_0} + s\vec{r_1} \tag{A.2}$$

where $\vec{r_0}$ points to the start of the straight ray and $\vec{r_1}$ is a vector in the direction of the straight ray. The phase of the field is:

$$\text{phase} = k_0 n |\vec{r}| \tag{A.3}$$

The electric field amplitude can be calculated by:

$$\left(\frac{\vec{e}}{\mu}\right)_B = \left(\frac{\vec{e}}{\mu}\right)_A \sqrt{\frac{R_1(A)}{R_1(A) + B}} \sqrt{\frac{R_2(A)}{R_2(A) + B}} \tag{A.4}$$

119

where $R(s)$ is the radius of curvature of the wavefront surface and the wave propagates from point A to point B. The polarization is unaltered along the ray ($\partial \hat{e}/\partial s = 0$).

- **Step 2: Transmitted field inside lens.** Each ray that reaches the lens boundary refracts and the angle or refraction is found using Snell's law:

$$\frac{\sin \theta_t}{\sin \theta_i} = \frac{n_1}{n_2} \tag{A.5}$$

where θ_i is the angle of incidence, θ_t the the angle of refraction, $n_1 = 1$ is the refractive index of air and n_2 is the refractive index of the lens at the boundary. The incident field is multiplied by the Fresnel transmission coefficients to obtain the transmitted field:

$$\vec{E}_{\text{trans}} = T_\perp \left(\vec{E}_{\text{inc}} \hat{a}_\perp^i \right) \hat{a}_\perp^t + T_\parallel \left(\vec{E}_{\text{inc}} \hat{a}_\parallel^i \right) \hat{a}_\parallel^t \tag{A.6}$$

$$T_\parallel = \frac{2\eta_2 \cos \theta_i}{\eta_1 \cos \theta_i + \eta_2 \cos \theta_t} \tag{A.7}$$

$$T_\perp = \frac{2\eta_2 \cos \theta_i}{\eta_2 \cos \theta_i + \eta_1 \cos \theta_t} \tag{A.8}$$

where η_1, η_2 is the impedance of free space and medium at the lens boundary, $\hat{a}_\perp^i$, $\hat{a}_\parallel^i$, $\hat{a}_\perp^t$, $\hat{a}_\parallel^t$ are unit vectors parallel and perpendicular to the plane of incidence, and $T_\parallel$, $T_\perp$ are Fresnel transmission coefficients for parallel and perpendicular polarization.

- **Step 3: Propagation inside lens volume.** The transmitted wave is now guided through the inhomogeneous medium of the lens. The refractive index now varies spatially and the ray path is no longer a straight line. The propagation is governed by the laws of geometrical optics in inhomogeneous media [20, 121, 178–180]. The ray trajectory is found by solving the Light-Ray equation:

$$\frac{d}{ds} \left(n \frac{d\vec{r}}{ds} \right) = \nabla n \tag{A.9}$$

The phase is found by:

$$\text{phase} = k_0 \left(S(B) - S(A) \right) = k_0 \int_A^B nds \qquad (\text{A.10})$$

where $\left(S(B) - S(A) \right) = \int_A^B nds$ is the optical path length. The amplitude and polarization of the electric field along the ray path is found by the following equations:

$$\left(\frac{\vec{e}}{\mu} \right)_B = \left(\frac{\vec{e}}{\mu} \right)_A \sqrt{\frac{n(A)}{n(B)}} e^{-\frac{1}{2} \int_A^B \left(\frac{1}{R_1(s)} + \frac{1}{R_2(s)} \right) ds} \qquad (\text{A.11})$$

$$\frac{\partial \hat{e}}{\partial s} = - \left(\hat{e} \cdot \nabla \log n \right) \hat{t} \qquad (\text{A.12})$$

where $\hat{t}$ is a unit vector that is tangent to the ray.

- **Step 4: Transmitted field outside lens.** The ray exits the inhomogeneous lens. Reflection and transmission at the lens-air interface are made according to Snell's law and ray amplitude is affected by Fresnel coefficients. The procedure is similar to step 2.

- **Step 5: Lens Surface-Exit Aperture Plane: Propagation in Homogeneous medium.** The ray that exits the lens travels in free space in straight line according to the equations that were described in step 1. The exit aperture plane is chosen to be a quarter wavelength far from the lens physical aperture.

- **Step 6: Equivalent currents and Aperture Field Interpolation.** The launched rays are predetermined to be distributed uniformly in ρ direction and have a constant separation in each ring of a polar ring, with more samples in outer than inner rings. Steps 1-5 are repeated for each ray and the electric field $\vec{E}_{\text{ap}}$ in the aperture plane is calculated. Each calculated electric field is characterized by the amplitude, phase, and direction of propagation described by the unit vector $\hat{r}_{\text{out}}$. In view of the equivalence theorem and image theory, the equivalent currents are formed in the exit aperture plane:

$$\vec{J}_{\text{ap}} = \frac{2}{\eta_0} \hat{z} \times \hat{r}_{\text{out}} \times \vec{E}_{\text{ap}} \qquad (\text{A.13})$$

Additional aperture fields from direct rays from the feed to the aperture plane that do not travel through the lens are also calculated to capture enough field in the aperture plane and satisfy the equivalence principle. The equivalent currents from direct and spillover rays are interpolated in a rectilinear grid using Delaunay Triangulation Interpolation Scheme [181] in preparation for the Fast Fourier Transform algorithm. Interpolated currents are denoted by $\vec{J}_{\text{ap,int}}$.

- **Step 6: Fourier Transform and Far Field Pattern.** The plane wave spectrum is calculated from the interpolated equivalent current using the Fast Fourier Transform algorithm based on the following equation:

$$\vec{A}\left(k_{x,p}, k_{y,q}\right) \sum_{n=0}^{N-1} \sum_{m=0}^{M-2} \vec{J}_{\text{ap,int}}(x_n, y_m) e^{j2\pi\left(\frac{pn}{N}\frac{qm}{M}\right)} \tag{A.14}$$

where $x_n = n\Delta x$, $y_m = m\Delta y$ are the discrete coordinates of the interpolated rectilinear aperture current samples, and $k_{x,p} = p\Delta k_x = p\frac{2\pi}{N\Delta x}$, $k_{y,q} = q\Delta k_y = q\frac{2\pi}{M\Delta y}$ are discrete samples in the transformed space. The normalized far field pattern is calculated from the plane wave spectrum function:

$$\vec{E}(\theta, \phi) \left[\hat{\theta}\left(A_x \cos\phi + A_y \sin\phi\right) - \hat{\phi}\cos\theta\left(A_x \sin\phi - A_y \cos\phi\right)\right] \tag{A.15}$$

APPENDIX B

"Rotation-Phase" Property Enabling the Transmitarray CP Unit Cell Design

Recently, a property associated with CP wave scattering has drawn attention for CP reflectarray applications [182]: The CP wave reflected by a rotated object will gain a phase shift which is proportional only to the rotation angle of the object and is frequency-independent, as shown in Fig. B.1. This property renders more flexibility to the design of CP unit cells, since the desired unit cell transmission phase can be easily controlled by element rotation, and one can focus dominantly on the optimization of transmission magnitude. The "S-ring" transmitarray unit cell presented in section 5.3.1 utilized this property to provide the CP phase compensation by proper rotation of the element. This appendix provides an overview of the foundations and the derivations of the "Rotation-Phase" property enabling the transmitarray unit cell design in chapter 5.

For a CP plane wave traveling in -z direction that impinges upon an object lying in x-y plane, the expressions of the incident CP waves are (the amplitude factor is omitted for brevity of derivations):

$$\vec{E}_R^i = \hat{x} + j\hat{y} \tag{B.1}$$

$$\vec{E}_L^i = \hat{x} - j\hat{y} \tag{B.2}$$

where the subscripts "R" and "L" correspond to RHCP and LHCP incidence, respectively.

(a) RHCP Incident Wave.   (b) LHCP Incident Wave.
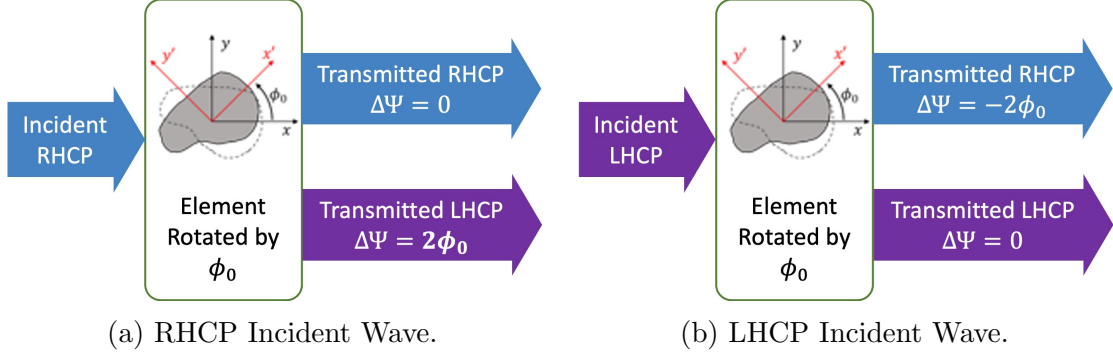
Figure B.1 "Rotation-Phase" property enabling the CP transmitarray unit cell.

The transmitted waves due to RHCP and LHCP incidence can be expressed as:

$$\vec{E}_R^t = A_t \hat{x} + j B_t \hat{y} \tag{B.3}$$

$$\vec{E}_L^t = C_t \hat{x} + j D_t \hat{y} \tag{B.4}$$

where $\vec{E}_R^t$ and $\vec{E}_L^t$ are the transmitted fields due to RHCP and LHCP excitations; the coefficients A_t, B_t and C_t, and D_t are complex scalars that take into account all the factors in this scattering problem (e.g., object geometry, material, frequency). First we consider RHCP plane wave incidence. The corresponding transmitted wave in (B.3) and can be rearranged as:

$$\vec{E}_R^t = \frac{1}{2}(A_t + B_t)(\hat{x} + j\hat{y}) + \frac{1}{2}(A_t - B_t)(\hat{x} - j\hat{y}) \tag{B.5}$$

which decomposes the transmitted wave into RHCP and LHCP components. If the object is rotated about the origin of the coordinate by an angle of ϕ_0 (as illustrated in Fig. B.1), the primed coordinate (red) follows the rotation of the object and the new axes form an angle of ϕ_0 with the global (unprimed) axes. We repeat the previous procedures in the new coordinates and illuminate the rotated object with a RHCP wave defined in primed coordinate ($\vec{E}_R^{i'} = \hat{x}' + j\hat{y}'$). For the latter case, the transmitted wave is expressed as:

$$\vec{E}_R^{t'} = \frac{1}{2}(A_t + B_t)(\hat{x}' + j\hat{y}') + \frac{1}{2}(A_t - B_t)(\hat{x}' - j\hat{y}') \tag{B.6}$$

Note that the coefficients A_t and B_t are the same as in (B.5) since the new incident wave seen by the rotated object is identical to that before rotation. We are interested in the transmitted field from the rotated object when it is excited by the original RHCP wave $\vec{E}_R^i$. Using the equation that relate theCP components defined in the original coordinate system and those in the rotated coordinate system:

$$\hat{x} - j\hat{y} = (\cos\phi_0\hat{x}' - \sin\phi_0\hat{y}') - j(\sin\phi_0\hat{x}' + \cos\phi_0\hat{y}') = e^{-j\phi_0}(\hat{x}' - j\hat{y}') \qquad (B.7)$$

$$\hat{x} + j\hat{y} = (\cos\phi_0\hat{x}' - \sin\phi_0\hat{y}') + j(\sin\phi_0\hat{x}' + \cos\phi_0\hat{y}') = e^{+j\phi_0}(\hat{x}' + j\hat{y}') \qquad (B.8)$$

one can rewrite (B.6) as:

$$\vec{E}_R^{t'} = \frac{1}{2}e^{-j\phi_0}(A_t + B_t)(\hat{x} + j\hat{y}) + \frac{1}{2}e^{+j\phi_0}(A_t - B_t)(\hat{x} - j\hat{y}) \qquad (B.9)$$

Also note that $\vec{E}_R^i = e^{j\phi_0}\vec{E}_R^{i'}$, i.e. the field from the two excitations are related by a phase constant $e^{j\phi_0}$. Therefore, when $\vec{E}_R^i$ is illuminating the rotated object, the transmitted field will carry this phase constant, which can be obtained by multiplying (B.9) by $e^{j\phi_0}$ as follows:

$$\vec{E}_R^t = \frac{1}{2}(A_t + B_t)(\hat{x} + j\hat{y}) + \frac{1}{2}e^{+j2\phi_0}(A_t - B_t)(\hat{x} - j\hat{y}) \qquad (B.10)$$

(B.10) suggests that for an object under RHCP plane wave excitation, the rotation of the object by ϕ_0 will result in a phase shift of $2\phi_0$ in its transmitted LCHP component; whereas the transmitted RHCP component will not experience any phase shift. Following similar procedures, one could also derive the expression of reflected wave under LHCP plane wave excitation:

$$\vec{E}_L^t = \frac{1}{2}e^{-j2\phi_0}(A_t + B_t)(\hat{x} + j\hat{y}) + \frac{1}{2}(A_t - B_t)(\hat{x} - j\hat{y}) \qquad (B.11)$$

This means that when the object is rotated by ϕ_0, a phase shift of $-2\phi_0$ will be introduced to the transmitted RHCP component. Note that the phase shift is only introduced to the same-handed polarized component in reflected field.

REFERENCES

[1] J. Thornton and K.-C. Huang, *Modern lens antennas for communications engineering*, 1st ed. John Wiley & Sons, 2013, vol. 39.

[2] C. A. Fernandes, "Shaped dielectric lenses for wireless millimeter-wave communications," *IEEE Antennas and Propagation Magazine*, vol. 41, no. 5, pp. 141–150, 1999.

[3] N. Pohl and M. Gerding, "A dielectric lens-based antenna concept for high-precision industrial radar measurements at 24GHz," in *2012 9th European Radar Conference*. IEEE, 2012, pp. 405–408.

[4] A. Artemenko, A. Maltsev, A. Mozharovskiy, A. Sevastyanov, V. Ssorin, and R. Maslennikov, "Millimeter-wave electronically steerable integrated lens antennas for WLAN/WPAN applications," *IEEE Transactions on Antennas and Propagation*, vol. 61, no. 4, pp. 1665–1671, 2012.

[5] J. S. Silva, M. Garcia-Vigueras, T. Debogović, J. R. Costa, C. A. Fernandes, and J. R. Mosig, "Stereolithography-based antennas for satellite communications in Ka-band," *Proceedings of the IEEE*, vol. 105, no. 4, pp. 655–667, 2017.

[6] J. R. Costa, E. B. Lima, and C. A. Fernandes, "Compact beam-steerable lens antenna for 60-GHz wireless communications," *IEEE Transactions on Antennas and Propagation*, vol. 57, no. 10, pp. 2926–2933, 2009.

[7] J. Costa, M. Silveirinha, and C. Fernandes, "Design and analysis of double-shell axial-symmetric integrated lens antennas for space applications," in *Proc. 28th ESA Antenna Workshop on Space Antenna Systems and Technologies*, vol. 2, 2005, pp. 865–872.

[8] B. Schoenlinner, X. Wu, J. P. Ebling, G. V. Eleftheriades, and G. M. Rebeiz, "Wide-scan spherical-lens antennas for automotive radars," *IEEE Transactions on Microwave Theory and Techniques*, vol. 50, no. 9, pp. 2166–2175, 2002.

[9] R. K. Luneburg, *Mathematical theory of optics*. Univ of California Press, 1964.

[10] H. Xin and M. Liang, "3-D-printed microwave and THz devices using polymer jetting techniques," *Proceedings of the IEEE*, vol. 105, no. 4, pp. 737–755, 2017.

[11] M. Liang, W.-R. Ng, K. Chang, K. Gbele, M. E. Gehm, and H. Xin, "A 3-D Luneburg lens antenna fabricated by polymer jetting rapid prototyping," *IEEE Transactions on Antennas and Propagation*, vol. 62, no. 4, pp. 1799–1807, 2014.

[12] H. F. Ma, B. G. Cai, T. X. Zhang, Y. Yang, W. X. Jiang, and T. J. Cui, "Three-dimensional gradient-index materials and their applications in microwave lens antennas," *IEEE Transactions on Antennas and Propagation*, vol. 61, no. 5, pp. 2561–2569, 2013.

[13] J. Eaton, "On spherically symmetric lenses," *Transactions of the IRE Professional Group on Antennas and Propagation*, pp. 66–71, 1952.

[14] A. Gutman, "Modified luneberg lens," *Journal of Applied Physics*, vol. 25, no. 7, pp. 855–859, 1954.

[15] G. Peeler, K. Kelleher, and H. Coleman, "Virtual source Luneberg lenses," *Transactions of the IRE Professional Group on Antennas and Propagation*, vol. 2, no. 3, pp. 94–99, 1954.

[16] A. Kay, "Spherically symmetric lenses," *IRE Transactions on Antennas and Propagation*, vol. 7, no. 1, pp. 32–38, 1959.

[17] S. Morgan, "Generalizations of spherically symmetric lenses," *IRE Transactions on Antennas and Propagation*, vol. 7, no. 4, pp. 342–345, 1959.

[18] H. Mosallaei and Y. Rahmat-Samii, "Nonuniform Luneburg and two-shell lens antennas: Radiation characteristics and design optimization," *IEEE Transactions on Antennas and Propagation*, vol. 49, no. 1, pp. 60–69, 2001.

[19] G. Du, M. Liang, R. A. Sabory-Garcia, C. Liu, and H. Xin, "3-D printing implementation of an X-band Eaton lens for beam deflection," *IEEE Antennas and Wireless Propagation Letters*, vol. 15, pp. 1487–1490, 2016.

[20] J. Budhu and Y. Rahmat-Samii, "A novel and systematic approach to inhomogeneous dielectric lens design based on curved ray geometrical optics and particle swarm optimization," *IEEE Transactions on Antennas and Propagation*, vol. 67, no. 6, pp. 3657–3669, 2019.

[21] A. Papathanasopoulos, J. Budhu, Y. Rahmat-Samii, R. E. Hodges, and D. F. Ruffatto, "3-D-printed shaped and material-optimized lenses for next-generation spaceborne wind scatterometer weather radars," *IEEE Transactions on Antennas and Propagation*, vol. 70, no. 5, pp. 3163–3172, 2022.

[22] J. Budhu and Y. Rahmat-Samii, "3D-printed inhomogeneous dielectric lens antenna diagnostics: A diagnostic tool for assessing lenses misprinted due to fabrication tolerances," *IEEE Antennas and Propagation Magazine*, 2019.

[23] J. Budhu, Y. Rahmat-Samii, R. E. Hodges, D. C. Hofmann, D. F. Ruffatto, and K. C. Carpenter, "Three-dimensionally printed, shaped, engineered material inhomogeneous lens antennas for next-generation spaceborne weather radar systems," *IEEE Antennas and Wireless Propagation Letters*, vol. 17, no. 11, pp. 2080–2084, 2018.

[24] Q.-W. Lin and H. Wong, "A low-profile and wideband lens antenna based on high-refractive-index metasurface," *IEEE Transactions on Antennas and Propagation*, vol. 66, no. 11, pp. 5764–5772, 2018.

[25] A. Papathanasopoulos, Y. Rahmat-Samii, N. Garcia, and J. D. Chisum, "A novel collapsible flat-layered metamaterial gradient-refractive-index (GRIN) lens antenna," *IEEE Transactions on Antennas and Propagation*, pp. 1–1, 2019.

[26] X. Chen, H. Feng Ma, X. Ying Zou, W. Xiang Jiang, and T. Jun Cui, "Three-dimensional broadband and high-directivity lens antenna made of metamaterials," *Journal of Applied Physics*, vol. 110, no. 4, p. 044904, 2011.

[27] M. Li, M. A. Al-Joumayly, and N. Behdad, "Broadband true-time-delay microwave lenses based on miniaturized element frequency selective surfaces," *IEEE Transactions on Antennas and Propagation*, vol. 61, no. 3, pp. 1166–1179, 2012.

[28] C. Pfeiffer and A. Grbic, "Millimeter-wave transmitarrays for wavefront and polarization control," *IEEE Transactions on Microwave Theory and Techniques*, vol. 61, no. 12, pp. 4407–4417, 2013.

[29] ——, "Planar lens antennas of subwavelength thickness: Collimating leaky-waves with metasurfaces," *IEEE Transactions on Antennas and Propagation*, vol. 63, no. 7, pp. 3248–3253, 2015.

[30] Y. Rahmat-Samii, "Reflector antennas," in *Antenna Handbook: Theory, Applications, and Design*, Y. T. Lo and S. W. Lee, Eds. Boston, MA: Springer US, 1988, pp. 949–1072.

[31] Q. Luo, S. Gao, M. Sobhy, and X. Yang, "Wideband transmitarray with reduced profile," *IEEE Antennas and Wireless Propagation Letters*, vol. 17, no. 3, pp. 450–453, 2018.

[32] K. T. Pham, A. Clemente, E. Fourn, F. Diaby, L. Dussopt, and R. Sauleau, "Low-cost metal-only transmitarray antennas at Ka-band," *IEEE Antennas and Wireless Propagation Letters*, vol. 18, no. 6, pp. 1243–1247, 2019.

[33] D. G. Long and J. M. Mendel, "Identifiability in wind estimation from scatterometer measurements," *IEEE Transactions on Geoscience and Remote Sensing*, vol. 29, no. 2, pp. 268–276, 1991.

[34] F. M. Naderi, M. H. Freilich, and D. Long, "Spaceborne radar measurement of wind velocity over the ocean-an overview of the NSCAT scatterometer system," *Proceedings of the IEEE*, vol. 79, no. 6, pp. 850–866, 1991.

[35] G. Wang, X. Dong, D. Zhu, and Q. Bao, "Azimuth high resolution for a conically scanned pencil-beam scatterometer using rotating azimuth Doppler discrimination," *IEEE Journal of Selected Topics in Applied Earth Observations and Remote Sensing*, vol. 10, no. 2, pp. 572–579, 2016.

[36] J. J. Qu, W. Gao, M. Kafatos, R. E. Murphy, and V. V. Salomonson, *Earth Science Satellite Remote Sensing: Vol. 1: Science and Instruments*. Springer, 2006.

[37] Y.-X. Wang, M. Wei, Z.-h. Wang, S. Zhang, and L.-X. Liu, "Novel scanning strategy for future spaceborne Doppler weather radar with application to tropical cyclones," *IEEE Journal of Selected Topics in Applied Earth Observations and Remote Sensing*, vol. 10, no. 6, pp. 2685–2693, 2017.

[38] D. B. Kunkee, G. A. Poe, D. J. Boucher, S. D. Swadley, Y. Hong, J. E. Wessel, and E. A. Uliana, "Design and evaluation of the first special sensor microwave imager/sounder," *IEEE Transactions on Geoscience and Remote sensing*, vol. 46, no. 4, pp. 863–883, 2008.

[39] X. Lu, L. Wu, Z. L. Xiao, and J. Z. Xu, "Ranging technique based on conically scanned single pixel millimeter wave radiometer," in *International Journal of Engineering Research in Africa*, vol. 12. Trans Tech Publ, 2014, pp. 43–52.

[40] E. Nova, J. Abril, J. Romeu, A. Broquetas, F. Torres, and L. Jofre, "Characterization of a 94 GHz radiometric imager with mechanical beam-scanning," in *2011 IEEE MTT-S International Microwave Workshop Series on Millimeter Wave Integration Technologies*. IEEE, 2011, pp. 164–167.

[41] R. Appleby, R. N. Anderton, S. Price, N. A. Salmon, G. N. Sinclair, J. R. Borrill, P. R. Coward, V. P. Papakosta, A. H. Lettington, and D. A. Robertson, "Compact real-time (video rate) passive millimeter-wave imager," in *Passive Millimeter-Wave Imaging Technology III*, vol. 3703. International Society for Optics and Photonics, 1999, pp. 13–19.

[42] R. N. Anderton, R. Appleby, P. R. Coward, P. J. Kent, S. Price, G. N. Sinclair, and M. R. Wasley, "Security scanning at 35 GHz," in *Passive Millimeter-Wave Imaging Technology V*, vol. 4373. International Society for Optics and Photonics, 2001, pp. 16–23.

[43] R. Appleby, R. N. Anderton, S. Price, N. A. Salmon, G. N. Sinclair, P. R. Coward, A. R. Barnes, P. Munday, M. Moore, A. H. Lettington *et al.*, "Mechanically scanned real-time passive millimeter-wave imaging at 94 GHz," in *Passive millimeter-wave imaging technology VI and Radar sensor technology VII*, vol. 5077. International Society for Optics and Photonics, 2003, pp. 1–6.

[44] P. R. Coward, R. N. Anderton, and S. Price, "Receiver array design for conically scanned millimetre-wave imagers," in *Passive Millimetre-Wave and Terahertz Imaging and Technology*, vol. 5619. International Society for Optics and Photonics, 2004, pp. 108–116.

[45] M. Vicente-Lozano, G. Franceschetti, F. J. Ares-Pena, and E. Moreno-Piquero, "Analysis and synthesis of a printed array for satellite communication with moving vehicles," *IEEE Transactions on Antennas and propagation*, vol. 50, no. 11, pp. 1555–1559, 2002.

[46] A. Papathanasopoulos and Y. Rahmat-Samii, "Fundamentals of orbital angular momentum beams: Concepts, antenna analogies, and applications," Z. H. Jiang and D. Werner, Eds. Wiley Online Library, 2021, pp. 1–32.

[47] D. G. Bodnar, B. K. Rainer, and Y. Rahmat-Samii, "A novel array antenna for MSAT applications," *IEEE Transactions on Vehicular Technology*, vol. 38, no. 2, pp. 86–94, 1989.

[48] W. Lin, H. Wong, and R. W. Ziolkowski, "Wideband pattern-reconfigurable antenna with switchable broadside and conical beams," *IEEE Antennas and wireless propagation letters*, vol. 16, pp. 2638–2641, 2017.

[49] A. F. Morabito, L. Di Donato, and T. Isernia, "Orbital angular momentum antennas: Understanding actual possibilities through the aperture antennas theory," *IEEE Antennas and Propagation Magazine*, vol. 60, no. 2, pp. 59–67, 2018.

[50] M. Veysi, C. Guclu, F. Capolino, and Y. Rahmat-Samii, "Revisiting orbital angular momentum beams: Fundamentals, reflectarray generation, and novel antenna applications," *IEEE Antennas and Propagation Magazine*, vol. 60, no. 2, pp. 68–81, 2018.

[51] W. L. Stutzman and G. A. Thiele, *Antenna theory and design*, 3rd ed. John Wiley & Sons, 2012.

[52] "Today's hurricanes kill way fewer americans, and NOAA's satellites are the reason why," https://www.popsci.com/noaa-satellites-storm-predictions, accessed: 03-29-2022.

[53] "QuikSCAT - eoPortal directory - satellite missions," https://directory.eoportal.org/web/eoportal/satellite-missions/q/quikscat., accessed: 03-29-2022.

[54] "Scatterometry - overview," https://www.coaps.fsu.edu/scatterometry/about/overview.php., accessed: 03-29-2022.

[55] D. B. Chelton, M. H. Freilich, J. M. Sienkiewicz, and J. M. Von Ahn, "On the use of QuikSCAT scatterometer measurements of surface winds for marine weather prediction," *Monthly Weather Review*, vol. 134, no. 8, pp. 2055–2071, 2006.

[56] P. S. ChaNg, Z. JElENak, J. M. SIENkIEWICZ, R. Knabb, M. J. Brennan, D. G. Long, and M. Freeberg, "Operational use and impact of satellite remotely sensed ocean surface vector winds in the marine warning and forecasting environment," *Oceanography*, vol. 22, no. 2, pp. 194–207, 2009.

[57] R. Singh, P. Kumar, and P. K. Pal, "Assimilation of Oceansat-2-scatterometer-derived surface winds in the weather research and forecasting model," *IEEE Transactions on Geoscience and Remote Sensing*, vol. 50, no. 4, pp. 1015–1021, 2011.

[58] R. Atlas, R. Hoffman, S. Leidner, J. Sienkiewicz, T.-W. Yu, S. Bloom, E. Brin, J. Ardizzone, J. Terry, D. Bungato *et al.*, "The effects of marine winds from scatterometer data on weather analysis and forecasting," *Bulletin of the American Meteorological Society*, vol. 82, no. 9, pp. 1965–1990, 2001.

[59] S. B. Capps and C. S. Zender, "Estimated global ocean wind power potential from QuikSCAT observations, accounting for turbine characteristics and siting," *Journal of Geophysical Research: Atmospheres*, vol. 115, no. D9, 2010.

[60] D. Karamanis, C. Tsabaris, K. Stamoulis, and D. Georgopoulos, "Wind energy resources in the Ionian Sea," *Renewable Energy*, vol. 36, no. 2, pp. 815–822, 2011.

[61] K. T. Chan and J. C. Chan, "Size and strength of tropical cyclones as inferred from QuikSCAT data," *Monthly weather review*, vol. 140, no. 3, pp. 811–824, 2012.

[62] R. Singh, P. Pal, C. Kishtawal, and P. Joshi, "The impact of variational assimilation of SSM/I and QuikSCAT satellite observations on the numerical simulation of Indian ocean tropical cyclones," *Weather and Forecasting*, vol. 23, no. 3, pp. 460–476, 2008.

[63] S. Frolking, T. Milliman, K. McDonald, J. Kimball, M. Zhao, and M. Fahnestock, "Evaluation of the SeaWinds scatterometer for regional monitoring of vegetation phenology," *Journal of Geophysical Research: Atmospheres*, vol. 111, no. D17, 2006.

[64] J. Friesen, S. C. Steele-Dunne, and N. van de Giesen, "Diurnal differences in global ERS scatterometer backscatter observations of the land surface," *IEEE Transactions on Geoscience and Remote Sensing*, vol. 50, no. 7, pp. 2595–2602, 2012.

[65] A. Bartsch, "Ten years of SeaWinds on QuikSCAT for snow applications," *Remote Sensing*, vol. 2, no. 4, pp. 1142–1156, 2010.

[66] P.-L. Frison, L. Jarlan, and E. Mougin, "Using satellite scatterometers to monitor continental surfaces," in *Land Surface Remote Sensing in Continental Hydrology*. Elsevier, 2016, pp. 79–113.

[67] X. Fettweis, M. Tedesco, M. van den Broeke, and J. Ettema, "Melting trends over the Greenland ice sheet (1958–2009) from spaceborne microwave data and regional climate models," *The Cryosphere*, vol. 5, no. 2, pp. 359–375, 2011.

[68] "Scatterometry," https://winds.jpl.nasa.gov/aboutscatterometry/history/., accessed: 03-29-2022.

[69] R. Atlas, S. Bloom, R. Hoffman, E. Brin, J. Ardizzone, J. Terry, D. Bungato, and J. Jusem, "Geophysical validation of NSCAT winds using atmospheric data and analyses," *Journal of Geophysical Research: Oceans*, vol. 104, no. C5, pp. 11405–11424, 1999.

[70] J. Pan, X.-H. Yan, Q. Zheng, W. T. Liu, and V. V. Klemas, "Interpretation of scatterometer ocean surface wind vector EOFs over the Northwestern Pacific," *Remote Sensing of Environment*, vol. 84, no. 1, pp. 53–68, 2003.

[71] M. W. Spencer, C. Wu, and D. G. Long, "Improved resolution backscatter measurements with the SeaWinds pencil-beam scatterometer," *IEEE Transactions on Geoscience and remote sensing*, vol. 38, no. 1, pp. 89–104, 2000.

[72] D. G. Long and P. J. Hardin, "Vegetation studies of the Amazon basin using enhanced resolution Seasat scatterometer data," *IEEE Transactions on Geoscience and Remote Sensing*, vol. 32, no. 2, pp. 449–460, 1994.

[73] D. G. Long, M. R. Drinkwater, B. Holt, S. Saatchi, and C. Bertoia, "Global ice and land climate studies using scatterometer image data," *Eos, Transactions American Geophysical Union*, vol. 82, no. 43, pp. 503–503, 2001.

[74] D. G. Long and M. R. Drinkwater, "Cryosphere applications of NSCAT data," *IEEE transactions on geoscience and remote sensing*, vol. 37, no. 3, pp. 1671–1684, 1999.

[75] D. S. Early, *A study of the scatterometer image reconstruction algorithm and its applications to polar ice studies*. Brigham Young University. Department of Electrical and Computer Engineering, 1998.

[76] "SeaSat - eoPortal directory - satellite missions," https://directory.eoportal.org/web/eoportal/satellite-missions/s/seasat., accessed: 03-29-2022.

[77] F. Wentz, S. Peteherych, and L. Thomas, "A model function for ocean radar cross sections at 14.6 GHz," *Journal of Geophysical Research: Oceans*, vol. 89, no. C3, pp. 3689–3704, 1984.

[78] F. J. Wentz, L. Mattox, and S. Peteherych, "New algorithms for microwave measurements of ocean winds: Applications to Seasat and the special sensor microwave imager," *Journal of Geophysical Research: Oceans*, vol. 91, no. C2, pp. 2289–2307, 1986.

[79] "Missions," https://winds.jpl.nasa.gov/missions/, accessed: 03-30-2022.

[80] "QuikSCAT — PO.DAAC," https://podaac.jpl.nasa.gov/QuikSCAT, accessed: 03-30-2022.

[81] J. E. Graf, W.-y. Tsi, and L. Jones, "Overview of QuikSCAT mission-a quick deployment of a high resolution, wide swath scanning scatterometer for ocean wind measurement," in *Proceedings IEEE Southeastcon'98'Engineering for a New Era'*. IEEE, 1998, pp. 314–317.

[82] S. Clark, "Spaceflight Now — Breaking News — Wind sensor failure ends long-lived satellite mission," https://spaceflightnow.com/news/n0911/24quikscat/, accessed: 03-30-2022.

[83] S. L. Durden and D. Perkovic-Martin, "The RapidScat ocean winds scatterometer: A radar system engineering perspective," *IEEE Geoscience and Remote Sensing Magazine*, vol. 5, no. 3, pp. 36–43, 2017.

[84] A. C. Paget, D. G. Long, and N. M. Madsen, "RapidScat diurnal cycles over land," *IEEE Transactions on Geoscience and Remote Sensing*, vol. 54, no. 6, pp. 3336–3344, 2016.

[85] "Missions — International Space Station Rapid Scatterometer," https://www.jpl.nasa.gov/missions/international-space-station-rapid-scatterometer-iss-rapidscat/, accessed: 11-23-2020.

[86] D. A. Laing, "Introduction to tropical meteorology," https://ftp.comet.ucar.edu/memory-stick/tropical/textbook_2nd_edition/index.htm, 2016, accessed: 04-07-2022.

[87] Y. Li, L. Ge, M. Chen, Z. Zhang, Z. Li, and J. Wang, "Multibeam 3-D-printed Luneburg lens fed by magnetoelectric dipole antennas for millimeter-wave MIMO applications," *IEEE Transactions on Antennas and Propagation*, vol. 67, no. 5, pp. 2923–2933, 2019.

[88] C. Wang, J. Wu, and Y.-X. Guo, "A 3D-printed multibeam dual circularly polarized Luneburg lens antenna based on quasi-icosahedron models for Ka-band wireless applications," *IEEE Transactions on Antennas and Propagation*, vol. 68, no. 8, pp. 5807–5815, 2020.

[89] B. Fuchs, L. Le Coq, O. Lafond, S. Rondineau, and M. Himdi, "Design optimization of multishell Luneburg lenses," *IEEE Transactions on Antennas and Propagation*, vol. 55, no. 2, pp. 283–289, 2007.

[90] Z. Larimore, S. Jensen, A. Good, A. Lu, J. Suarez, and M. Mirotznik, "Additive manufacturing of Luneburg lens antennas using space-filling curves and fused filament fabrication," *IEEE Transactions on Antennas and Propagation*, vol. 66, no. 6, pp. 2818–2827, 2018.

[91] K. Gbele, M. Liang, W.-R. Ng, M. E. Gehm, and H. Xin, "Millimeter wave Luneburg lens antenna fabricated by polymer jetting rapid prototyping," in *2014 39th International Conference on Infrared, Millimeter, and Terahertz waves (IRMMW-THz)*. IEEE, 2014, pp. 1–1.

[92] G. A. Deschamps, "Ray techniques in electromagnetics," *Proceedings of the IEEE*, vol. 60, no. 9, pp. 1022–1035, 1972.

[93] J. Robinson and Y. Rahmat-Samii, "Particle swarm optimization in electromagnetics," *IEEE Transactions on Antennas and Propagation*, vol. 52, no. 2, pp. 397–407, 2004.

[94] A. Papathanasopoulos and Y. Rahmat-Samii, "Flat meta-lens antenna synthesis via geometrical optics and particle swarm optimization," in *2020 IEEE International Symposium on Antennas and Propagation and CNC/USNC-URSI Radio Science Meeting*. IEEE, 2020, pp. 857–858.

[95] ——, "Multi-layered flat metamaterial lenses: Design, prototyping and measurements," in *2020 Antenna Measurement Techniques Association Symposium (AMTA)*. IEEE, 2020, pp. 1–6.

[96] Y. Rahmat-Samii, J. Budhu, R. Hodges, D. Hofmann, and D. Ruffatto, "A novel 60-cm nonsherical 3-D printed voxelized lens antenna: Design, fabrication and measurement," in *2019 IEEE International Symposium on Antennas and Propagation and USNC-URSI Radio Science Meeting*. IEEE, 2019, pp. 1699–1700.

[97] "IEEE Standard for definitions of terms for antennas," *IEEE Std 145-2013 (Revision of IEEE Std 145-1993)*, pp. 1–50, 2014.

[98] "Original Prusa 3D printers directly from Josef Prusa," https://www.prusa3d.com., accessed: 05-06-2022.

[99] "IEEE Standard test procedures for antennas," *ANSI/IEEE Std 149-1979*, pp. 1–144, 1979.

[100] Q. Ma, C. B. Shi, T. Y. Chen, M. Q. Qi, Y. B. Li, and T. J. Cui, "Broadband metamaterial lens antennas with special properties by controlling both refractive-index distribution and feed directivity," *Journal of Optics*, vol. 20, no. 4, p. 045101, 2018.

[101] M. Q. Qi, W. X. Tang, H.-X. Xu, H. F. Ma, and T. J. Cui, "Tailoring radiation patterns in broadband with controllable aperture field using metamaterials," *IEEE Transactions on Antennas and Propagation*, vol. 61, no. 11, pp. 5792–5798, 2013.

[102] H. F. Ma, X. Chen, X. M. Yang, W. X. Jiang, and T. J. Cui, "Design of multibeam scanning antennas with high gains and low sidelobes using gradient-index metamaterials," *Journal of Applied Physics*, vol. 107, no. 1, p. 014902, 2010.

[103] A. Papathanasopoulos and Y. Rahmat-Samii, "A novel deployable compact lens antenna based on gradient-index metamaterials," in *2019 IEEE International Symposium on Antennas and Propagation and USNC-URSI Radio Science Meeting.* IEEE, 2019, pp. 625–626.

[104] W. E. Kock, "Metallic delay lenses," *Bell Labs Technical Journal*, vol. 27, no. 1, pp. 58–82, 1948.

[105] Q. Cheng, H. Ma, and T. Cui, "A complementary lens based on broadband metamaterials," *Journal of Electromagnetic Waves and Applications*, vol. 24, no. 1, pp. 93–101, 2010.

[106] E. Erfani, M. Niroo-Jazi, and S. Tatu, "A high-gain broadband gradient refractive index metasurface lens antenna," *IEEE Transactions on Antennas and Propagation*, vol. 64, no. 5, pp. 1968–1973, 2016.

[107] H.-X. Xu, G.-M. Wang, Z. Tao, and T. J. Cui, "High-directivity emissions with flexible beam numbers and beam directions using gradient-refractive-index fractal metamaterial," *Scientific reports*, vol. 4, p. 5744, 2014.

[108] S. M. A. M. H. Abadi and N. Behdad, "Design of wideband, fss-based multibeam antennas using the effective medium approach," *IEEE Transactions on Antennas and Propagation*, vol. 62, no. 11, pp. 5557–5564, 2014.

[109] N. Zhang, W. X. Jiang, H. F. Ma, W. X. Tang, and T. J. Cui, "Compact high-performance lens antenna based on impedance-matching gradient-index metamaterials," *IEEE Transactions on Antennas and Propagation*, vol. 67, no. 2, pp. 1323–1328, 2018.

[110] A. Papathanasopoulos and Y. Rahmat-Samii, "Multi-layered flat meta-lenses for conical beam scanning via optimization of geometrical optics," in *2021 IEEE International Symposium on Antennas and Propagation and USNC-URSI Radio Science Meeting (APS/URSI).* IEEE, 2021, pp. 105–106.

[111] H.-X. Xu, G.-M. Wang, Z. Tao, and T. Cai, "An octave-bandwidth half maxwell fish-eye lens antenna using three-dimensional gradient-index fractal metamaterials," *IEEE Transactions on Antennas and Propagation*, vol. 62, no. 9, pp. 4823–4828, 2014.

134

[112] D. R. Smith, S. Schultz, P. Markoš, and C. Soukoulis, "Determination of effective permittivity and permeability of metamaterials from reflection and transmission coefficients," *Physical Review B*, vol. 65, no. 19, p. 195104, 2002.

[113] D. Smith, D. Vier, T. Koschny, and C. Soukoulis, "Electromagnetic parameter retrieval from inhomogeneous metamaterials," *Physical review E*, vol. 71, no. 3, p. 036617, 2005.

[114] A. Papathanasopoulos and Y. Rahmat-Samii, "A systematic approach for the design of metallic delay lenses," in *2019 United States National Committee of URSI National Radio Science Meeting (USNC-URSI NRSM)*.   IEEE, 2019, pp. 1–2.

[115] M. Imbert, A. Papió, F. De Flaviis, L. Jofre, and J. Romeu, "Design and performance evaluation of a dielectric flat lens antenna for millimeter-wave applications," *IEEE Antennas and Wireless Propagation Letters*, vol. 14, pp. 342–345, 2015.

[116] M. K. T. Al-Nuaimi, W. Hong, and Y. Zhang, "Design of high-directivity compact-size conical horn lens antenna," *IEEE Antennas and Wireless Propagation Letters*, vol. 13, pp. 467–470, 2014.

[117] A. Dhouibi, S. N. Burokur, A. de Lustrac, and A. Priou, "Compact metamaterial-based substrate-integrated luneburg lens antenna," *IEEE Antennas and Wireless Propagation Letters*, vol. 11, pp. 1504–1507, 2012.

[118] H.-X. Xu, G.-M. Wang, and T. Cai, "Miniaturization of 3-D anistropic zero-refractive-index metamaterials with application to directive emissions," *IEEE Transactions on Antennas and Propagation*, vol. 62, no. 6, pp. 3141–3149, 2014.

[119] J. P. Turpin, Q. Wu, D. H. Werner, B. Martin, M. Bray, and E. Lier, "Low cost and broadband dual-polarization metamaterial lens for directivity enhancement," *IEEE Transactions on Antennas and Propagation*, vol. 60, no. 12, pp. 5717–5726, 2012.

[120] R. E. Hodges, N. Chahat, D. J. Hoppe, and J. D. Vacchione, "A deployable high-gain antenna bound for Mars: Developing a new folded-panel reflectarray for the first cubesat mission to Mars." *IEEE Antennas and Propagation Magazine*, vol. 59, no. 2, pp. 39–49, April 2017.

[121] J. Budhu, "Numerical synthesis algorithms and antenna designs for next generation spaceborne wind scatterometer and cubesat antennas," Ph.D. dissertation, UCLA, 2018.

[122] Y. Rahmat-Samii, L. I. Williams, and R. G. Yaccarino, "The UCLA bi-polar planar-near-field antenna-measurement and diagnostics range," *IEEE Antennas and Propagation Magazine*, vol. 37, no. 6, pp. 16–35, 1995.

[123] A. H. Abdelrahman, F. Yang, A. Z. Elsherbeni, and P. Nayeri, "Analysis and design of transmitarray antennas," *Synthesis Lectures on Antennas*, vol. 6, no. 1, pp. 1–175, 2017.

[124] N. Gagnon, A. Petosa, and D. A. McNamara, "Research and development on phase-shifting surfaces (PSSs)," *IEEE Antennas and Propagation Magazine*, vol. 55, no. 2, pp. 29–48, 2013.

[125] A. H. Abdelrahman, P. Nayeri, A. Z. Elsherbeni, and F. Yang, "Bandwidth improvement methods of transmitarray antennas," *IEEE Transactions on Antennas and Propagation*, vol. 63, no. 7, pp. 2946–2954, 2015.

[126] B. Rahmati and H. Hassani, "High-efficient wideband slot transmitarray antenna," *IEEE Transactions on Antennas and Propagation*, vol. 63, no. 11, pp. 5149–5155, 2015.

[127] A. H. Abdelrahman, A. Z. Elsherbeni, and F. Yang, "Transmitarray antenna design using cross-slot elements with no dielectric substrate," *IEEE Antennas and Wireless Propagation Letters*, vol. 13, pp. 177–180, 2014.

[128] G. Liu, H.-j. Wang, J.-s. Jiang, F. Xue, and M. Yi, "A high-efficiency transmitarray antenna using double split ring slot elements," *IEEE Antennas and Wireless Propagation Letters*, vol. 14, pp. 1415–1418, 2015.

[129] G. Liu, M. R. D. Kodnoeih, K. T. Pham, E. M. Cruz, D. González-Ovejero, and R. Sauleau, "A millimeter-wave multibeam transparent transmitarray antenna at Ka-band," *IEEE Antennas and Wireless Propagation Letters*, vol. 18, no. 4, pp. 631–635, 2019.

[130] J. Wang, A. Papathanasopoulos, Y. Rahmat-Samii, R. Hensleigh, Z. Xu, and X. Zheng, "Ultra-lightweight transmitarray antenna enabled by charge-programmed three-dimensional multi-material printing," in *2022 United States National Committee of URSI National Radio Science Meeting (USNC-URSI NRSM)*. IEEE, 2019, pp. 302–303.

[131] A. Papathanasopoulos and Y. Rahmat-Samii, "Low-profile transmitarray for wide-angle conical scanning: Concept, optimization and validation," in *2021 IEEE International Symposium on Antennas and Propagation and CNC/USNC-URSI Radio Science Meeting*. IEEE, 2021, pp. 1079–1080.

[132] H. Nematollahi, J.-J. Laurin, J. Page, and J. A. Encinar, "Design of broadband transmitarray unit cells with comparative study of different numbers of layers," *IEEE Transactions on Antennas and Propagation*, vol. 63, no. 4, pp. 1473–1481, 2015.

[133] X. Yi, T. Su, X. Li, B. Wu, and L. Yang, "A double-layer wideband transmitarray antenna using two degrees of freedom elements around 20 GHz," *IEEE Transactions on Antennas and Propagation*, vol. 67, no. 4, pp. 2798–2802, 2019.

[134] A. Clemente, L. Dussopt, R. Sauleau, P. Potier, and P. Pouliguen, "Focal distance reduction of transmit-array antennas using multiple feeds," *IEEE Antennas and Wireless Propagation Letters*, vol. 11, pp. 1311–1314, 2012.

[135] S. Zainud-Deen, S. M. Gaber, and K. Awadalla, "Transmitarray using perforated dielectric material for wideband applications," *Progress in Electromagnetics Research M*, vol. 24, pp. 1–13, 2012.

[136] "Home: Microwave/RF components, subsystems, and SATCOM - Narda-MITEQ," https://nardamiteq.com/., accessed: 02-04-2022.

[137] J. Bresenham, "A linear algorithm for incremental digital display of circular arcs," *Communications of the ACM*, vol. 20, no. 2, pp. 100–106, 1977.

[138] L.-Z. Song, P.-Y. Qin, S.-L. Chen, and Y. J. Guo, "An elliptical cylindrical shaped transmitarray for wide-angle multibeam applications," *IEEE Transactions on Antennas and Propagation*, vol. 69, no. 10, pp. 7023–7028, 2021.

[139] S. A. Matos, E. B. Lima, J. S. Silva, J. R. Costa, C. A. Fernandes, N. J. Fonseca, and J. R. Mosig, "High gain dual-band beam-steering transmit array for satcom terminals at Ka-band," *IEEE Transactions on Antennas and Propagation*, vol. 65, no. 7, pp. 3528–3539, 2017.

[140] L. Allen, M. W. Beijersbergen, R. Spreeuw, and J. Woerdman, "Orbital angular momentum of light and the transformation of Laguerre-Gaussian laser modes," *Physical Review A*, vol. 45, no. 11, p. 8185, 1992.

[141] A. E. Willner, Y. Ren, G. Xie, Y. Yan, L. Li, Z. Zhao, J. Wang, M. Tur, A. F. Molisch, and S. Ashrafi, "Recent advances in high-capacity free-space optical and radio-frequency communications using orbital angular momentum multiplexing," *Philosophical Transactions of the Royal Society A: Mathematical, Physical and Engineering Sciences*, vol. 375, no. 2087, p. 20150439, 2017.

[142] A. Papathanasopoulos and Y. Rahmat-Samii, "A review on orbital angular momentum (OAM) beams: Fundamental concepts, potential applications, and perspectives," in *2021 XXXVth URSI General Assembly and Scientific Symposium (URSI GASS)*. IEEE, 2021.

[143] C. Rui, Z. Hong, M. Marco, W. Xiaodong, and L. Jiandong, "Orbital angular momentum waves: Generation, detection and emerging applications," *arXiv preprint arXiv:1903.07818*, 2019.

[144] O. Edfors and A. J. Johansson, "Is orbital angular momentum (OAM) based radio communication an unexploited area?" *IEEE Transactions on Antennas and Propagation*, vol. 60, no. 2, pp. 1126–1131, 2011.

[145] M. Tamagnone, C. Craeye, and J. Perruisseau-Carrier, "Comment on 'encoding many channels on the same frequency through radio vorticity: First experimental test'," *New Journal of Physics*, vol. 14, no. 11, p. 118001, 2012.

[146] G. Xie, L. Li, Y. Ren, H. Huang, Y. Yan, N. Ahmed, Z. Zhao, M. P. Lavery, N. Ashrafi, S. Ashrafi *et al.*, "Performance metrics and design considerations for a free-space optical

orbital-angular-momentum multiplexed communication link," *Optica*, vol. 2, no. 4, pp. 357–365, 2015.

[147] J. H. Poynting, "The wave motion of a revolving shaft, and a suggestion as to the angular momentum in a beam of circularly polarised light," *Proceedings of the Royal Society of London. Series A, Containing Papers of a Mathematical and Physical Character*, vol. 82, no. 557, pp. 560–567, 1909.

[148] R. A. Beth, "Mechanical detection and measurement of the angular momentum of light," *Phys. Rev.*, vol. 50, pp. 115–125, Jul 1936.

[149] G. Gibson, J. Courtial, M. J. Padgett, M. Vasnetsov, V. Pas'ko, S. M. Barnett, and S. Franke-Arnold, "Free-space information transfer using light beams carrying orbital angular momentum," *Optics express*, vol. 12, no. 22, pp. 5448–5456, 2004.

[150] P. Z. Dashti, F. Alhassen, and H. P. Lee, "Observation of orbital angular momentum transfer between acoustic and optical vortices in optical fiber," *Physical review letters*, vol. 96, no. 4, p. 043604, 2006.

[151] B. Thidé, H. Then, J. Sjöholm, K. Palmer, J. Bergman, T. Carozzi, Y. N. Istomin, N. Ibragimov, and R. Khamitova, "Utilization of photon orbital angular momentum in the low-frequency radio domain," *Physical review letters*, vol. 99, no. 8, p. 087701, 2007.

[152] F. Tamburini, E. Mari, A. Sponselli, B. Thidé, A. Bianchini, and F. Romanato, "Encoding many channels on the same frequency through radio vorticity: first experimental test," *New Journal of Physics*, vol. 14, no. 3, p. 033001, 2012.

[153] N. Bozinovic, Y. Yue, Y. Ren, M. Tur, P. Kristensen, H. Huang, A. E. Willner, and S. Ramachandran, "Terabit-scale orbital angular momentum mode division multiplexing in fibers," *science*, vol. 340, no. 6140, pp. 1545–1548, 2013.

[154] C. A. Balanis, *Advanced Engineering Electromagnetics*, 2nd ed. John Wiley & Sons, 2012.

[155] ——, *Antenna theory: analysis and design*, 3rd ed. John wiley & sons, 2016.

[156] M. Born and E. Wolf, *Principles of optics: electromagnetic theory of propagation, interference and diffraction of light*, 7th ed. Elsevier, 2013.

[157] I. S. Gradshteyn and I. M. Ryzhik, *Table of integrals, series, and products*, 7th ed. Academic press, 2014.

[158] R. Niemiec, C. Brousseau, K. Mahdjoubi, O. Emile, and A. Ménard, "Characterization of an OAM flat-plate antenna in the millimeter frequency band," *IEEE Antennas and Wireless Propagation Letters*, vol. 13, pp. 1011–1014, 2014.

[159] E. Yao, S. Franke-Arnold, J. Courtial, S. Barnett, and M. Padgett, "Fourier relationship between angular position and optical orbital angular momentum," *Optics Express*, vol. 14, no. 20, pp. 9071–9076, 2006.

138

[160] A. Papathanasopoulos, J. Wang, and Y. Rahmat-Samii, "Understanding the far-field properties of orbital angular momentum beams through the antenna aperture field method," in *2022 United States National Committee of URSI National Radio Science Meeting (USNC-URSI NRSM)*.   IEEE, 2019, pp. 178–179.

[161] C. Tao, A. Papathanasopoulos, and T. Itoh, "Linear-to-circular polarization converter based on stacked metasurfaces with aperture coupling interlayer," in *2020 IEEE/MTT-S International Microwave Symposium (IMS)*.   IEEE, 2020, pp. 1–4.

[162] G. Turnbull, D. Robertson, G. Smith, L. Allen, and M. Padgett, "The generation of free-space Laguerre-Gaussian modes at millimetre-wave frequencies by use of a spiral phaseplate," *Optics communications*, vol. 127, no. 4-6, pp. 183–188, 1996.

[163] A. M. Yao and M. J. Padgett, "Orbital angular momentum: origins, behavior and applications," *Advances in Optics and Photonics*, vol. 3, no. 2, pp. 161–204, 2011.

[164] A. E. Willner, H. Huang, Y. Yan, Y. Ren, N. Ahmed, G. Xie, C. Bao, L. Li, Y. Cao, Z. Zhao *et al.*, "Optical communications using orbital angular momentum beams," *Advances in Optics and Photonics*, vol. 7, no. 1, pp. 66–106, 2015.

[165] M. Oldoni, F. Spinello, E. Mari, G. Parisi, C. G. Someda, F. Tamburini, F. Romanato, R. A. Ravanelli, P. Coassini, and B. Thidé, "Space-division demultiplexing in orbital-angular-momentum-based MIMO radio systems," *IEEE Transactions on Antennas and Propagation*, vol. 63, no. 10, pp. 4582–4587, 2015.

[166] X. Ge, R. Zi, X. Xiong, Q. Li, and L. Wang, "Millimeter wave communications with OAM-SM scheme for future mobile networks," *IEEE Journal on Selected Areas in Communications*, vol. 35, no. 9, pp. 2163–2177, 2017.

[167] R. L. Phillips and L. C. Andrews, "Spot size and divergence for laguerre gaussian beams of any order," *Applied optics*, vol. 22, no. 5, pp. 643–644, 1983.

[168] A. Papathanasopoulos, J. Wang, and Y. Rahmat-Samii, "Transmitarray antenna generating circularly polarized orbital angular momentum (OAM) beams: Synthesis, prototyping and measurements," in *2021 Antenna Measurement Techniques Association Symposium (AMTA)*.   IEEE, 2021, pp. 1–4.

[169] R. H. Phillion and M. Okoniewski, "Lenses for circular polarization using planar arrays of rotated passive elements," *IEEE Transactions on Antennas and Propagation*, vol. 59, no. 4, pp. 1217–1227, 2011.

[170] L. Di Palma, A. Clemente, L. Dussopt, R. Sauleau, P. Potier, and P. Pouliguen, "Circularly polarized transmitarray with sequential rotation in Ka-band," *IEEE Transactions on Antennas and propagation*, vol. 63, no. 11, pp. 5118–5124, 2015.

[171] F. Qin, L. Wan, L. Li, H. Zhang, G. Wei, and S. Gao, "A transmission metasurface for generating OAM beams," *IEEE Antennas and Wireless Propagation Letters*, vol. 17, no. 10, pp. 1793–1796, 2018.

139

[172] Y. Wang, K. Zhang, Y. Yuan, X. Ding, B. Ratni, S. N. Burokur, and Q. Wu, "Planar vortex beam generator for circularly polarized incidence based on FSS," *IEEE Transactions on Antennas and Propagation*, vol. 68, no. 3, pp. 1514–1522, 2019.

[173] S. Jiang, C. Chen, H. Zhang, and W. Chen, "Achromatic electromagnetic metasurface for generating a vortex wave with orbital angular momentum (OAM)," *Optics express*, vol. 26, no. 5, pp. 6466–6477, 2018.

[174] H.-H. Lv, Q.-L. Huang, X.-J. Yi, J.-Q. Hou, and X.-W. Shi, "Low-profile transmitting metasurface using single dielectric substrate for OAM generation," *IEEE Antennas and Wireless Propagation Letters*, vol. 19, no. 5, pp. 881–885, 2020.

[175] D. Thompson, P. Kirby, J. Papapolymerou, and M. M. Tentzeris, "W-band characterization of finite ground coplanar transmission lines on liquid crystal polymer (LCP) substrates," in *Electronic Components and Technology Conference*. IEEE; 1999, 2003, pp. 1652–1655.

[176] C. A. Fernandes, E. B. Lima, and J. R. Costa, *Dielectric Lens Antennas*. Singapore: Springer Singapore, 2016, pp. 1001–1064.

[177] S. Lee, *Differential geometry for GTD applications*. University of Illinois at Urbana-Champaign, 1976.

[178] A. Sharma, D. V. Kumar, and A. K. Ghatak, "Tracing rays through graded-index media: a new method," *Applied Optics*, vol. 21, no. 6, pp. 984–987, 1982.

[179] R. M. More and K. Kosaka, "Wave-front curvature in geometrical optics," *Phys. Rev. E*, vol. 57, pp. 6127–6134, May 1998. [Online]. Available: https://link.aps.org/doi/10.1103/PhysRevE.57.6127

[180] H. Bremmer and S. Lee, "Propagation of a geometrical optics field in an isotropic inhomogeneous medium," *Radio science*, vol. 19, no. 01, pp. 243–257, 1984.

[181] I. Amidror, "Scattered data interpolation methods for electronic imaging systems: a survey," *Journal of electronic imaging*, vol. 11, no. ARTICLE, pp. 157–76, 2002.

[182] H. Yang, F. Yang, X. Cao, S. Xu, J. Gao, X. Chen, M. Li, and T. Li, "A 1600-element dual-frequency electronically reconfigurable reflectarray at X/Ku-band," *IEEE Transactions on Antennas and propagation*, vol. 65, no. 6, pp. 3024–3032, 2017.